Cell

Intercellular nanotube-mediated mitochondrial transfer enhances T cell metabolic fitness and antitumor efficacy

Graphical abstract

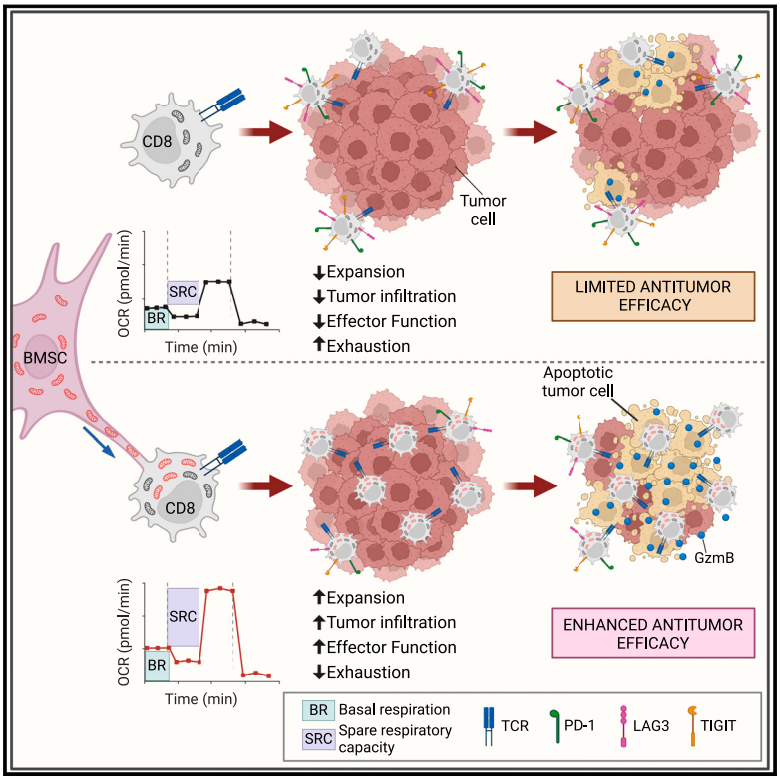

Highlights

- BMSCs transfer mitochondria to CD8$^+$ T cells via intercellular nanotube connections
- Mitochondrial transfer between BMSCs and CD8$^+$ T cells depends on Talin 2
- Mitochondrial transfer augments CD8$^+$ T cell mitochondria mass and metabolic fitness
- Mitochondria-boosted mouse and human CD8$^+$ T cells exhibit superior antitumor efficacy

Authors

Jeremy G. Baldwin, Christoph Heuser-Loy, Tanmoy Saha, ..., Jessica Fioravanti, Shiladitya Sengupta, Luca Gattinoni

Correspondence

jeremy.baldwin@ukr.de (J.G.B.), shiladit@mit.edu (S.S.), luca.gattinoni@lit.eu (L.G.)

In brief

Transfer of mitochondria via nanotubes from bone marrow stem cells to CD8$^+$ T cells augments cellular metabolism, empowering engineered T cells and tumor-infiltrating lymphocytes to counteract exhaustion and fight tumors more effectively.

Baldwin et al., 2024, Cell *187*, 6614–6630
November 14, 2024
https://doi.org/10.1016/j.cell.2024.08.029

CellPress

CellPress
OPEN ACCESS

Cell

Article

Intercellular nanotube-mediated mitochondrial transfer enhances T cell metabolic fitness and antitumor efficacy

Jeremy G. Baldwin,[1,2,*] Christoph Heuser-Loy,[1,22] Tanmoy Saha,[3,4,22] Roland C. Schelker,[1,5] Dragana Slavkovic-Lukic,[1] Nicholas Strieder,[6] Inmaculada Hernandez-Lopez,[6] Nisha Rana,[1,7] Markus Barden,[8] Fabio Mastrogiovanni,[1] Azucena Martín-Santos,[1] Andrea Raimondi,[9] Philip Brohawn,[10] Brandon W. Higgs,[11] Claudia Gebhard,[6] Veena Kapoor,[2] William G. Telford,[2] Sanjivan Gautam,[2] Maria Xydia,[12,13] Philipp Beckhove,[5,7,13] Sina Frischholz,[14] Kilian Schober,[14,15] Zacharias Kontarakis,[16,17] Jacob E. Corn,[18] Matteo Iannacone,[19,20] Donato Inverso,[19,20] Michael Rehli,[5,6] Jessica Fioravanti,[1,2] Shiladitya Sengupta,[3,4,*] and Luca Gattinoni[1,2,7,21,23,*]

[1]Division of Functional Immune Cell Modulation, Leibniz Institute for Immunotherapy, Regensburg, Germany
[2]Center for Cancer Research, National Cancer Institute, National Institutes of Health, Bethesda, MD, USA
[3]Center for Engineered Therapeutics, Department of Medicine, Brigham and Women's Hospital, Harvard Medical School, Boston, MA, USA
[4]Harvard-MIT Division of Health Sciences and Technology, Cambridge, MA, USA
[5]Department of Internal Medicine III, University Hospital Regensburg, Regensburg, Germany
[6]Next Generation Sequencing Core, Leibniz Institute for Immunotherapy, Regensburg, Germany
[7]University of Regensburg, Regensburg, Germany
[8]Division of Genetic Immunotherapy, Leibniz Institute for Immunotherapy, Regensburg, Germany
[9]Experimental Imaging Centre, IRCCS San Raffaele Scientific Institute, Milan, Italy
[10]Translational Science and Experimental Medicine, Early R&I, AstraZeneca, Gaithersburg, MD, USA
[11]Genmab, Princeton, NJ, USA
[12]Bavarian Cancer Research Center (BZKF), Regensburg, Germany
[13]Division of Interventional Immunology, Leibniz Institute for Immunotherapy, Regensburg, Germany
[14]Mikrobiologisches Institut, Klinische Mikrobiologie, Immunologie und Hygiene, Universitätsklinikum Erlangen und Friedrich-Alexander-Universität (FAU) Erlangen-Nürnberg, Erlangen, Germany
[15]FAU Profile Center Immunomedicine, FAU Erlangen-Nürnberg, Erlangen, Germany
[16]Genome Engineering and Measurement Laboratory (GEML), ETH Zürich, Zürich, Switzerland
[17]Functional Genomics Center Zürich, ETH Zürich, University of Zürich, Zürich 8057, Switzerland
[18]Department of Biology, Institute of Molecular Health Sciences, ETH Zürich, Zürich, Switzerland
[19]Division of Immunology, Transplantation and Infectious Diseases, IRCCS San Raffaele Scientific Institute, Milan, Italy
[20]Vita-Salute San Raffaele University, Milan, Italy
[21]Center for Immunomedicine in Transplantation and Oncology, University Hospital Regensburg, Regensburg, Germany
[22]These authors contributed equally
[23]Lead contact
*Correspondence: jeremy.baldwin@ukr.de (J.G.B.), shiladit@mit.edu (S.S.), luca.gattinoni@lit.eu (L.G.)
https://doi.org/10.1016/j.cell.2024.08.029

SUMMARY

Mitochondrial loss and dysfunction drive T cell exhaustion, representing major barriers to successful T cell-based immunotherapies. Here, we describe an innovative platform to supply exogenous mitochondria to T cells, overcoming these limitations. We found that bone marrow stromal cells establish nanotubular connections with T cells and leverage these intercellular highways to transplant stromal cell mitochondria into $CD8^+$ T cells. Optimal mitochondrial transfer required Talin 2 on both donor and recipient cells. $CD8^+$ T cells with donated mitochondria displayed enhanced mitochondrial respiration and spare respiratory capacity. When transferred into tumor-bearing hosts, these supercharged T cells expanded more robustly, infiltrated the tumor more efficiently, and exhibited fewer signs of exhaustion compared with T cells that did not take up mitochondria. As a result, mitochondria-boosted $CD8^+$ T cells mediated superior antitumor responses, prolonging animal survival. These findings establish intercellular mitochondrial transfer as a prototype of organelle medicine, opening avenues to next-generation cell therapies.

INTRODUCTION

Adoptive T cell therapies have proven powerful against hematologic malignancies, but efficacy against solid tumor entities is limited.[1,2] A major hurdle faced by transferred T cells is the hostile tumor microenvironment, which disrupts normal mitochondrial activity, driving T cell exhaustion.[3–7] Ultimately, impaired mitochondrial fitness orchestrates transcriptional and epigenetic

programs associated with terminal exhaustion, leading to defective antitumor T cell responses and cancer immune evasion.[3,4] Thus, strategies to boost mitochondrial function in infused T cells are highly sought after. Previous preclinical attempts include leveraging intrinsic T cell properties, such as the generation or selection of T cell subsets with higher mitochondrial fitness,[8,9] and active intervention strategies, such as genetic engineering of drivers of mitochondrial biogenesis,[6,10] or the administration of antioxidants during T cell manufacturing to protect mitochondrial integrity.[11] However, these approaches in general narrowly focus on single targets and are largely ineffective if T cells contain mitochondria that are already dysfunctional or have damaged mitochondrial DNA (mtDNA).

In recent years, intercellular transfer of mitochondria has been described, reflecting the evolutionary history of mitochondria as endosymbionts. Mitochondrial transfer has been shown to not only aid the repair of damaged cells[12,13] but also to be exploited by tumor cells, which hijack mitochondria from tumor-infiltrating lymphocytes (TILs)[14] and stromal cells to support their growth.[15,16] Several mechanisms of mitochondrial transfer have been described, including trafficking through gap junctions and extrusion of microvesicle-embedded or free-floating mitochondria.[17] However, one of the most predominant routes of mitochondrial transfer is tunneling nanotubes (TNTs). TNTs are F-actin-supported membrane protrusions that can traverse vast distances to bridge cells, enabling the exchange of cytoplasmic factors and organelles between connected cells.[13,18]

We sought to leverage mitochondrial transfer from bone marrow stromal cells (BMSCs) to boost CD8$^+$ T cell bioenergetic capacity, resistance to exhaustion, and antitumor efficacy. We found that TNTs enable effective mitochondrial transfer from BMSCs to T cells, providing the basis of a technology platform to potentiate the metabolic fitness and antitumor function of T cells for adoptive immunotherapy.

RESULTS

Intercellular nanotubes enable mitochondrial trafficking from BMSCs to CD8$^+$ T cells

BMSCs have been shown to be potent modulators of T cell function and differentiation.[19] To investigate the interaction between BMSCs and CD8$^+$ T cells, we set up a co-culture study with either human or mouse BMSCs and species-matched CD8$^+$ T cells on glass coverslips. Cells were fixed after 24 h and examined using field-emission scanning electron microscopy (FESEM). We frequently found complex nanotube structures physically bridging BMSCs and CD8$^+$ T cells in both human (Figures 1A and 1B) and mouse (Figures 1C and 1D) settings. The detection of complex branching nanotubes indicates that these intercellular bridging structures were not mere stress fibers (Figures 1B and 1B1). The average number of nanotubes per cell for both BMSCs and CD8$^+$ T cells was one per cell (Figure 1E). However, as nanotubes are ultrafine structures that may be lost during sample processing, we consider that the actual number per cell may be higher. Overall, mouse nanotubes were shorter ($\leq$20 μm) and narrower ($\leq$1 μm) compared with their human counterparts whose dimensions were more variable with maximal lengths and widths exceeding 40 and 2 μm, respectively (Figures 1F and 1G). Interestingly, despite the narrow average width, some nanotubes exhibited enlarged segments, which may accommodate trafficking organelles, such as mitochondria (Figures 1C1 and 1D, far right inlet).

To determine if mitochondria are indeed transported within nanotubes from BMSCs to CD8$^+$ T cells, we transduced BMSCs with a dsRed-tagged mitochondrial subunit protein (*COX8A*), known as Mito-dsRed, and evaluated BMSC-CD8$^+$ T cell co-cultures using confocal microscopy. After 24 h co-incubation, we observed that a fraction of CD8$^+$ T cells acquired dsRed signal in both human (Figure 1H) and mouse (Figure 1I) settings. We used Phalloidin Green to stain F-actin of both BMSCs and CD8$^+$ T cells to delineate nanotube structures. We observed enlarged portions of the nanotubes (Figure 1H), confirming our FESEM observations. Notably, we also detected dsRed signals co-localized within these regions (Figure 1H), substantiating our speculation that TNTs serve mitochondrial trafficking from BMSCs to CD8$^+$ T cells. Mitochondria are unique among organelles within the cell as they contain a small independent genome, mtDNA.[20] Interestingly, high magnification of TNT bulges and locally adapted exposure of blue-fluorescent DNA stain, DAPI, showed traces of DNA that co-localized with dsRed pockets, consistent with the presence of intact mitochondria (Figure 1H, inlet). Taken together, FESEM and confocal studies revealed nanotube-mediated intercellular trafficking of mitochondria from BMSCs to CD8$^+$ T cells in both mouse and human cells.

Establishment and validation of mitochondrial transfer as technology platform

Compared with conventional 2D tissue culture plastic, we found that a co-culture transwell system (Figure 2A) improved cell viability and transfer rates of dsRed mitochondria from BMSCs to CD8$^+$ T cells, especially when mouse cells were used (Figure S1A). Mitochondrial transfer required CD8$^+$ T cell activation and peaked at 48 h (Figures S1B–S1E). Notably, we could not observe any meaningful uptake of mitochondria following co-incubation of free-floating mitochondria isolated from BMSCs with T cells (Figure S1F). Hereafter, CD8$^+$ T cells that acquire donor mitochondria in co-culture will be referred to as Mito$^+$, whereas CD8$^+$ T cells that do not will be referred to as Mito$^-$ cells. The average percentage of Mito$^+$ (dsRed$^+$CD8$^+$) cells after a 36–48 h co-culture ranged from 6.2% to 24.7% with a median of 12.5% (Figure 2B). Mito$^+$ and Mito$^-$ cells could be sorted to purities higher than 90% (Figure 2C). To validate the transfer of mitochondria, we initially performed confocal microscopy of sorted Mito$^+$ cells. We stained sorted Mito$^+$ cells with a fluorescently conjugated CD8-specific antibody to delineate the cell membrane and MitoTracker Deep Red to determine if mitochondria had active membrane potential. We found that dsRed mitochondria were internalized within recipient CD8$^+$ T cells and maintained intact mitochondrial membrane potential (Figure 2D). To more precisely attribute dsRed signals to mitochondria, we used correlative light-electron microscopy (CLEM), which employs a combination of fluorescence microscopy with an electron microscope, to image Mito$^+$ cells. We found that dsRed signals co-localized with mitochondria structures and were not diffuse in the cell cytosol (Figure 2E). These studies allowed us

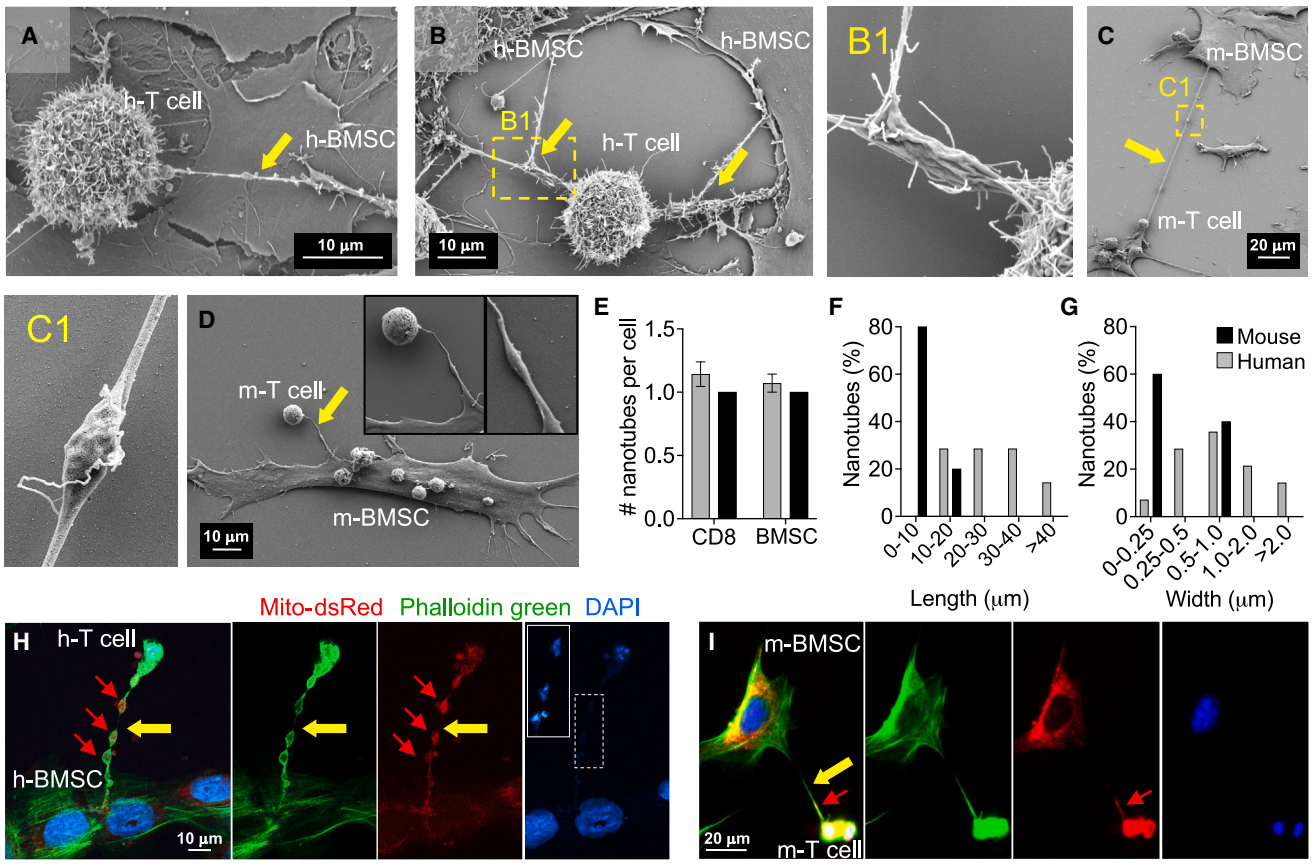

Figure 1. Intercellular nanotubes enable mitochondrial trafficking from BMSCs to CD8⁺ T cells

(A–D) FESEM images showing nanotubes (yellow arrows) between BMSCs and CD8⁺ T cells in human (A and B) and mouse (C and D) co-cultures. The images show thin (A), thick (B), and branched (B1) nanotubes.

(E–G) Bar graphs showing the number of nanotubes between BMSCs and CD8⁺ T cells (E) and the distribution of lengths (F) and widths (G) of nanotubes connecting the BMSC and CD8⁺ T cells, as calculated from the FESEM images. Data shown in (E) are mean ± SEM (n = 5–14).

(H and I) Confocal microscopy images of nanotube (yellow arrows) formation between Mito-dsRed BMSCs and CD8⁺ T cells in human (H) and mouse (I) co-cultures. Transfer of mitochondria has been observed inside the nanotube (red arrows). Co-cultures were fixed after 24 h and stained with Phalloidin Green and DAPI. Co-localization of DAPI and dsRed signals within the nanotube (H) indicates the trafficking of intact mitochondria from the BMSCs to CD8⁺ T cells. Scale bar is 10 μm (A, B, D, and H) and 20 μm (C and I).

also to examine the morphological structure of transferred donor mitochondria in more detail. Qualitative analysis showed organized cristae and double membrane arrangements typical of a normal mitochondria phenotype (Figures 2E1 and 2E2).

To assess if the transferred donor mitochondria increased the overall mitochondrial mass of the recipient CD8⁺ T cells, we used quantitative real-time PCR to determine mtDNA content of Mito⁺ and Mito⁻ cells as measured by *mt-Co2* gene normalized to the nuclear gene standard reference gene *App*. Mito⁺ cells showed a fold-change increase in mtDNA content ranging from 1.1 to 2.5 (median = 1.34) compared with Mito⁻ cells (Figure 2F). To validate if the mitochondrial transfer from BMSCs contributes to this increase in mitochondrial content, we co-cultured our Mito-dsRed BMSC line, which was derived from a C57BL/6 mouse strain, with CD8⁺ T cells isolated from BALB/c mice. BALB/c mtDNA has a single nucleotide polymorphism at A9348 in the *mt-Co3* gene that disrupts an *Asp*I restriction site that is normally present in C57BL/6 mtDNA, allowing the genetic discrimination of endogenous and transferred mitochondria. We then extracted mtDNA from highly enriched Mito⁺ and Mito⁻ cells (>98% purity) and performed restriction enzyme analysis of the *mt-Co3* target region, as previously described.[21] Mito⁻ cells showed a uniform 385 bp band, congruent with non-co-cultured BALB/c CD8⁺ control T cells. Strikingly, Mito⁺ cells showed a mixture of BALB/c and C57BL/6 mtDNAs, demonstrating the presence of both endogenous and donor mtDNA (Figure 2G).

BMSC mitochondrial transfer enhances CD8⁺ T cell metabolic fitness

A key task of mitochondria is energy production, primarily via aerobic respiration. To evaluate the effect of donor mitochondria on CD8⁺ T cell respiration, we measured oxygen consumption rates at a steady state and after perturbation with diverse modulators of mitochondrial respiration (Figure 2H). Overall, Mito⁺ cells showed significantly higher basal respiration and spare respiratory

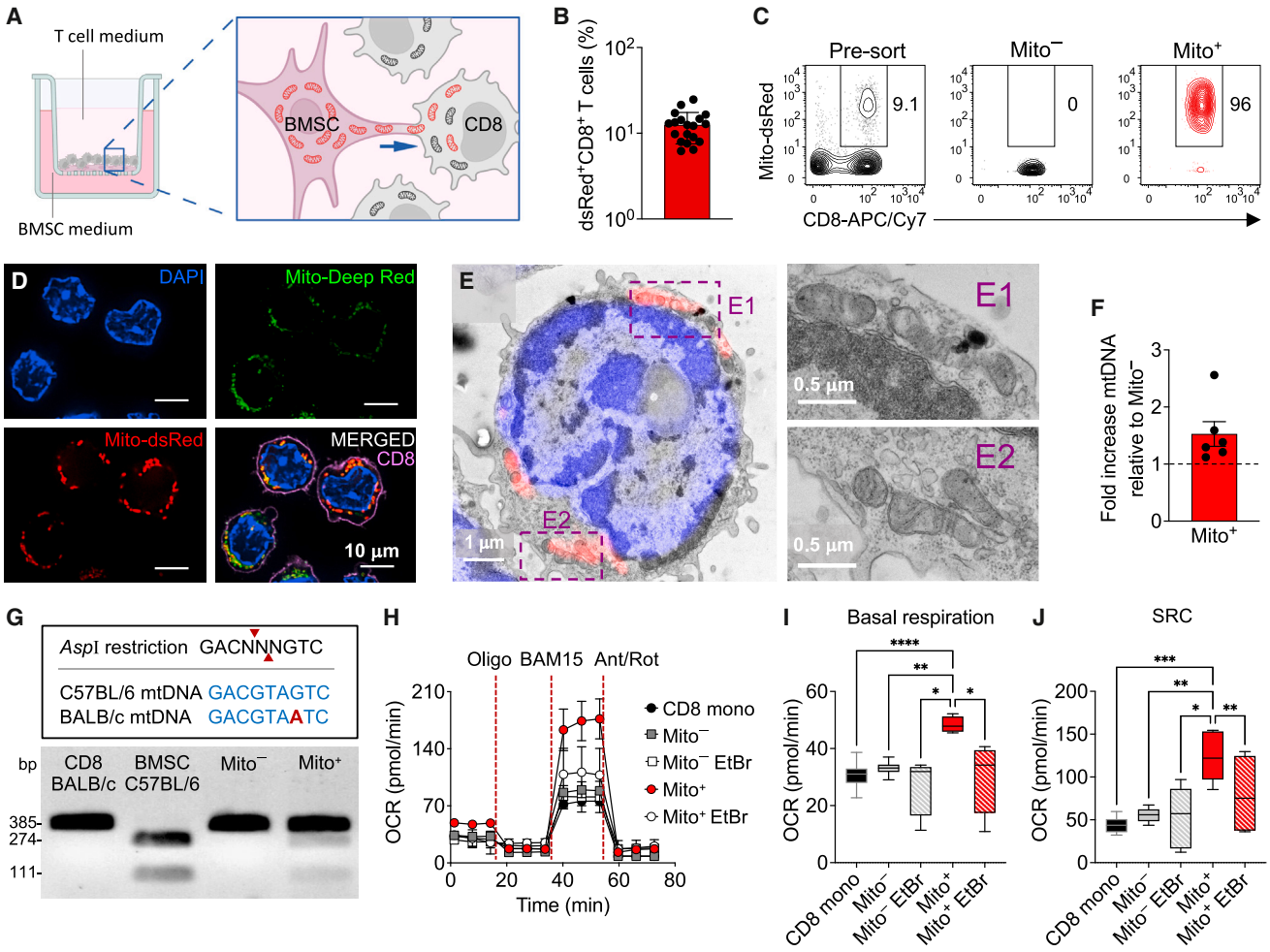

Figure 2. Mitochondrial transfer enhances CD8⁺ T cell metabolic fitness

(A) Cartoon depicting the transwell co-culture system designed to promote mitochondrial transfer from Mito-dsRed BMSCs to CD8⁺ T cells.

(B) Percentage of mouse CD8⁺dsRed⁺T cells 48 h after co-culture with Mito-dsRed BMSCs. Data shown are mean ± SEM, *n* = 19 independent co-culture experiments.

(C) Flow cytometry plots of mouse CD8⁺ T cells 48 h after co-culture with Mito-dsRed BMSCs before (left) and after (right) sorting based on dsRed signal. Numbers indicate percentage after gating on live lymphocytes.

(D) Representative confocal microscopy image showing FACS-sorted mouse CD8⁺ T cells that have received donor-labeled mitochondria from Mito-dsRed BMSCs. MitoTracker Deep Red was used to label total mitochondria after sorting. Scale bar is 10 µm.

(E) Correlative confocal and transmission electron microscopy image of FACS-sorted mouse CD8⁺ T cells that have received donor-labeled mitochondria from Mito-dsRed BMSCs. Overlay of nucleus (DAPI) and acquired mitochondria (dsRed) with the electron micrograph of the same section. Scale bar is 1 µm.

(E1 and E2) Electron micrograph alone of transferred mitochondria. Scale bar is 0.5 µm.

(F) Percent increase in mtDNA (as measured by *mt-Co2* gene normalized to nuclear *App* gene) of mouse Mito⁺ cells relative to Mito⁻ (*n* = 7 biological replicates, data shown are mean ± SEM).

(G) Restriction enzyme analysis of Mito⁺ and Mito⁻ BALB/c CD8⁺ T cells after co-culture with C57BL/6-derived Mito-dsRed BMSCs. C57BL/6 cells have a single nucleotide polymorphism at A9348 in the *mt-Co3* gene that creates an *Asp*I restriction site.

(H) Oxygen consumption rates (OCRs) of FACS-sorted Mito⁺ and Mito⁻ mouse CD8⁺ T cells after co-culture with Mito-dsRed BMSCs that were left untreated or pre-treated with 200 ng/mL ethidium bromide (EtBr) in DMEM complete medium supplemented with 50 µg/mL uridine to render donor mitochondria dysfunctional. CD8⁺ T cells monocultured (CD8 mono) were included as additional control. Data were obtained under basal culture conditions and in response to the indicated molecules.

(I and J) (I) Basal respiration and (J) spare respiratory capacity (SRC) (*n* = 6–12, 2–4 technical replicates per 3 time points, data shown are mean ± SEM). *$p < 0.05$; **$p < 0.01$; ***$p < 0.001$; ***$p < 0.0001$ (one-way ANOVA with Dunnett's multiple-comparison test).

See also Figures S1 and S2.

capacity (SRC) compared with either Mito⁻ cells or CD8⁺ T cells that were not co-cultured with BMSCs (CD8 mono) (Figures 2I and 2J). To exclude the possibility that the enhanced mitochondrial activity of Mito⁺ cells was due to the intercellular transfer of other cytoplasmic factors, we set up additional control groups using Mito-dsRed-labeled BMSCs whose mitochondria were

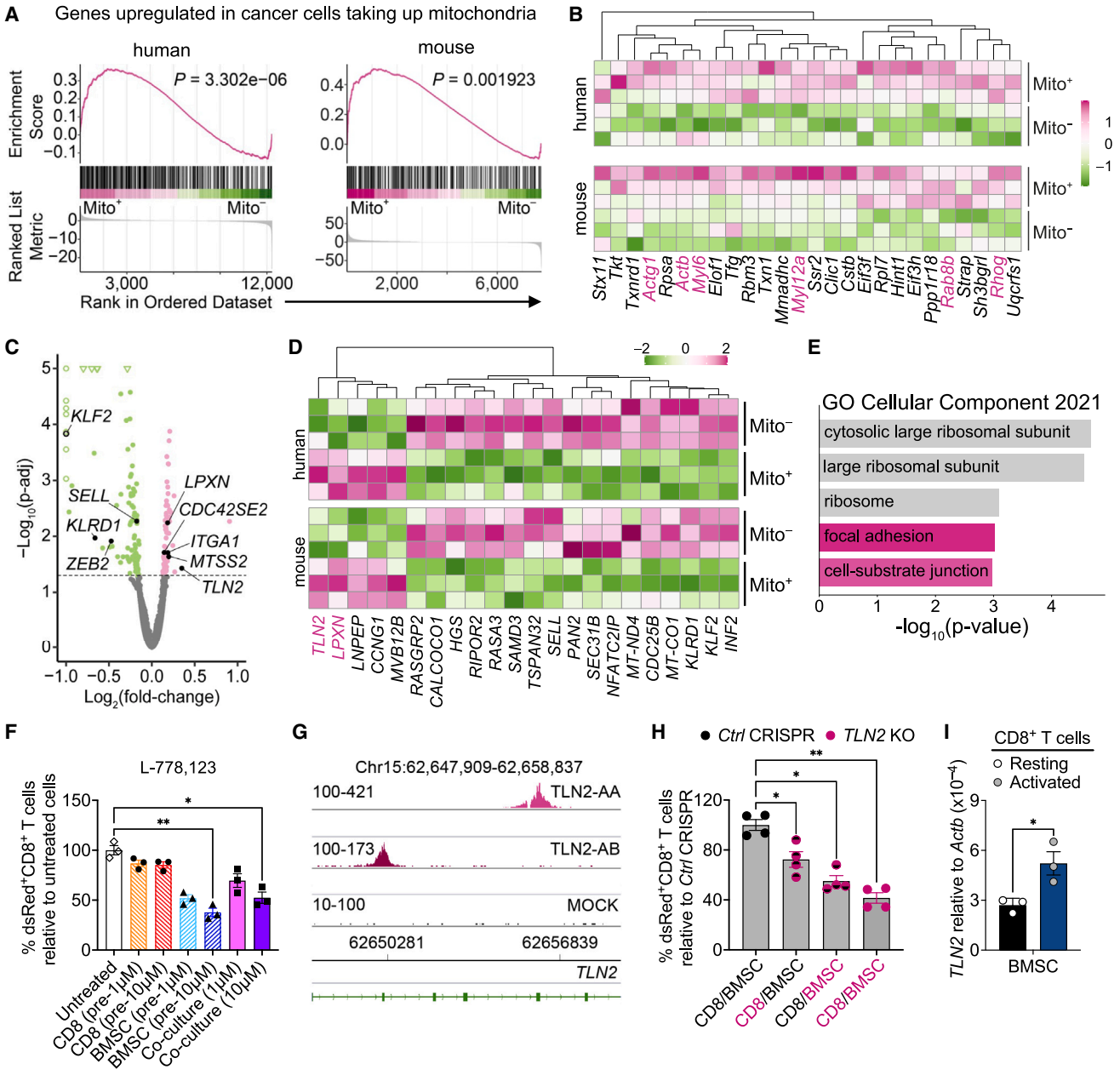

Figure 3. Mitochondrial transfer from BMSCs to T cells is TLN2-dependent

(A) GSEA of human and mouse Mito$^+$ cells showing positive enrichment of genes upregulated in cancer cells acquiring mitochondria from neighboring cells.[25]

(B) Heatmap showing 26 of the enriched genes in the GSEA that are co-regulated in both human and mouse Mito$^+$ cells.

(C) Volcano plot showing changes in gene expression between Mito$^+$ and Mito$^-$ human CD8$^+$ T cells. Gene expression was evaluated by RNA-seq on Mito$^+$ and Mito$^-$ cells FACS-sorted after 48 h co-culture with human Mito-dsRed BMSCs (n = 3 healthy donors) (dashed line, p adj = 0.05).

(D) Heatmap of the top 22 selected DEG in Mito$^+$ and Mito$^-$ human CD8$^+$ T cells (false discovery rate [FDR] corrected, $p$adj.hs < 0.05) that are more robustly co-regulated in mouse CD8$^+$ T cells (p.ms < 0.15).

(E) Overrepresentation analysis of the 59 orthologous genes co-regulated in human and mouse Mito$^+$ and Mito$^-$ CD8$^+$ T cells using GO ontology terms (baseMean.hs > 100, $p$adj.hs < 0.05). Bar graph illustrates the top 5 Gene Ontology terms of genes enriched.

(F) Percentage of dsRed$^+$CD8$^+$ T cells after BMSCs-CD8$^+$ T cells co-cultures. Indicated doses of the farnesyltransferase and geranylgeranyltransferase inhibitor L-778,123 were added to BMSCs and CD8 T cells before or during co-cultures. Data are shown as mean ± SEM relative to untreated co-cocultures.

(G) Double-strand break repair, as indicated by MRE11 chromatin immunoprecipitation sequencing (ChIP-seq) signal at the TLN2 locus in CRISPR-Cas (TLN2-AA or TLN2-AB) and mock-treated T cells. y axis scale depicting the NGS read coverage at the left of each sample. Genomic coordinates on the x axis.

(legend continued on next page)

selectively rendered partially dysfunctional by pre-treatment with low-dose ethidium bromide (EtBr). EtBr-treated BMSCs had lower mitochondrial membrane potential, decreased mtDNA, and exhibited severely impaired mitochondrial respiration (Figures S2A–S2C). Even though EtBr treatment resulted in a reduction of the Rho-GTPase RHOT1 (also known as Miro1) (Figure S2D), a key promoter of intercellular mitochondrial trafficking,[22] BMSCs maintained their capacity to transfer dysfunctional mitochondria to recipient CD8$^+$ T cells (Mito$^+$ EtBr) (Figures S2E–S2G). Notably, the improvement in mitochondrial fitness observed in Mito$^+$ cells was abrogated in Mito$^+$ EtBr cells (Figures 2H–2J). Altogether, these results not only functionally validate the effective transfer of mitochondria to CD8$^+$ T cells but also demonstrate that the increased metabolic activity in Mito$^+$ cells is donor mitochondria-dependent.

Mitochondrial transfer between BMSCs and T cells depends on TLN2

TNTs are unique cell protrusions and undergo several phases of development, including (1) initiation of membrane curvature via inverse BAR (I-BAR) proteins, (2) extension of the membrane protrusion via actin polymerization and integrin binding mediated by focal adhesion proteins (FAPs), and (3) reaching the adjacent cell and undergoing membrane fusion to complete the intercellular, cytosol-bridging connection.[23] Rho-GTPases have been shown to play a key role throughout this process from activating I-BAR proteins to regulating focal adhesion and assisting in trafficking mitochondria through nanotubes (a well-known example being RHOT1).[22,24]

To further unravel the mechanisms governing mitochondrial transfer, we performed bulk and single-cell RNA sequencing (scRNA-seq) on sorted human and mouse Mito$^+$ and Mito$^-$ cells. Recently, Zhang et al.[25] reported a gene signature associated with cancer cells that take up mitochondria from neighboring cells. Gene set enrichment analysis (GSEA) revealed a significant enrichment of this core signature in both human and mouse Mito$^+$ T cells (Figure 3A; Table S1), suggesting shared biological features across different cell types that acquire mitochondria. Notably, human and mouse Mito$^+$ cells exhibited an enrichment of genes involved in organelle trafficking and TNT formations including cytoskeleton proteins (*ACTB* and *ACTG1*), myosin-II complex proteins (*MYL6* and *MYL12A*), and small GTPases (*RHOG* and *RAB8B*)[26,27] (Figure 3B).

Among the genes differentially expressed in human Mito$^+$ and Mito$^-$ cells, we found several molecules involved in membrane curvature initiation, protrusion, and elongation. For instance, MTSS I-BAR domain containing 2 (MTSS2, also known as ABBA-1), which regulates plasma membrane dynamics and Rho GTPase activity[28,29]; Talin 2 (TLN2), a cytoskeletal protein involved in actin filaments assembly, which mediates their interaction with integrins and membrane protrusions[30,31]; leupaxin (LPXN), a focal adhesion-associated protein[32]; integrin alpha-1 (ITGA1), which is involved in CD8$^+$ T cell motility[33]; and CDC42 small effector 2 (CDC42SE),[34] a downstream regulator of small Rho-GTPase CDC42 involved in actin assembly and cell shape,[35] were all upregulated in human Mito$^+$ cells (Figure 3C). The genes differentially expressed in mouse Mito$^+$ and Mito$^-$ cells were largely different from those identified in human cells (Tables S2 and S3). Notwithstanding, we did identify 59 transcripts that were co-regulated in both conditions (Table S4). The top 22 co-regulated genes are shown in Figure 3D. Of note, *TLN2* and *LPXN* were among the few genes upregulated in Mito$^+$ cells in both mouse and human settings. Consistent with this observation, Gene Ontology (GO) analysis showed that focal adhesion and cellular substrate junction genes were among the gene sets most significantly enriched in co-regulated genes (Figure 3E; Table S5).

The heightened expression of genes involved in the formation of membrane protrusions and extensions suggests that CD8$^+$ T cells taking up BMSC mitochondria display an increased ability to establish TNT connections. Using L-788,123, an inhibitor of farnesyltransferase and geranylgeranyltransferase type 1 that has been previously shown to partially block nanotube-mediated mitochondria transfer,[14] we confirmed that TNTs are a primary mediator of mitochondrial transfer (Figure 3F). Interestingly, pre-treatment of CD8$^+$ T cells with L-788,123 had minimal impact on mitochondrial transfer compared with BMSC pre-treatment. To test whether BMSCs or CD8$^+$ T cells initiate TNTs, we then focused on *TLN2* given that it was the second highest upregulated gene in human Mito$^+$ cells and was similarly regulated in mouse cells that acquired donor mitochondria. Considering that talins have been shown to promote integrin activation and membrane dynamics/outgrowth,[30] we reasoned that TLN2 may also play a role in the extension of nanotubes and subsequent mitochondrial transfer. To test this hypothesis, we used CRISPR-Cas9 gene editing technology to knockout *TLN2* in CD8$^+$ T cells as well as in Mito-dsRed BMSCs before co-culture. We selected CRISPR RNAs (crRNAs) that exhibited high efficacy and negligible off-target activity using the DISCOVER-seq (discovery of *in situ* Cas off-targets and verification by sequencing) platform[36] (Figures 3G and S3). Deletion of *TLN2* in both CD8$^+$ T cells or BMSCs was sufficient to significantly impair mitochondrial transfer rates, with the effects being more pronounced in BMSCs (Figure 3H). These findings together with results from the L778,123 treatment studies suggest that the process of mitochondrial transfer is initiated by BMSCs. Given that activation of CD8$^+$ T cells is required for active mitochondrial transfer (Figures S1B and S1C), we sought to determine if activated CD8$^+$ T cells prime BMSCs for transfer. Interestingly, we found that *TLN2* expression in BMSCs was upregulated upon co-culture with activated CD8$^+$ T cells compared with non-activated/resting control CD8$^+$ T cells as assessed by qPCR (Figure 3I). These datasets implicate TLN2 as a key regulator of nanotube-mediated mitochondrial transfer on both donor and recipient cells but with a more critical role in BMSCs.

(H) Percentage of dsRed$^+$CD8$^+$ T cells after BMSCs-CD8$^+$ T cell co-cultures in which TLN2 was deleted in the indicated cell type (magenta color). Data are shown as mean ± SEM relative to control co-cultures in which CD2 was deleted (n = 3 healthy donors).
(I) qPCR of *TLN2* mRNA of human Mito-dsRed BMSCs sorted following co-culture with either resting or activated human CD8$^+$ T cells. Bars (mean ± SEM of 3 healthy donors) relative to *Actb*. *p < 0.05 (one-way ANOVA, F and H; unpaired two-tailed Student's t test, I); **p < 0.01 (one-way ANOVA, F and H).
See also Figure S3.

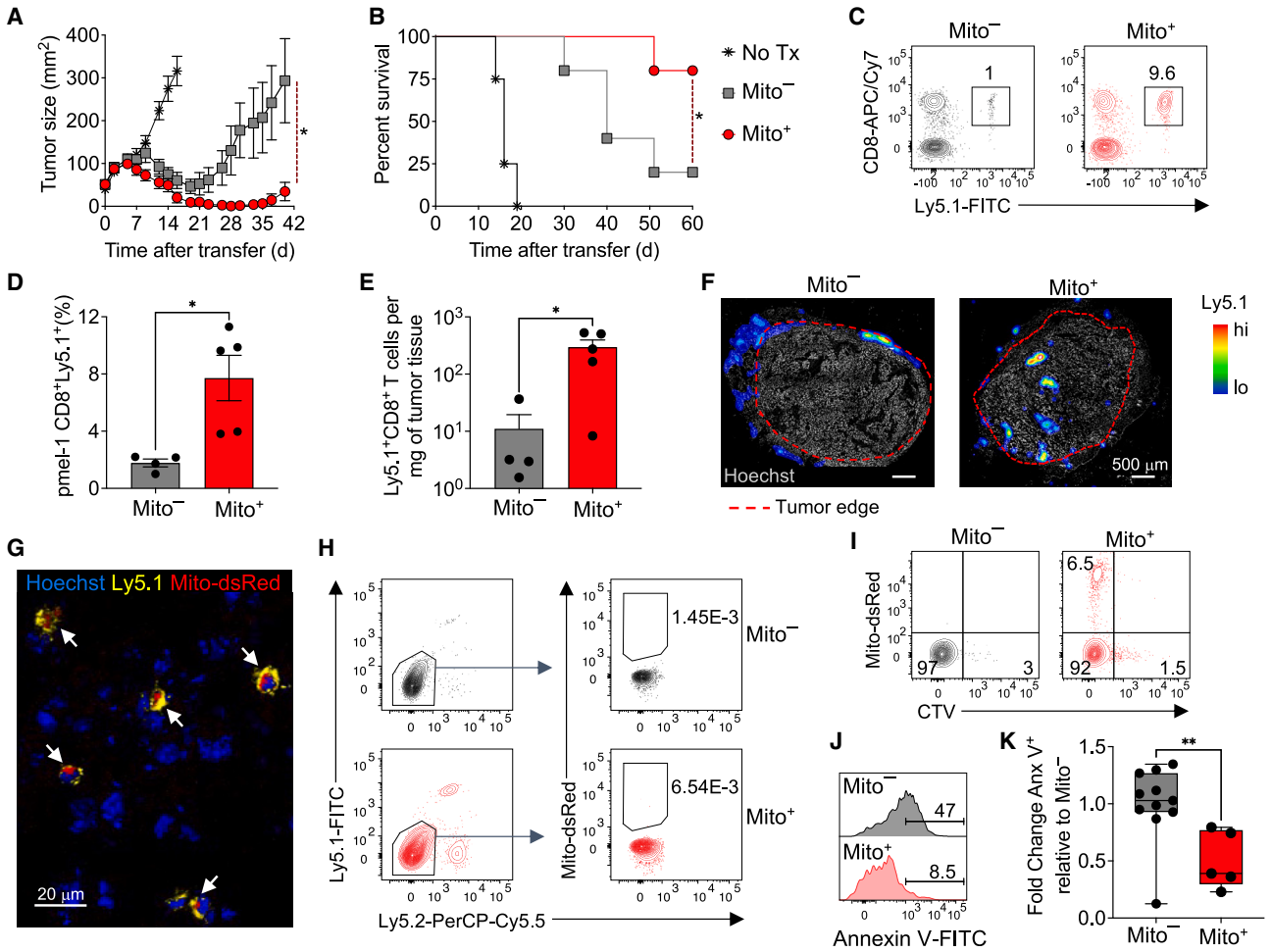

Figure 4. Mitochondrial transfer enhances CD8⁺ T cell antitumor immunity against solid tumors

(A and B) Tumor size (A, mean ± SEM) and survival curve (B) of sublethally irradiated $B16_{KVP}$ tumor-bearing Ly5.2⁺ mice receiving 1.5 × 10^5 Mito⁺ or Mito⁻ pmel-1 Ly5.1⁺CD8⁺ T cells generated as in Figure 2A in conjunction with recombinant human interleukin-2 (IL-2) (n = 5 mice/group). No Tx, no treatment (n = 4 mice).

(C and D) Flow cytometry plot (C) and frequency (D) of Mito⁺ and Mito⁻ pmel-1 Ly5.1⁺CD8⁺ T cells in the spleen 7 days after transfer. Data shown in (D) are mean ± SEM (n = 4–5 biological replicates).

(E) Numbers of pmel-1 Ly5.1⁺CD8⁺ T cells per mg of tumor tissue, 7 days after treatment as in (A) and (B). Data shown as mean ± SEM (n = 4–5 biological replicates).

(F and G) Confocal microscopy images of tumor sections stained with Ly5.1 and Hoechst 7 days after treatment with Mito⁺ pmel-1 Ly5.1⁺CD8⁺ T cells as in (A) and (B). Arrows indicate tumor-infiltrating pmel-1 Ly5.1⁺ T cells retaining internalized Mito-dsRed signals. Scale bar is 500 μm (F) and 20 μm (G).

(H) Flow cytometry plot of Mito-dsRed⁺ cells in non-immune components (Ly5.1⁻Ly5.2⁻) of the tumor microenvironment.

(I) Flow cytometry plot of Mito⁺ pmel-1 Ly5.1⁺CD8⁺ T cells in the tumor 7 days after transfer showing CTV signals versus Mito-dsRed.

(J and K) Flow cytometry plot (J) and fold change of annexin V frequency (K) in Mito⁺ and Mito⁻ pmel-1 Ly5.1⁺CD8⁺ T cells in the tumor 7 days after transfer. Data shown as mean ± SEM relative to Mito⁻ cells (n = 5–10, from two pooled independent experiments). *p < 0.05 (unpaired two-tailed Student's t test, A, D, and E; log-rank [Mantel-Cox] test, B) **p < 0.01 (unpaired two-tailed Student's t test, K).

See also Figures S4 and S5.

Mitochondrial transfer enhances CD8⁺ T cell antitumor immunity against solid tumors

Our bioenergetic studies indicate that mitochondrial transfer enhances mitochondrial respiration and SRC of CD8⁺ T cells. SRC is the cell's energy reserve, which the cell accesses in response to increased stress or workload.[37] We hypothesized that the higher SRC observed in Mito⁺ cells would provide the energetic advantage to thrive in harsh microenvironments, such as tumors, and additionally compensate for any loss of mitochondria to cancer cells that would have led to a loss of T cell viability. We generated Mito⁺ and Mito⁻ pmel-1 CD8⁺ T cells, which express a transgenic T cell receptor (TCR) recognizing the melanoma antigen, gp100, and transferred them into irradiated mice bearing subcutaneous $B16_{KVP}$ melanoma.[38] Strikingly, Mito⁺ cells mediated a more robust tumor regression compared with Mito⁻ cells (Figure 4A), significantly prolonging mouse survival (Figure 4B). Importantly, the enhanced antitumor responses mediated by Mito⁺ cells were not due to a skewing of memory and effector

$CD8^+$ T cell subsets as assessed by scRNA-seq and flow cytometry (Figures S4A and S4B). Moreover, similar results were observed using immunodeficient NCG mice as tumor-bearing hosts, ruling out the contribution of endogenous immune cells to the observed therapeutic outcome (Figure S5).

To gain further insight into the cellular mechanisms behind the augmented antitumor efficacy of $Mito^+$ cells, we administered $Mito^+$ and $Mito^-$ pmel-1 $CD8^+$ T cells carrying the Ly5.1 congenic marker to enable tracking of transferred cells into tumor-bearing wild-type mice. 7 days after adoptive transfer, we found increased frequencies of pmel-1 cells in the spleens of mice that received $Mito^+$ cells, indicating that transferred mitochondria confer more robust cell engraftment and expansion (Figures 4C and 4D). Similarly, we measured higher numbers of pmel-1 cells in tumors harvested from $Mito^+$ cell-treated mice (Figures 4E and 4F). Notably, $Mito^+$ cells infiltrated tumors efficiently, whereas $Mito^-$ cells were excluded from tumors and largely confined at the tumor periphery (Figure 4F). Interestingly, we could still detect dsRed-labeled mitochondria within a fraction of tumor-infiltrating $Mito^+Ly5.1^+$ cells (Figure 4G). Of note, we did not observe dsRed-labeled mitochondria within non-immune ($Ly5.1^-Ly5.2^-$) components of B16 tumors (Figure 4H), indicating that mitochondria hijacking by tumor cells[14] is not relevant in our experimental system. Indeed, the acquisition of exogenous mitochondria by $CD8^+$ T cells was not detrimental to the treatment but conferred a therapeutic advantage (Figures 4A and 4B).

Experiments tracking cell proliferation with Cell Trace Violet (CTV) showed that both $Mito^+$ and $Mito^-$ cells infiltrating the tumors had proliferated extensively as demonstrated by the complete dilution of the labeling dye (Figure 4I). This robust proliferation also characterized $Mito^+$ cells that retained dsRed-labeled mitochondria, indicating that transferred mitochondria can be inherited to daughter cells across multiple cell divisions, potentially providing long-term benefits to the recipient cells. Having found no significant differences in CTV dilution between $Mito^+$ and $Mito^-$ cells, we sought to determine if the increased numbers of $Mito^+$ cells observed in the tumors were supported by advantages in cell survival. Measuring apoptosis with annexin V revealed that $Mito^-$ underwent massive apoptosis in the tumors in contrast to only a minority of $Mito^+$ cells that experienced apoptotic death (Figures 4J and 4K).

Given that mitochondrial loss and dysfunction are potent drivers of T cell exhaustion,[4,5,7] we sought to determine whether mitochondrial transfer conveys resistance to terminal exhaustion while supporting the differentiation of highly functional effectors by performing scRNA-seq of pmel-1 T cells infiltrating $B16_{KVP}$ tumors. Pmel-1 T cells were isolated 7 days after transfer when there were no notable differences in tumor size between $Mito^+$ and $Mito^-$ groups. We identified four major clusters by Louvain clustering (Figure 5A; Table S6). $Mito^+$ cells were distributed across clusters 0, 1, and 2, whereas $Mito^-$ cells were mostly confined within cluster 3 (Figure 5B). To determine the nature of the clusters, we used a mouse TIL atlas consisting of 16,803 single-cell transcriptomes from B16 melanoma and MC38 colon adenocarcinoma from ProjecTILs[39] integrated with a $CD8^+$ T cell proliferation signature dataset from Pauken et al.[40] This analysis showed that cluster 3, which is enriched in $Mito^-$ cells, displayed a mixture of progenitor exhausted (T_{PEX}) and terminal exhausted (T_{EX}) T cell signatures (Figure 5C). Consistently, this $Mito^-$ cluster expressed higher levels of the co-inhibitory receptors *Pdcd1*, *Lag3*, and *Havcr2* (Figure 5D). T_{PEX} cells were also abundantly present in cluster 2, which is enriched with $Mito^+$ cells. However, the majority of $Mito^+$ cells exhibited effector memory and proliferating cell signatures found in clusters 0 and 1, respectively. Accordingly, cluster 0 expressed higher amounts of effector molecules, *Gzmb*, *Gzma*, and *Fasl* (Figure 5G). In summary, the scRNA-seq study indicates that transferred mitochondria promote potent effector responses while conferring resistance to terminal exhaustion within the tumor microenvironment.

To confirm these findings at the protein level, we performed high-dimensional flow cytometry and employed an unsupervised clustering algorithm to analyze the merged datasets in FlowJo.[41] FlowSOM identified three different pmel-1 T cell subpopulations (Figures S6A and S6B). Consistent with our scRNA-seq, we found higher frequencies of $PD\text{-}1^{hi}LAG3^{hi}$ T_{EX} cells in $Mito^-$ compared with $Mito^+$ cells, which instead contained a larger population of cells with low/intermediate levels of these inhibitory receptors (Figures 5E, 5F, and S6C–S6E). Similarly, TIGIT expression was lower in $Mito^+$ cells, further supporting the idea that donor mitochondria promote resistance of $CD8^+$ T cells to terminal exhaustion (Figures S6F–S6H). In line with this view, there was an inverse correlation ($R = -0.54$, $p = 0.0376$) between the percentage of dsRed-retaining cells and the levels of PD-1 in intratumoral pmel-1 cells (Figure S6I). Flow cytometry analyses also revealed a significantly higher portion of $PD\text{-}1^{hi}Gzmb^{low}$ cells in $Mito^-$ cells compared with $Mito^+$ cells (Figure S6J). By contrast, the $Mito^+$ group exhibited higher frequencies of $PD\text{-}1^{low/int}Gzmb^{hi}$ cells (Figures 5H and 5I), indicating that mitochondria-boosted $CD8^+$ T cells are more functionally active in the tumor microenvironment. These data were further supported by the detection of higher frequencies of terminally differentiated effector cells ($KLRG1^{hi}IL7R\alpha^{low}$) in $Mito^+$ cells, which are necessary for tumor killing and clearance (Figures S6K–S6O). Collectively, functional, proteomic, and transcriptomic findings indicate that the acquisition of donor mitochondria by $CD8^+$ T cells provides significant advantages in terms of cell expansion, survival, tumor penetration, resistance to exhaustion, and differentiation into highly functional killers.

In addition, we examined the spleens of the tumor-bearing mice to assess whether BMSC mitochondrial transfer affects T cell differentiation and function outside the tumor microenvironment. scRNA-seq revealed distinct cluster distributions for $Mito^+$ and $Mito^-$ cells (Figures 5J and 5K; Table S7). Classification of cell types based on ProjecTILs[39] and Pauken[40] signatures showed a unique enrichment of naive-like T cells in $Mito^+$ cell-associated cluster 1 (Figure 5L). The majority of cells in both groups exhibited an effector memory signature (Figure 5L). Notably, there were minor differences in the expression of co-inhibitory receptors (Figure 5M) but no evidence of cell exhaustion signatures (Figure 5L). This outcome was also observed in flow cytometry datasets (Figures 5N and 5O) and is not unexpected given that cells in the spleen are not exposed to chronic antigen stimulation and the pro-exhaustion cues found in the tumor microenvironment.

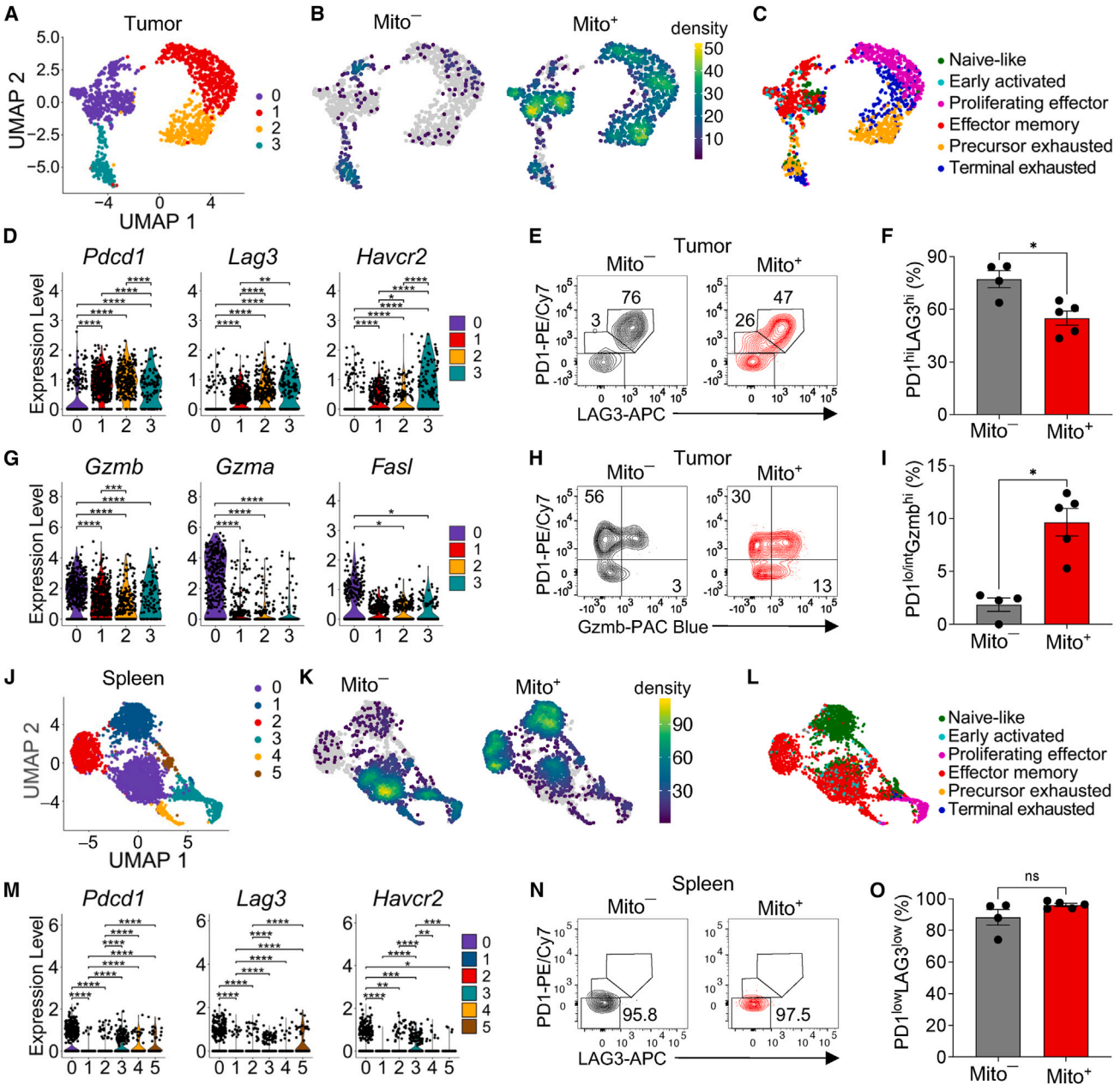

Figure 5. Mitochondrial transfer counteracts CD8⁺ T cell exhaustion, promoting effective effector responses

(A and J) Uniform manifold approximation and projection (UMAP) plot showing concatenated tumor-infiltrating (A) and splenic (J) pmel-1 Mito$^+$ and Mito$^-$ T cells 7 days after tumor treatment as described in Figure 4A.

(B and K) Density plot of pmel-1 Mito$^+$ and Mito$^-$ T cells as in (A) and (J).

(C and L) T cell subtype classification by ProjecTILs[39] integrated with the Pauken proliferation signature dataset.[40]

(D, G, and M) Violin plots showing the expression levels of exhaustion markers (D and M) and cytotoxic molecules (G) in each cluster.

(E, F, H, I, N, and O) Flow cytometry plots (E, H, and N) and frequencies (F, I, and O) of Mito$^+$ and Mito$^-$ pmel-1 Ly5.1$^+$CD8$^+$ T cells expressing the indicated combination of PD-1 and LAG3 (F and O) or PD-1 and Gzmb (I) 7 days after treatment as in (A) and (J). Data shown in (F), (I), and (O) are mean ± SEM (n = 4–5 biological replicates). ns, not significant; *$p < 0.05$ (unpaired two-tailed Student's t test; F, I, and O), *$p < 0.05$; **$p < 0.01$; ***$p < 0.001$, ****$p < 0.0001$ (Wilcoxon test followed by Benjamini Hochberg multiple-comparison test; D, G, and M).

See also Figure S6.

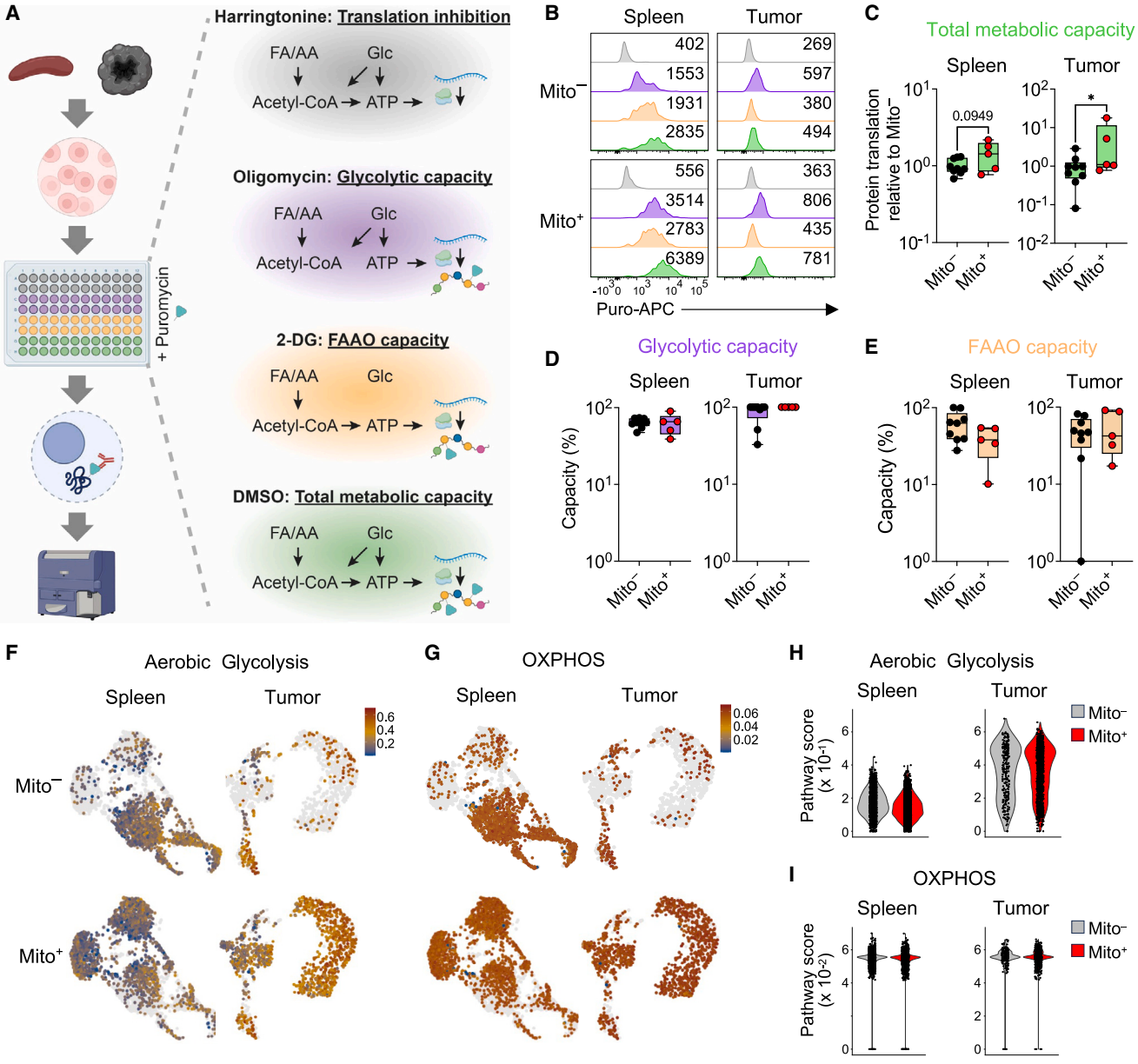

Figure 6. Mitochondrial transfer enhances CD8⁺ T cell metabolism within the tumor microenvironment

(A) Schematic representation of the SCENITH assay. Cells are incubated with DMSO (green), 2-DG (orange), oligomycin (purple), or harringtonine (gray) to inhibit the respective metabolic pathways before energy levels are read out by puromycin incorporation. 2-DG, 2-deoxy-D-glucose; DMSO, dimethyl sulfoxide; FA, fatty acid; aa, amino acid; FAAO, fatty acid and amino acid oxidation.

(B) Histogram plots showing puromycin incorporation by splenic and intratumoral pmel-1 Mito⁺ and Mito⁻ T cells 7 days after tumor treatment as described in Figure 4A (n = 5–9, from two pooled independent experiments).

(C–E) (C) Total metabolic capacity, (D) glycolytic capacity, and (E) FAAO capacity of splenic and intra-tumoral pmel-1 Mito⁺ and Mito⁻ T cells as assessed with SCENITH (n = 5–9). Boxes and lines (C–E) represent interquartile range and median, respectively; whiskers extend to minimum and maximum values.

(F and G) UMAP plots of splenic and intratumoral pmel-1 Mito⁺ and Mito⁻ T cells, color-coded by GSVA-based metabolic signatures.[43]

(H and I) Violin plots showing aerobic glycolysis (H) and oxidative phosphorylation (OXPHOS) (I) pathway scores. p = 0.0949; *p < 0.05 (unpaired one-tailed Student's t test, C).

See also Figure S7.

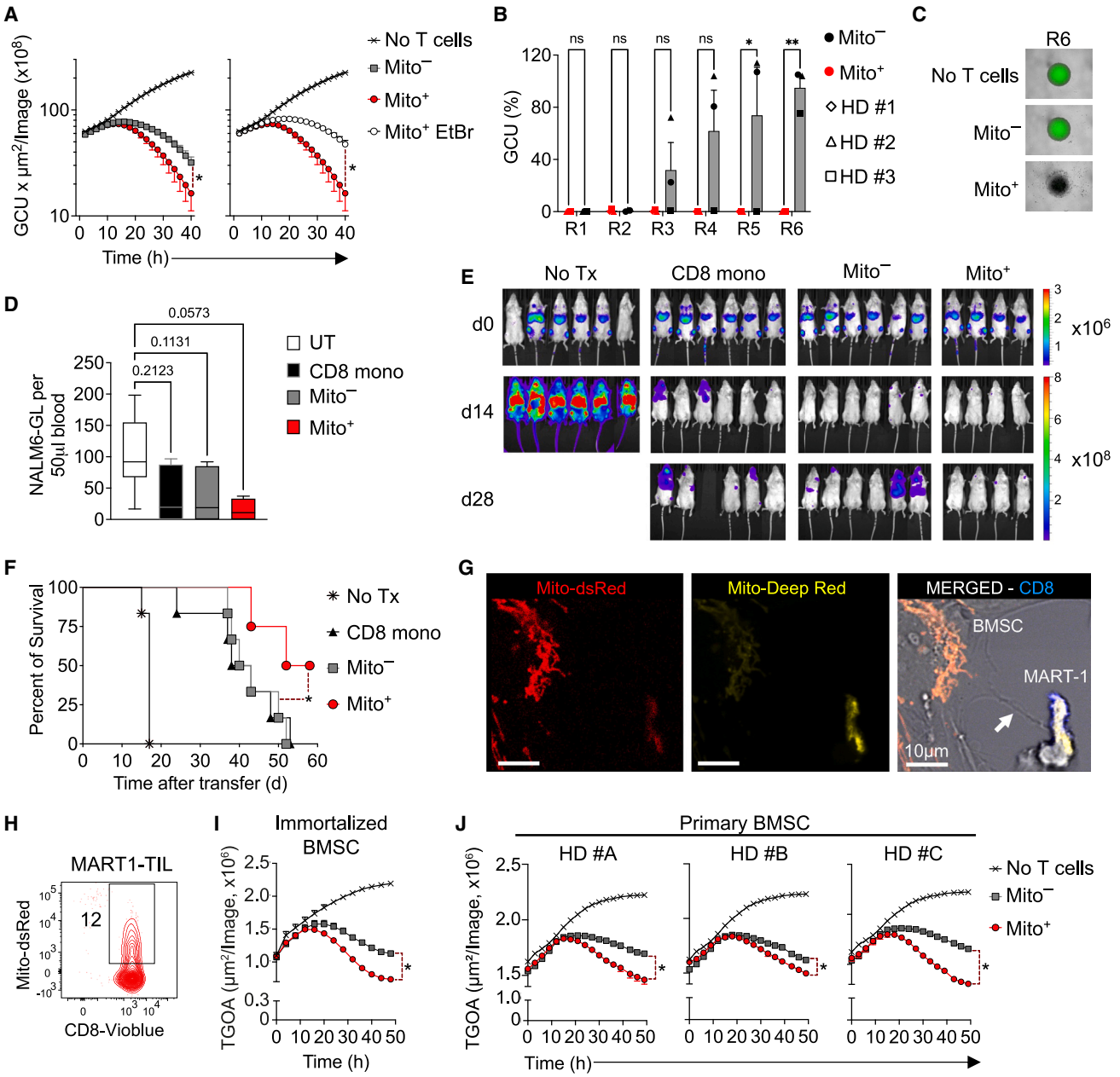

Figure 7. Mitochondrial transfer enhances human CD19-CAR CD8⁺ T cell antitumor immunity against systemic leukemia xenografts

(A) Cytotoxicity assay using CD19-CAR Mito⁻ or Mito⁺ cells after co-culture with Mito-dsRed BMSCs that were left untreated or pre-treated ethidium bromide (EtBr) to render donor mitochondria dysfunctional. Data show green calibrated unit (GCU) per µm²/image means ± SEM after co-culture with NALM6-GL leukemia (E:T ratio 1:5) (n = 3 technical replicates per group).

(B) Repetitive cytotoxicity assay using CD19-CAR Mito⁻ or Mito⁺ cells against NALM6-GL leukemia (E:T ratio 1:1). Data show final GCU means ± SEM for each round of stimulation (n = 3 healthy donor [HD] replicates per group).

(C) Representative image of effector T cells:NALM6-GL leukemia co-cultures after six rounds of stimulation. Top row shows NALM6-GL cells alone.

(D) Numbers of circulating NALM6-GL cells per 50 µL of blood 7 days after transfer of 1.25 × 10^5 CD19-CAR Mito⁻ or Mito⁺ cells or CD19-CAR CD8 monocultured in conjunction with recombinant human IL-15 into sublethally irradiated NXG mice bearing NALM6-GL leukemia (n = 4–6 biological replicates).

(E and F) (E) *In vivo* bioluminescent imaging and (F) survival of NALM6-GL-bearing NXG mice treated as in (C) (n = 4 or 6 mice/group). No Tx, no treatment (n = 6).

(G) Confocal microscopy image of Mito-dsRed-BMSC pre-stained with MitoTracker DeepRed co-cultured with MART-1 TILs probed with anti-CD8-VioBlue antibody. Scale bar is 10 µm.

(H) Flow cytometry plot of MART-1 TILs 48 h after co-culture with Mito-dsRed BMSCs. Numbers indicate the percentage of Mito-dsRed positive cells after gating on live lymphocytes.

(legend continued on next page)

Mitochondrial transfer enhances CD8$^+$ T cell metabolism in the tumor microenvironment

We next sought to determine whether the metabolic benefits provided by the augmented mitochondrial mass in Mito$^+$ cells impact CD8$^+$ T cell metabolism *in vivo* following adoptive transfer. To this end, we used SCENITH (single cell energetic metabolism by profiling translation inhibition), a flow cytometry-based method that enables metabolic profiling of samples *ex vivo*.[42] The assay measures *de novo* protein synthesis as a surrogate marker for ATP production, as it is one of the most energy-consuming metabolic activities performed by a cell (Figure 6A). Exposure of live cells to inhibitors that target and shut down specific metabolic pathways provides further information on the cell potential to engage aerobic glycolysis (i.e., oligomycin) or fatty acids and amino acids oxidation (FAAO) (i.e., 2-deoxy-D-glucose [2-DG]) (Figure 6A). We found that even 7 days after transfer, Mito$^+$ cells showed a tendency to maintain a metabolic edge over Mito$^-$ cells in the spleen ($p = 0.0949$) (Figures 6B and 6C). Within $B16_{KVP}$ tumors, pmel-1 T cells overall exhibited a lower metabolic activity than in the spleen, likely as a result of the limited availability of nutrients and hypoxic conditions.[44] However, under these harsh circumstances, the metabolic differences between Mito$^+$ and Mito$^-$ cells became more pronounced (Figures 6B and 6C), emphasizing the advantage conferred by the transferred mitochondria in such hostile microenvironments. The heightened protein translation capacity is consistent with the higher frequency of proliferating T cells in the Mito$^+$ cell cohort observed in our scRNA-seq study (Figure 5C). Both cell types displayed similar glycolytic and fatty acid and amino acid oxidation (FAAO) capacities within each of the respective tissues (Figures 6D and 6E). However, intratumoral pmel-1 T cells exhibited higher glycolytic capacities compared with those found in the spleen (Figure 6D), a typical feature of proliferating T cells that, akin to cancer cells, adopt a Warburg metabolism profile to generate building blocks to sustain their exponential growth.[44] These conclusions were further corroborated by our scRNA-seq datasets, which revealed higher expression of genes associated with aerobic glycolysis[43] in intratumoral compared with splenic pmel-1 T cells (Figures 6F and 6H). By contrast, oxidative phosphorylation (OXPHOS) remained mostly unaffected across different sites and conditions (Figures 6G and 6I). Taken together, these *in vivo* metabolic studies demonstrate that the mitochondrial transfer empowers CD8$^+$ T cells to sustain elevated metabolic rates within the tumor microenvironment, without significantly altering the cells' metabolic profile, which instead relies more on the tissue type where the T cells are located.

Mitochondrial transfer augments CD8$^+$ T cell mitochondrial mass long-term boosting cell persistence

To explore whether the advantages provided by mitochondrial transfer are maintained long-term and across successive divisions, we tracked cells undergoing lymphodepletion-driven homeostatic expansion for 1 month in non-tumor-bearing hosts and evaluated them using a combination of CTV and MitoTracker Green quantification. Similar to day 7 results in tumor-bearing mice, we observed higher frequencies of adoptively transferred cells in the Mito$^+$ group associated with increased proliferation, as indicated by CTV dilution (Figures S7A–S7D). This extensive proliferation also characterized a fraction of Mito$^+$ cells that retained Mito-dsRed labeling indicating again that transferred mitochondria can be passed to daughter cells across repetitive divisions (Figure S7E). Indeed, quantification of mitochondrial mass by MitoTracker Green revealed that Mito$^+$ cells had higher mitochondrial content than Mito$^-$ cells 1 month after transfer (Figures S7F and S7G) and that this advantage was maintained throughout multiple divisions (Figures S7H and S7I). These results indicate that the advantages provided by mitochondrial transfer are not merely short-term but persist over an extended period.

Mitochondrial transfer enhances human CD19-CAR T cell and TIL antitumor immunity

To assess whether mitochondrial transfer could also improve human antitumor T cell efficacy, we transduced human CD8$^+$ T cells with a retroviral construct encoding a CD19-specific chimeric antigen receptor (CAR) and co-cultured them with a Mito-dsRed immortalized BMSC line. We initially evaluated the cytotoxic capacity of CD19-CAR T cells *in vitro* against fluorescently labeled NALM6, an aggressive CD19$^+$ human B cell lymphoblastic leukemia (B-ALL) cell line[45] transduced with GFP-luciferase (GL). Compared with Mito$^-$ cells, Mito$^+$ cells demonstrated significantly increased tumor-killing capacity (Figure 7A). Strikingly, the transfer of dysfunctional mitochondria (Mito$^+$ EtBr) did not enhance antitumor activity, once again demonstrating that the superior functionality observed in Mito$^+$ cells is driven by donor mitochondria (Figure 7A). To determine if mitochondrial transfer confers resistance of CD19-CAR T cells to exhaustion, we evaluated the capacity of Mito$^+$ cells to kill NALM6-GL leukemia cells upon repetitive challenges. Mito$^+$ cells maintained robust cytotoxic activity against cancer cells throughout six rounds of stimulation, while Mito$^-$ cells began losing killing capacity at round three and became almost completely functionally exhausted by round six (Figures 7B and 7C). Next, we assessed the antitumor efficacy of CD19-CAR T cells *in vivo* by transferring cells into NXG mice bearing systemic acute lymphoblastic leukemia.[9] 7 days after transfer, we detected lower numbers of circulating leukemic cells in mice receiving CD19-CAR Mito$^+$ cells compared with the untreated group ($p = 0.0573$), whereas transferring Mito$^-$ cells or CD19-CAR CD8 monocultured cells had only a minor impact on tumor burden in the blood (Figure 7D). Mito$^+$ cell enhanced antitumor activity resulted in prolonged control of NALM6-GL leukemia (Figure 7E) and significantly increased mouse survival compared with both Mito$^-$ and conventional monocultured CAR CD8$^+$ T cells (Figure 7F). It is important to note that also in the human

(I and J) Cytotoxicity assay using Mito$^-$ or Mito$^+$ MART-1 TILs against SK23-GFP melanoma (E:T ratio 1:5). Donor mitochondria were derived from immortalized (I) or primary (J) BMSCs.

Data show target green object area (TGOA) per μm^2/image mean ± SEM. $n = 3$ technical replicates per group. Kruskal-Wallis test, I; $^*p < 0.05$ (Wilcoxon test: A, I, and J; two-way ANOVA, Šídák's multiple comparisons test: B; log-rank [Mantel-Cox] test: F); $^{**}p < 0.01$ (two-way ANOVA, Šídák's multiple comparisons test). See also Figure S4.

setting, we did not observe significant skewing of memory and effector CD8$^+$ T cell subsets in the pre-infusion product, indicating the superior antitumor responses by the Mito$^+$ cells were mediated by the augmented mitochondrial content (Figure S4C).

The capacity to transplant healthy mitochondria might be particularly relevant for TIL application, as their endogenous mitochondria often are irreparably damaged by the hostile conditions found in the tumor microenvironment. To evaluate the impact of mitochondrial transfer on TIL function, we co-cultured a previously described TIL product, MART-1,[46] with Mito-dsRed BMSC. TILs were also able to acquire donor mitochondria with moderate efficiency (Figures 7G and 7H). When challenged with SK23-GFP, a melanoma cell line expressing the target antigen MART-1, Mito$^+$ TILs mediated enhanced tumor clearance compared with their Mito$^-$ counterparts (Figure 7I). To explore whether donor mitochondria can also be sourced from primary BMSCs, we co-cultured MART-1 TILs with clinical-grade primary BMSCs generated from three different donors. Despite mild inter-donor variations, Mito$^+$ TILs consistently exhibited enhanced cytotoxicity against target cancer cells (Figure 7J). Taken together, these findings highlight the translational potential of our mitochondrial transfer technology platform and provide initial proof of concept for the feasibility of using patient-matched BMSCs in a fully autologous co-culture system.

DISCUSSION

Organelle medicine, or organelle transplantation, is an emerging research area, wherein similar to traditional organ transplants in patients, organelles are transferred to recipient cells to improve cellular function.[47] Mitochondrial transfer is the form of organelle transplantation most studied.[17,48] Technology platforms based on the transfer of isolated mitochondria are more prevalent in the field. These methods include the use of mechanical force,[49] coating with artificial lipid membranes,[50] or microinjection[51] to increase mitochondria uptake by recipient cells. The application of mitochondrial transfer in T cell therapy has yet to be explored. However, given the close link between mitochondrial fitness and CD8$^+$ T cell expansion, persistence, and antitumor effector function,[8,10,11,37,52,53] it holds great promise for enhancing the efficacy of cancer immunotherapies. Preclinical and clinical studies of adoptive T cell therapy have shown that the metabolic qualities of the infusion products, and particularly their mitochondrial function, are critical determinants of patients' outcomes.[8,10,11,54] Unfortunately, patient or donor T cell mitochondria can become damaged and dysfunctional, impairing their capacity to energetically sustain the fight against cancer cells upon transfer of these "living drugs."[55] Indeed, mtDNA is up to 10 times more prone to accumulate damage than nuclear DNA.[56] Approximately 60% of cancer cases occur in patients aged 65 and above,[57] increasing the likelihood of accumulated mtDNA mutations. Moreover, mitochondrial biomass and activity in T cells sharply decrease with age.[58,59] Prior systemic treatments, including chemo- and radiotherapy, can also have detrimental effects on the mitochondrial function of patients' T cells.[60,61] Thus, the ability to transplant healthy mitochondria can have a profound impact on several cancer immunotherapy platforms, such as those relying on autologous T cell sources and, in particular, on TILs whose mitochondria have been damaged by the hostile tumor microenvironment.[3–6]

Our results provide proof of concept that BMSC mitochondrial transfer can be successfully utilized to potentiate the antitumor efficacy of both mouse and human CD8$^+$ T cells. The enhanced antitumor responses were observed across a variety of different T cell platforms (TCR, CAR, and TILs) in diverse *in vitro* and *in vivo* settings (syngeneic/human xenograft) against both liquid and solid tumors. Mitochondrial transfer from donor BMSCs had a profound impact on antitumor CD8$^+$ T cells; it enhanced their survival, facilitated robust expansion, improved efficiency in infiltrating the tumor mass, conferred resistance to exhaustion, and promoted differentiation into potent cytotoxic effector cells. Interestingly, a high portion of cells that were prone to exhaustion in the group that received BMSC mitochondria showed reduced expression levels of PD-1, LAG3, and TIGIT. As this cell population can be rescued more efficiently by PD-1:PD-L1 blockade compared with terminally exhausted PD-1^{hi}LAG3^{hi}TIGIT^{hi},[62,63] it may be beneficial in the future to couple mitochondria-boosted T cell therapies with immune checkpoint inhibitors. Extending mitochondrial transfer technology to infusion products comprising CD4$^+$ T cells warrants caution given that donor mitochondria have been shown to promote regulatory T cell (Treg) differentiation.[64] This is particularly relevant considering recent evidence that CAR CD4$^+$ Treg cells in infusion products have been associated with clinical progression.[65,66]

We focused our research effort on using BMSCs as a donor source, as these cells present several advantages compared with other cell types. For instance, they show low surface expression levels of human leukocyte antigen (HLA) molecules, facilitating their use in allogeneic co-culture settings.[19] Moreover, *ex vivo* clinical-grade manufacturing and expansion protocols have been established for BMSCs, easing the transition to the clinic.[19] Future work will be needed to elucidate whether the source and quality of transferred mitochondria are also critical for bolstering T cell antitumor function. Indeed, it is becoming increasingly appreciated in the field that distinct "mitotypes" with different specializations exist within a cell.[67]

A compelling aspect of mitochondrial transfer technology is its capability to impart enduring benefits to recipient T cells. We observed that the increased mitochondrial mass resulting from the acquired mitochondria can be maintained long-term across multiple divisions. These results are in line with previous observations *in vitro* showing that transferred mitochondria can be propagated across numerous cell divisions in a cancer cell line.[51] Interestingly, in the same study, acquired mitochondria exhibited greater persistence when transferred via cell-to-cell interactions rather than microinjection of isolated mitochondria, indicating that leveraging endogenous mechanisms is superior to artificial manipulation for the long-term engraftment of donor mitochondria.[51] Our *ex vivo* scRNA-seq findings also underscore that mitochondrial transfer has profound and long-lasting effects on T cell differentiation trajectories. Mitochondria are crucial sources of essential cofactors for histone and genome modifications; thus, their number and function can significantly influence

the cell's epigenetic landscape, resulting in heritable alterations in gene expression.[67] The capacity of transferred mitochondria to trigger hardwired reprogramming of T cell fates is particularly relevant for T cell therapies, where adoptively transferred T cells can undergo substantial expansion within the patient's body.

Lastly, the mitochondria transfer approach offers the advantage of enhancing the quality of mitochondria without requiring direct interventions on T cells that may negatively affect the final infusion product. For example, rapamycin can promote mitochondrial remodeling[68,69] but stunts T cell proliferation,[70] limiting the generation of therapeutic T cell doses. Altogether, these findings establish intercellular mitochondrial transfer as a promising organelle-based technology platform to improve the outcomes of patients receiving next-generation cell therapies.

Limitations of the study

Clinical translation of these results will require further research into identifying surrogate marker(s) of mitochondria transfer or significantly increasing the transfer rate. Currently, fluorescent labels are used for tracking mitochondria transfer; however, this approach is not applicable in the clinic. The identification of a surrogate marker to enrich cells that acquire donor mitochondria would avoid the need to pre-label mitochondria. Perhaps a bigger limitation of mitochondrial transfer in $CD8^+$ T cells is the currently modest transfer rate (~10%), which may prevent scaling up the technology to clinically relevant cell doses. The mechanistic data derived from our study provide the blueprint for future work aiming at increasing transfer efficiency. Targeting the TLN2 machinery or other identified molecules in this study could help to overcome this limitation and even mitigate the need for downstream cell selection. In addition, determining if there are subset(s) of BMSC that are primarily responsible for mitochondrial transfer ("super donor") could assist efforts in scaling up this platform.

RESOURCE AVAILABILITY

Lead contact

Further information and requests for resources and reagents should be directed to and will be fulfilled by the lead contact, Prof. Luca Gattinoni (luca.gattinoni@lit.eu).

Materials availability

The cell lines generated during this study are available upon request.

Data and code availability

- Mouse bulk and single-cell RNA sequencing data are available from GEO: GSE229487 and GSE25419, respectively. Human bulk RNA sequencing and ID data are available at EGA: EGAS00001007356 and EGAD00001011082, respectively.
- All software and packages used were publicly accessible, and this study does not report original codes.
- Any additional information required to reanalyze the data reported in this paper is available from the lead contact upon request.

ACKNOWLEDGMENTS

This research was supported by the NIH Intramural Research Program through an NCI FLEX award to L.G., the CRI Clinic and Laboratory Integration Program (CLIP) (CRI3201), and the DFG Reinhart Koselleck project (GA 2882/2-1). J.G.B.'s work was supported by the Joachim Herz Foundation (Add-on Fellowship) and the Fulbright Future Fellowship by the Australian Fulbright Commission and The Kinghorn Foundation. M.I. is supported by the European Research Council (ERC) Consolidator Grant 725038, ERC Proof of Concept Grant 957502, Italian Association for Cancer Research (AIRC) grants 19891 and 22737, Italian Ministry of Health grants RF-2018-12365801, EU funding within the NextGeneration EU-MUR PNRR Extended Partnership initiative on Emerging Infectious Diseases (project no. PE00000007, INF-ACT), and Funded Research Agreements from Gilead Sciences, Asher Bio, Takis Biotech, and Vir Biotechnology. D.I. is supported by the Italian Association for Cancer Research (AIRC, grant 26183) and by the European Commission (FET-open grant 964481). M.X. is supported by the "SATURN3 – Spatial And Temporal Resolution of Intratumoral Heterogeneity in 3 hard-to-treat CaNcers" in the BMBF funding line joint research on "Tumor Heterogeneity, Clonal Tumor Evolution and Therapy Resistance." K.S. is supported by the German Federal Ministry of Education and Research (BMBF, projects 01KI2013 and 031L0290B), the Else Kröner-Fresenius-Stiftung (project 2020_EKEA.127), and the German Research Foundation (DFG) through the research training group RTG 2504 (project 401821119). S.S. is supported by the NIH Research Project Grant Program (R01CA276525 and R01CA293908). Sequencing and bioinformatic analysis were conducted at the NGS & Data Technologies Core Unit of the Leibniz Institute of Immunotherapy (LIT), Germany (https://lit.eu/facilities/ngs-and-data-technologies). We thank Pamela G. Robey for providing the spontaneously immortalized mBMSC line DM5, ALEMBIC facility at San Raffaele Scientific Institute, Milan, Italy, and in particular Valeria Berno for support in CLEM analysis. We would like to thank Patrick Grandinetti for his assistance with irradiating mice at the NIH animal facility. We would like to add a special thanks to Jaqueline Dirmeier and Irina Fink from FACS-Analytics and Cell Sorting at the LIT for their assistance with cell sorting. The graphical abstract and Figures 2A and 6A panels were created with BioRender.com.

AUTHOR CONTRIBUTIONS

J.G.B., C.H.-L., T.S., R.C.S., D.S.-L., M.B., F.M., A.M.-S., A.R., P. Brohawn, V.K., W.G.T., S.G., S.F., Z.K., and J.F. performed the experiments. J.G.B., C.H.-L., T.S., D.S.-L., N.S., M.B., F.M., A.M.-S., A.R., B.W.H., S.G., I.H.-L., N.R., Z.K., D.I., J.F., and L.G. analyzed the experiments. J.G.B., C.H.-L., T.S., R.C.S., D.S.-L., N.S., C.G., S.G., M.X., P. Beckhove, K.S., Z.K., J.E.C., M.I., D.I., M.R., J.F., S.S., and L.G. designed the experiments. J.G.B. and L.G. wrote the manuscript. All authors read, edited, and approved the article.

DECLARATION OF INTERESTS

J.G.B., T.S., J.F., S.S., and L.G. have a patent application for the use of mitochondrial transfer technology in cancer immunotherapies. P.B. and S.G. have an employee relationship and have stock in AstraZeneca. B.W.H. has an employee relationship and has stock in Genmab. L.G. has consulting agreements with Lyell Immunopharma, Instil Bio, and Advaxis. L.G. is on the scientific advisory board of Poseida Therapeutics and Kiromic and a stockholder of Poseida Therapeutics. M.I. participates in advisory boards/consultancies for Gilead Sciences, Third Rock Ventures, Antios Therapeutics, Asher Biotherapeutics, GentiBio, Clexio Biosciences, Sybilla, and BlueJay Therapeutics. J.F. has an employee relationship and has stock in Lyell Immunopharma. S.S. is a founder and owns equity in Vyome Therapeutics Inc. and Alyssum Therapeutics Inc.

STAR★METHODS

Detailed methods are provided in the online version of this paper and include the following:

- KEY RESOURCES TABLE
- EXPERIMENTAL MODEL AND SUBJECT DETAILS
  - Cell lines
  - Experimental Animals
- METHOD DETAILS
  - Antibodies, flow cytometry, and cell sorting
  - Scanning electron microscopy of nanotubes

- Fluorescence microscopy of BMSC-CD8$^+$ T cell cocultures
- Murine co-culture system platform
- Incubation of T cells with isolated mitochondria
- Human co-culture system platform
- Confocal imaging of sorted cells
- Quantification of mtDNA content
- Generation of BMSC lines with partially dysfunctional donor mitochondria
- Correlative light-electron microscopy
- Restriction enzyme analysis of mtDNA
- Mitochondria Stress Test assay
- Bulk RNA-sequencing
- Bioinformatic analysis of bulk RNA-sequencing data
- CRISPR-Cas9 *TLN2* knockout
- DISCOVER-seq
- Amplicon sequencing and genome editing analysis
- Inhibitor treatment study
- Murine syngeneic melanoma model
- Frozen immunohistochemistry
- Quantification and phenotype of adoptively transferred CD8$^+$ T cells
- Short and long-term *in vivo* functionality assays
- Single-cell RNA-sequencing
- Bioinformatic analysis of single-cell RNA-sequencing data
- SCENITH
- Quantification of *TLN2* expression
- Human *in vitro* cytotoxicity assay
- Repetitive *in vitro* cytotoxicity assay
- Humanized B-cell malignancy model

- QUANTIFICATION AND STATISTICAL ANALYSIS

SUPPLEMENTAL INFORMATION

Supplemental information can be found online at https://doi.org/10.1016/j.cell.2024.08.029.

Received: April 7, 2023
Revised: February 20, 2024
Accepted: August 14, 2024
Published: September 13, 2024

REFERENCES

1. Sadelain, M., Rivière, I., and Riddell, S. (2017). Therapeutic T cell engineering. Nature *545*, 423–431. https://doi.org/10.1038/nature22395.
2. Finck, A.V., Blanchard, T., Roselle, C.P., Golinelli, G., and June, C.H. (2022). Engineered cellular immunotherapies in cancer and beyond. Nat. Med. *28*, 678–689. https://doi.org/10.1038/s41591-022-01765-8.
3. Scharping, N.E., Rivadeneira, D.B., Menk, A.V., Vignali, P.D.A., Ford, B.R., Rittenhouse, N.L., Peralta, R., Wang, Y., Wang, Y., DePeaux, K., et al. (2021). Mitochondrial stress induced by continuous stimulation under hypoxia rapidly drives T cell exhaustion. Nat. Immunol. *22*, 205–215. https://doi.org/10.1038/s41590-020-00834-9.
4. Yu, Y.R., Imrichova, H., Wang, H., Chao, T., Xiao, Z., Gao, M., Rincon-Restrepo, M., Franco, F., Genolet, R., Cheng, W.C., et al. (2020). Disturbed mitochondrial dynamics in CD8(+) TILs reinforce T cell exhaustion. Nat. Immunol. *21*, 1540–1551. https://doi.org/10.1038/s41590-020-0793-3.
5. Soto-Heredero, G., Desdín-Micó, G., and Mittelbrunn, M. (2021). Mitochondrial dysfunction defines T cell exhaustion. Cell Metab. *33*, 470–472. https://doi.org/10.1016/j.cmet.2021.02.010.
6. Scharping, N.E., Menk, A.V., Moreci, R.S., Whetstone, R.D., Dadey, R.E., Watkins, S.C., Ferris, R.L., and Delgoffe, G.M. (2016). The tumor microenvironment represses T cell mitochondrial biogenesis to drive intratumoral T cell metabolic insufficiency and dysfunction. Immunity *45*, 374–388. https://doi.org/10.1016/j.immuni.2016.07.009.
7. Wu, H., Zhao, X., Hochrein, S.M., Eckstein, M., Gubert, G.F., Knöpper, K., Mansilla, A.M., Öner, A., Doucet-Ladevèze, R., Schmitz, W., et al. (2023). Mitochondrial dysfunction promotes the transition of precursor to terminally exhausted T cells through HIF-1α-mediated glycolytic reprogramming. Nat. Commun. *14*, 6858. https://doi.org/10.1038/s41467-023-42634-3.
8. Sukumar, M., Liu, J., Mehta, G.U., Patel, S.J., Roychoudhuri, R., Crompton, J.G., Klebanoff, C.A., Ji, Y., Li, P., Yu, Z., et al. (2016). Mitochondrial membrane potential identifies cells with enhanced stemness for cellular therapy. Cell Metab. *23*, 63–76. https://doi.org/10.1016/j.cmet.2015.11.002.
9. Sabatino, M., Hu, J., Sommariva, M., Gautam, S., Fellowes, V., Hocker, J.D., Dougherty, S., Qin, H., Klebanoff, C.A., Fry, T.J., et al. (2016). Generation of clinical-grade CD19-specific CAR-modified CD8+ memory stem cells for the treatment of human B-cell malignancies. Blood *128*, 519–528. https://doi.org/10.1182/blood-2015-11-683847.
10. Dumauthioz, N., Tschumi, B., Wenes, M., Marti, B., Wang, H., Franco, F., Li, W., Lopez-Mejia, I.C., Fajas, L., Ho, P.-C., et al. (2021). Enforced PGC-1α expression promotes CD8 T cell fitness, memory formation and antitumor immunity. Cell. Mol. Immunol. *18*, 1761–1771. https://doi.org/10.1038/s41423-020-0365-3.
11. Pilipow, K., Scamardella, E., Puccio, S., Gautam, S., De Paoli, F., Mazza, E.M., De Simone, G., Polletti, S., Buccilli, M., Zanon, V., et al. (2018). Antioxidant metabolism regulates CD8+ T memory stem cell formation and antitumor immunity. JCI Insight *3*, e122299. https://doi.org/10.1172/jci.insight.122299.
12. Spees, J.L., Olson, S.D., Whitney, M.J., and Prockop, D.J. (2006). Mitochondrial transfer between cells can rescue aerobic respiration. Proc. Natl. Acad. Sci. USA *103*, 1283–1288. https://doi.org/10.1073/pnas.0510511103.
13. Islam, M.N., Das, S.R., Emin, M.T., Wei, M., Sun, L., Westphalen, K., Rowlands, D.J., Quadri, S.K., Bhattacharya, S., and Bhattacharya, J. (2012). Mitochondrial transfer from bone-marrow–derived stromal cells to pulmonary alveoli protects against acute lung injury. Nat. Med. *18*, 759–765. https://doi.org/10.1038/nm.2736.
14. Saha, T., Dash, C., Jayabalan, R., Khiste, S., Kulkarni, A., Kurmi, K., Mondal, J., Majumder, P.K., Bardia, A., Jang, H.L., et al. (2022). Intercellular nanotubes mediate mitochondrial trafficking between cancer and immune cells. Nat. Nanotechnol. *17*, 98–106. https://doi.org/10.1038/s41565-021-01000-4.
15. Marlein, C.R., Zaitseva, L., Piddock, R.E., Robinson, S.D., Edwards, D.R., Shafat, M.S., Zhou, Z., Lawes, M., Bowles, K.M., and Rushworth, S.A. (2017). NADPH oxidase-2 derived superoxide drives mitochondrial transfer from bone marrow stromal cells to leukemic blasts. Blood *130*, 1649–1660. https://doi.org/10.1182/blood-2017-03-772939.
16. Burt, R., Dey, A., Aref, S., Aguiar, M., Akarca, A., Bailey, K., Day, W., Hooper, S., Kirkwood, A., Kirschner, K., et al. (2019). Activated stromal cells transfer mitochondria to rescue acute lymphoblastic leukemia cells from oxidative stress. Blood *134*, 1415–1429. https://doi.org/10.1182/blood.2019001398.
17. Borcherding, N., and Brestoff, J.R. (2023). The power and potential of mitochondria transfer. Nature *623*, 283–291. https://doi.org/10.1038/s41586-023-06537-z.
18. Rustom, A., Saffrich, R., Markovic, I., Walther, P., and Gerdes, H.-H. (2004). Nanotubular highways for intercellular organelle transport. Science *303*, 1007–1010. https://doi.org/10.1126/science.1093133.
19. Uccelli, A., Moretta, L., and Pistoia, V. (2008). Mesenchymal stem cells in health and disease. Nat. Rev. Immunol. *8*, 726–736. https://doi.org/10.1038/nri2395.
20. Chen, X.J., and Butow, R.A. (2005). The organization and inheritance of the mitochondrial genome. Nat. Rev. Genet. *6*, 815–825. https://doi.org/10.1038/nrg1708.
21. Bayona-Bafaluy, M.P., Acín-Pérez, R., Mullikin, J.C., Park, J.S., Moreno-Loshuertos, R., Hu, P., Pérez-Martos, A., Fernández-Silva, P., Bai, Y.,

and Enríquez, J.A. (2003). Revisiting the mouse mitochondrial DNA sequence. Nucleic Acids Res. *31*, 5349–5355. https://doi.org/10.1093/nar/gkg739.

22. Ahmad, T., Mukherjee, S., Pattnaik, B., Kumar, M., Singh, S., Kumar, M., Rehman, R., Tiwari, B.K., Jha, K.A., Barhanpurkar, A.P., et al. (2014). Miro1 regulates intercellular mitochondrial transport & enhances mesenchymal stem cell rescue efficacy. EMBO J. *33*, 994–1010. https://doi.org/10.1002/embj.201386030.
23. Ljubojevic, N., Henderson, J.M., and Zurzolo, C. (2021). The ways of actin: why tunneling nanotubes are unique cell protrusions. Trends Cell Biol. *31*, 130–142. https://doi.org/10.1016/j.tcb.2020.11.008.
24. Zhang, S., Kazanietz, M.G., and Cooke, M. (2020). Rho GTPases and the emerging role of tunneling nanotubes in physiology and disease. Am. J. Physiol. Cell Physiol. *319*, C877–C884. https://doi.org/10.1152/ajpcell.00351.2020.
25. Zhang, H., Yu, X., Ye, J., Li, H., Hu, J., Tan, Y., Fang, Y., Akbay, E., Yu, F., Weng, C., et al. (2023). Systematic investigation of mitochondrial transfer between cancer cells and T cells at single-cell resolution. Cancer Cell *41*, 1788–1802.e10. https://doi.org/10.1016/j.ccell.2023.09.003.
26. Henderson, J.M., Ljubojevic, N., Belian, S., Chaze, T., Castaneda, D., Battistella, A., Giai Gianetto, Q., Matondo, M., Descroix, S., Bassereau, P., et al. (2023). Tunnelling nanotube formation is driven by Eps8/IRSp53-dependent linear actin polymerization. EMBO J. *42*, e113761. https://doi.org/10.15252/embj.2023113761.
27. Zhu, S., Bhat, S., Syan, S., Kuchitsu, Y., Fukuda, M., and Zurzolo, C. (2018). Rab11a–Rab8a cascade regulates the formation of tunneling nanotubes through vesicle recycling. J. Cell Sci. *131*, jcs215889. https://doi.org/10.1242/jcs.215889.
28. Zheng, D., Niu, S., Yu, D., Zhan, X.H., Zeng, X., Cui, B., Chen, Y., Yoon, J., Martin, S.S., Lu, X., et al. (2010). Abba promotes PDGF-mediated membrane ruffling through activation of the small GTPase Rac1. Biochem. Biophys. Res. Commun. *401*, 527–532. https://doi.org/10.1016/j.bbrc.2010.09.087.
29. Begemann, I., Saha, T., Lamparter, L., Rathmann, I., Grill, D., Golbach, L., Rasch, C., Keller, U., Trappmann, B., Matis, M., et al. (2019). Mechanochemical self-organization determines search pattern in migratory cells. Nat. Phys. *15*, 848–857. https://doi.org/10.1038/s41567-019-0505-9.
30. Qi, L., Jafari, N., Li, X., Chen, Z., Li, L., Hytönen, V.P., Goult, B.T., Zhan, C.-G., and Huang, C. (2016). Talin2-mediated traction force drives matrix degradation and cell invasion. J. Cell Sci. *129*, 3661–3674. https://doi.org/10.1242/jcs.185959.
31. Calderwood, D.A., and Ginsberg, M.H. (2003). Talin forges the links between integrins and actin. Nat. Cell Biol. *5*, 694–697. https://doi.org/10.1038/ncb0803-694.
32. Lipsky, B.P., Beals, C.R., and Staunton, D.E. (1998). Leupaxin is a novel LIM domain protein that forms a complex with PYK2. J. Biol. Chem. *273*, 11709–11713. https://doi.org/10.1074/jbc.273.19.11709.
33. Melssen, M.M., Lindsay, R.S., Stasiak, K., Rodriguez, A.B., Briegel, A.M., Cyranowski, S., Rutkowski, M.R., Conaway, M.R., Melief, C.J.M., van der Burg, S.H., et al. (2021). Differential expression of CD49a and CD49b determines localization and function of tumor-infiltrating CD8+ T cells. Cancer Immunol. Res. *9*, 583–597. https://doi.org/10.1158/2326-6066.CIR-20-0427.
34. Pirone, D.M., Fukuhara, S., Gutkind, J.S., and Burbelo, P.D. (2000). SPECs, small binding proteins for Cdc42. J. Biol. Chem. *275*, 22650–22656. https://doi.org/10.1074/jbc.M002832200.
35. Watson, J.R., Owen, D., and Mott, H.R. (2017). Cdc42 in actin dynamics: an ordered pathway governed by complex equilibria and directional effector handover. Small GTPases *8*, 237–244. https://doi.org/10.1080/21541248.2016.1215657.
36. Wienert, B., Wyman, S.K., Yeh, C.D., Conklin, B.R., and Corn, J.E. (2020). CRISPR off-target detection with DISCover-seq. Nat. Protoc. *15*, 1775–1799. https://doi.org/10.1038/s41596-020-0309-5.
37. van der Windt, G.J.W., O'Sullivan, D., Everts, B., Huang, S.C.-C., Buck, M.D., Curtis, J.D., Chang, C.-H., Smith, A.M., Ai, T., Faubert, B., et al. (2013). CD8 memory T cells have a bioenergetic advantage that underlies their rapid recall ability. Proc. Natl. Acad. Sci. USA *110*, 14336–14341. https://doi.org/10.1073/pnas.1221740110.
38. Hanada, K.I., Yu, Z., Chappell, G.R., Park, A.S., and Restifo, N.P. (2019). An effective mouse model for adoptive cancer immunotherapy targeting neoantigens. JCI Insight *4*, e124405. https://doi.org/10.1172/jci.insight.124405.
39. Andreatta, M., Corria-Osorio, J., Müller, S., Cubas, R., Coukos, G., and Carmona, S.J. (2021). Interpretation of T cell states from single-cell transcriptomics data using reference atlases. Nat. Commun. *12*, 2965. https://doi.org/10.1038/s41467-021-23324-4.
40. Pauken, K.E., Shahid, O., Lagattuta, K.A., Mahuron, K.M., Luber, J.M., Lowe, M.M., Huang, L., Delaney, C., Long, J.M., Fung, M.E., et al. (2021). Single-cell analyses identify circulating anti-tumor CD8 T cells and markers for their enrichment. J. Exp. Med. *218*, e20200920. https://doi.org/10.1084/jem.20200920.
41. Van Gassen, S., Callebaut, B., Van Helden, M.J., Lambrecht, B.N., Demeester, P., Dhaene, T., and Saeys, Y. (2015). FlowSOM: using self-organizing maps for visualization and interpretation of cytometry data. Cytometry A *87*, 636–645. https://doi.org/10.1002/cyto.a.22625.
42. Argüello, R.J., Combes, A.J., Char, R., Gigan, J.-P., Baaziz, A.I., Bousiquot, E., Camosseto, V., Samad, B., Tsui, J., Yan, P., et al. (2020). SCENITH: a flow cytometry-based method to functionally profile energy metabolism with single-cell resolution. Cell Metab. *32*, 1063–1075.e7. https://doi.org/10.1016/j.cmet.2020.11.007.
43. Fernández-García, J., Franco, F., Parik, S., Altea-Manzano, P., Pane, A.A., Broekaert, D., van Elsen, J., Di Conza, G., Vermeire, I., Schalley, T., et al. (2022). CD8+ T cell metabolic rewiring defined by scRNA-seq identifies a critical role of ASNS expression dynamics in T cell differentiation. Cell Rep. *41*, 111639. https://doi.org/10.1016/j.celrep.2022.111639.
44. Heuser, C., Renner, K., Kreutz, M., and Gattinoni, L. (2023). Targeting lactate metabolism for cancer immunotherapy-a matter of precision. In Seminars in Cancer Biology (Elsevier), pp. 32–45. https://doi.org/10.1016/j.semcancer.2022.12.001.
45. Hurwitz, R., Hozier, J., LeBien, T., Minowada, J., Gajl-Peczalska, K., Kubonishi, I., and Kersey, J. (1979). Characterization of a leukemic cell line of the pre-B phenotype. Int. J. Cancer *23*, 174–180. https://doi.org/10.1002/ijc.2910230206.
46. Uzana, R., Eisenberg, G., Sagi, Y., Frankenburg, S., Merims, S., Amariglio, N., Yefenof, E., Peretz, T., Machlenkin, A., and Lotem, M. (2012). Trogocytosis is a gateway to characterize functional diversity in melanoma-specific CD8+ T cell clones. J. Immunol. *188*, 632–640. https://doi.org/10.4049/jimmunol.1101429.
47. Rogers, R.S., and Bhattacharya, J. (2013). When cells become organelle donors. Physiology (Bethesda) *28*, 414–422. https://doi.org/10.1152/physiol.00032.2013.
48. Liu, Z., Sun, Y., Qi, Z., Cao, L., and Ding, S. (2022). Mitochondrial transfer/transplantation: an emerging therapeutic approach for multiple diseases. Cell Biosci. *12*, 66. https://doi.org/10.1186/s13578-022-00805-7.
49. Caicedo, A., Fritz, V., Brondello, J.-M., Ayala, M., Dennemont, I., Abdellaoui, N., de Fraipont, F., Moisan, A., Prouteau, C.A., Boukhaddaoui, H., et al. (2015). MitoCeption as a new tool to assess the effects of mesenchymal stem/stromal cell mitochondria on cancer cell metabolism and function. Sci. Rep. *5*, 9073. https://doi.org/10.1038/srep09073.
50. Nakano, T., Nakamura, Y., Park, J.-H., Tanaka, M., and Hayakawa, K. (2022). Mitochondrial surface coating with artificial lipid membrane improves the transfer efficacy. Commun. Biol. *5*, 745. https://doi.org/10.1038/s42003-022-03719-9.
51. Gäbelein, C.G., Feng, Q., Sarajlic, E., Zambelli, T., Guillaume-Gentil, O., Kornmann, B., and Vorholt, J.A. (2022). Mitochondria transplantation between living cells. PLoS Biol. *20*, e3001576. https://doi.org/10.1371/journal.pbio.3001576.

52. Buck, M.D., O'Sullivan, D., Klein Geltink, R.I., Curtis, J.D., Chang, C.H., Sanin, D.E., Qiu, J., Kretz, O., Braas, D., van der Windt, G.J.W., et al. (2016). Mitochondrial dynamics controls T cell fate through metabolic programming. Cell *166*, 63–76. https://doi.org/10.1016/j.cell.2016.05.035.

53. Nava Lauson, C.B., Tiberti, S., Corsetto, P.A., Conte, F., Tyagi, P., Machwirth, M., Ebert, S., Loffreda, A., Scheller, L., Sheta, D., et al. (2023). Linoleic acid potentiates CD8(+) T cell metabolic fitness and antitumor immunity. Cell Metab. *35*, 633–650.e9. https://doi.org/10.1016/j.cmet.2023.02.013.

54. Fraietta, J.A., Lacey, S.F., Orlando, E.J., Pruteanu-Malinici, I., Gohil, M., Lundh, S., Boesteanu, A.C., Wang, Y., O'Connor, R.S., Hwang, W.-T., et al. (2018). Determinants of response and resistance to CD19 chimeric antigen receptor (CAR) T cell therapy of chronic lymphocytic leukemia. Nat. Med. *24*, 563–571. https://doi.org/10.1038/s41591-018-0010-1.

55. Zhang, L., Zhang, W., Li, Z., Lin, S., Zheng, T., Hao, B., Hou, Y., Zhang, Y., Wang, K., Qin, C., et al. (2022). Mitochondria dysfunction in CD8+ T cells as an important contributing factor for cancer development and a potential target for cancer treatment: a review. J. Exp. Clin. Cancer Res. *41*, 227. https://doi.org/10.1186/s13046-022-02439-6.

56. Ozawa, T. (1995). Mechanism of somatic mitochondrial DNA mutations associated with age and diseases. Biochim. Biophys. Acta *1271*, 177–189. https://doi.org/10.1016/0925-4439(95)00026-z.

57. Yancik, R. (2005). Population aging and cancer: a cross-national concern. Cancer J. *11*, 437–441. https://doi.org/10.1097/00130404-200511000-00002.

58. Ron-Harel, N., Notarangelo, G., Ghergurovich, J.M., Paulo, J.A., Sage, P.T., Santos, D., Satterstrom, F.K., Gygi, S.P., Rabinowitz, J.D., Sharpe, A.H., et al. (2018). Defective respiration and one-carbon metabolism contribute to impaired naive T cell activation in aged mice. Proc. Natl. Acad. Sci. USA *115*, 13347–13352. https://doi.org/10.1073/pnas.1804149115.

59. Goronzy, J.J., and Weyand, C.M. (2017). Successful and maladaptive T cell aging. Immunity *46*, 364–378. https://doi.org/10.1016/j.immuni.2017.03.010.

60. Mozaffari, F., Lindemalm, C., Choudhury, A., Granstam-Björneklett, H., Helander, I., Lekander, M., Mikaelsson, E., Nilsson, B., Ojutkangas, M.L., Osterborg, A., et al. (2007). NK-cell and T-cell functions in patients with breast cancer: effects of surgery and adjuvant chemo- and radiotherapy. Br. J. Cancer *97*, 105–111. https://doi.org/10.1038/sj.bjc.6603840.

61. Wargo, J.A., Reuben, A., Cooper, Z.A., Oh, K.S., and Sullivan, R.J. (2015). Immune effects of chemotherapy, radiation, and targeted therapy and opportunities for combination with immunotherapy. Semin. Oncol. *42*, 601–616. https://doi.org/10.1053/j.seminoncol.2015.05.007.

62. Blackburn, S.D., Shin, H., Freeman, G.J., and Wherry, E.J. (2008). Selective expansion of a subset of exhausted CD8 T cells by αPD-L1 blockade. Proc. Natl. Acad. Sci. USA *105*, 15016–15021. https://doi.org/10.1073/pnas.0801497105.

63. Im, S.J., Hashimoto, M., Gerner, M.Y., Lee, J., Kissick, H.T., Burger, M.C., Shan, Q., Hale, J.S., Lee, J., Nasti, T.H., et al. (2016). Defining CD8+ T cells that provide the proliferative burst after PD-1 therapy. Nature *537*, 417–421. https://doi.org/10.1038/nature19330.

64. Court, A.C., Le-Gatt, A., Luz-Crawford, P., Parra, E., Aliaga-Tobar, V., Bátiz, L.F., Contreras, R.A., Ortúzar, M.I., Kurte, M., Elizondo-Vega, R., et al. (2020). Mitochondrial transfer from MSCs to T cells induces Treg differentiation and restricts inflammatory response. EMBO Rep. *21*, e48052. https://doi.org/10.15252/embr.201948052.

65. Good, Z., Spiegel, J.Y., Sahaf, B., Malipatlolla, M.B., Ehlinger, Z.J., Kurra, S., Desai, M.H., Reynolds, W.D., Wong Lin, A., Vandris, P., et al. (2022). Post-infusion CAR Treg cells identify patients resistant to CD19-CAR therapy. Nat. Med. *28*, 1860–1871. https://doi.org/10.1038/s41591-022-01960-7.

66. Haradhvala, N.J., Leick, M.B., Maurer, K., Gohil, S.H., Larson, R.C., Yao, N., Gallagher, K.M.E., Katsis, K., Frigault, M.J., Southard, J., et al. (2022). Distinct cellular dynamics associated with response to CAR-T therapy for refractory B cell lymphoma. Nat. Med. *28*, 1848–1859. https://doi.org/10.1038/s41591-022-01959-0.

67. Suomalainen, A., and Nunnari, J. (2024). Mitochondria at the crossroads of health and disease. Cell *187*, 2601–2627. https://doi.org/10.1016/j.cell.2024.04.037.

68. Nacarelli, T., Azar, A., Altinok, O., Orynbayeva, Z., and Sell, C. (2018). Rapamycin increases oxidative metabolism and enhances metabolic flexibility in human cardiac fibroblasts. GeroScience *40*, 243–256. https://doi.org/10.1007/s11357-018-0030-2.

69. Chiao, Y.A., Kolwicz, S.C., Basisty, N., Gagnidze, A., Zhang, J., Gu, H., Djukovic, D., Beyer, R.P., Raftery, D., MacCoss, M., et al. (2016). Rapamycin transiently induces mitochondrial remodeling to reprogram energy metabolism in old hearts. Aging (Albany, NY) *8*, 314–327. https://doi.org/10.18632/aging.100881.

70. Dumont, F.J., and Su, Q. (1996). Mechanism of action of the immunosuppressant rapamycin. Life Sci. *58*, 373–395. https://doi.org/10.1016/0024-3205(95)02233-3.

71. He, Y., de Castro, L.F., Shin, M.H., Dubois, W., Yang, H.H., Jiang, S., Mishra, P.J., Ren, L., Gou, H., Lal, A., et al. (2015). p53 loss increases the osteogenic differentiation of bone marrow stromal cells. Stem Cells *33*, 1304–1319. https://doi.org/10.1002/stem.1925.

72. Barrett, D.M., Seif, A.E., Carpenito, C., Teachey, D.T., Fish, J.D., June, C.H., Grupp, S.A., and Reid, G.S.D. (2011). Noninvasive bioluminescent imaging of primary patient acute lymphoblastic leukemia: a strategy for preclinical modeling. Blood *118*, e112–e117. https://doi.org/10.1182/blood-2011-04-346528.

73. Kochenderfer, J.N., Feldman, S.A., Zhao, Y., Xu, H., Black, M.A., Morgan, R.A., Wilson, W.H., and Rosenberg, S.A. (2009). Construction and preclinical evaluation of an anti-CD19 chimeric antigen receptor. J. Immunother. *32*, 689–702. https://doi.org/10.1097/CJI.0b013e3181ac6138.

74. Clement, K., Rees, H., Canver, M.C., Gehrke, J.M., Farouni, R., Hsu, J.Y., Cole, M.A., Liu, D.R., Joung, J.K., Bauer, D.E., et al. (2019). CRISPResso2 provides accurate and rapid genome editing sequence analysis. Nat. Biotechnol. *37*, 224–226. https://doi.org/10.1038/s41587-019-0032-3.

75. Aran, D., Looney, A.P., Liu, L., Wu, E., Fong, V., Hsu, A., Chak, S., Naikawadi, R.P., Wolters, P.J., Abate, A.R., et al. (2019). Reference-based analysis of lung single-cell sequencing reveals a transitional profibrotic macrophage. Nat. Immunol. *20*, 163–172. https://doi.org/10.1038/s41590-018-0276-y.

76. Borcherding, N., Vishwakarma, A., Voigt, A.P., Bellizzi, A., Kaplan, J., Nepple, K., Salem, A.K., Jenkins, R.W., Zakharia, Y., and Zhang, W. (2021). Mapping the immune environment in clear cell renal carcinoma by single-cell genomics. Commun. Biol. *4*, 122. https://doi.org/10.1038/s42003-020-01625-6.

STAR★METHODS

KEY RESOURCES TABLE

REAGENT or RESOURCE	SOURCE	IDENTIFIER
Antibodies		
anti-human CD8 (SK1) BV510	BD Pharmingen	Cat# 563919; RRID: AB_2722546
anti-mouse CD8 (53-6.7) Pacific Blue	BD Pharmingen	Cat# 558106; RRID:AB_397029
anti- mouse CD8 (53.6.7) Alexa-488	Biolegend	Cat# 100723; RRID:AB_389304
anti-human CD8 (SK1) Alexa-488	Biolegend	Cat# 344716; RRID:AB_10549301
anti-mouse Sca-1 (D7) Pacific Blue	Biolegend	Cat# 108120; RRID:AB_493273
anti-mouse CX3CR1 (SA011F11) BV605	Biolegend	Cat# 149027; RRID:AB_2565937
anti-mouse CD69 (H1.2F3) BV785	Biolegend	Cat# 104543; RRID:AB_2629640
anti-mouse CD3 (10030) PE/Cy5	Biolegend	Cat# 100310; RRID:AB_312675
anti-mouse KLRG1 (2F1/KLRG1) PE-Cy7	Biolegend	Cat# 138416; RRID:AB_2561736
anti-mouse CD27 (LG.3A10) APC	Biolegend	Cat# 124212; RRID:AB_2073425
anti-mouse CD44 (IM7) AF700	Biolegend	Cat# 103026; RRID:AB_493713
anti-mouse CD8a (53-6.7) APC-Cy7	Biolegend	Cat# 100714; RRID:AB_312753
anti-mouse CD366 (B8.2C12) PerCP/Cy5.5	Biolegend	Cat# 134012; RRID:AB_2632736
anti-mouse Granzyme B (GB11) Pacific Blue	Biolegend	Cat# 515408; RRID:AB_2562196
anti-mouse PD-1 (RMPI-30) PE-Cy7	Biolegend	Cat# 109110; RRID:AB_572017
anti-mouse LAG-3 (C9B7W) APC	Biolegend	Cat# 125210; RRID:AB_10639727
anti-mouse CD62L (MEL-14) BV650	BD Pharmingen	Cat# 564108; RRID:AB_2738597
anti-mouse IL7Rα (SB/199) BV711	BD Pharmingen	Cat# 565490; RRID:AB_2732059
anti-mouse CD45.2 (104) PerCP-Cy5.5	BD Pharmingen	Cat# 552950; RRID:AB_394528
anti-mouse CD45.2 (104) BUV737	BD Pharmingen	Cat# 564880; RRID:AB_2738998
anti-mouse CD244.2 (2B4) BV650	BD Pharmingen	Cat# 740467; RRID:AB_2740193
anti-mouse TIGIT (1G9) BV711	BD Pharmingen	Cat# 744214; RRID:AB_2742063
anti-mouse CD122 (TM-Beta) BUV737	BD Pharmingen	Cat# 741730; RRID:AB_2871100
anti-mouse CD45.1 (A20) FITC	eBiosciences	Cat# 11-0453-85; RRID:AB_465059
anti-mouse TCF1 (C6309) PE	Cell Signaling	Cat# 14456; RRID:AB_2798483
anti-mouse Ly5.1 (A20) APC	Biolegend	Cat# 110714; RRID:AB_313503
anti-humanTLN-2 (53.8)	BIO-RAD	Cat# MCA4771GA; RRID:AB_10698336
Anti-Puromycin clone (12D10) Alexa Fluor-647	Sigma Aldrich	Cat# MABE-343-AF647; RRID:AB_2736876
TotalSeq™-B 0301 anti-mouse Hashtag 1 Barcode Sequence- ACCCACCAGTAAGAC	Biolegend	Cat# 155831; RRID:AB_2814067
TotalSeq™-B 0302 anti-mouse Hashtag 2 Barcode Sequence- GGTCGAGAGCATTCA	Biolegend	Cat# 155833; RRID:AB_2814068
TotalSeq™-B 0303 anti-mouse Hashtag 3 Barcode Sequence- CTTGCCGCATGTCAT	Biolegend	Cat# 155835; RRID:AB_2814069
TotalSeq™-B 0304 anti-mouse Hashtag 4 Barcode Sequence - AAAGCATTCTTCACG	Biolegend	Cat# 155837; RRID:AB_2814070
TotalSeq™-B 0305 anti-mouse Hashtag 5 Barcode Sequence - CTTTGTCTTTGTGAG	Biolegend	Cat# 155839; RRID:AB_2814071
TotalSeq™-B 0306 anti-mouse Hashtag 6 Barcode Sequence - TATGCTGCCACGGTA	Biolegend	Cat# 155841; RRID:AB_2814072
TruStain FcX™ (anti-mouse CD16/32)	Biolegend	Cat# 101320; RRID:AB_1574975
Purified anti-mouse CD3e (145.2C11)	BD Pharmingen	Cat# 553057; RRID:AB_394590
Purified anti-mouse CD28 (37.51)	BD Pharmingen	Cat# 553294 RRID:AB_394763
Mre11 Antibody	Novus Biologicals	Cat# NB100-142; RRID:AB_10077796

(*Continued on next page*)

Continued

REAGENT or RESOURCE	SOURCE	IDENTIFIER
HRP-conjugated anti-Mouse IgG	Cell Signaling	Cat# 7076; RRID:AB_330924
Biological samples		
Human peripheral blood mononuclear cells from healthy donors	This paper.	N/A
Mouse Splenocytes	This paper.	N/A
MART-1 TILS	Michal Lotem, Hebrew University of Jerusalem	Uzana et al.[46]
Chemicals, peptides, and recombinant proteins		
Ethidium Bromide	Invitrogen	15585-011
Uridine powder, BioReagent, suitable for cell culture	Sigma	U3003
4% Paraformaldehyde (PFA)	ThermoFisher Scientific	J61899
Quick Extract	Lucigen	SS000035-D2
LIVE/DEAD™ Fixable Blue Dead Cell Stain	Thermo Fisher Scientific	L34962
LIVE/DEAD™ Fixable Far Red Dead Cell Stain	Thermo Fisher Scientific	L34974
Phalloidin AF-488	Thermo Fisher Scientific	A12379
Hoechst 33342	Thermo Fisher Scientific	H3570
Human recombinant IL15	NCI Frederick	50341
Human recombinant IL-2	Miltenyi	130-097-748
MitoTracker Deep Red	ThermoFisher Scientific	M22426
Cell-Tak	Corning	354240
Collagen Solution	Sigma-Aldrich	C3867-1VL
DMEM	Invitrogen	21969-035
RPMI	Invitrogen	61870-010
MEM-α, nucleosides	Invitrogen	22571-020
Penicillin-Streptomycin (10,000 U/mL)	Invitrogen	15140-122
Glutamax (100x)	Invitrogen	35050-038
Sodium Pyruvate 100mM	Invitrogen	11260-039
β-mercaptoethanol 50mM	Invitrogen	31350-010
MEM Non-Essential Amino Acids Solution (100X)	Invitrogen	11140-035
HEPES	Invitrogen	15630056
Fetal Bovine Serum, characterised	Hyclone	SH30071.03
Human AB Serum – Heat Inactivated	Valley Biomedical, Inc.	HP1022HI
Glutaraldehyde	Sigma	G5882-100ML
Sodium Cacodylate	Sigma	20840-100G-F
Osmium tetroxide (OsO4)	Electron Microscopy Sciences	19190
Phosphate Buffer Saline	Invitrogen	14190-094
Human gp100 (25-33 peptide)	Genescript	RP20344
Epoxyembedding kit	Sigma	45359
Uranyl acetate	ElectronMicroscopy Sciences	22400-4
Potassium ferrocyanide	Electron Microscopy Sciences	20150
PflFI Restriction Enzyme	New England Biolabs	R0595S
Pierce RIPA buffer	ThermoScientific	89900
L-778123	Cayman Chemicals	22940
Tissue-Tek O.C.T. compound	Sakura Finetek	4583
ibidi mounting medium	Ibidi GmbH	50001

(*Continued on next page*)

Continued

REAGENT or RESOURCE	SOURCE	IDENTIFIER
10x ACK lysis buffer	Elabscience	E-CK-A105
Ficoll® Paque Plus	Cytiva	17144003
IVISbrite D-Luciferin Potassium Salt Bioluminescent Substrate	PerkinElmer	122799
Rat Serum	Thermo Fisher Scientific	31888
DNase I	Roche	10104159001
Pierce™ 16 % Formaldehyd (w/v), methanolfrei	Thermo Fisher Scientific Inc.	28906
Glycine	Merck	J16407-36
Q5 high fidelity polymerase	New England Biolabs	M0492S
Oligomycin A	Sigma Aldrich	75351-5MG
Harringtonine	Santa Cruz Biotechnology	sc-204771
2-Deoxy-D-glucose:	Sigma Aldrich	D6134-5G
Puromycin dihydrochloride	Sigma-Aldrich	P7255-25mg
Critical commercial assays		
Seahorse XFe96 FluxPak mini	Agilent	102601-100
Seahorse XF T Cell Metabolic Profiling Kit	Agilent	103772-100
Seahorse XF 1.0 M glucose solution	Agilent	103577-100
Seahorse XF 100 mM pyruvate solution	Agilent	103578-100
Seahorse XF 200 mM glutamine solution	Agilent	103579-100
Seahorse XF DMEM medium, pH 7.4, 500 mL	Agilent	103575-100
Lonza™ P3 Primary Cell 4D-Nucleofector™ X Kit S	Lonza	V4XP-3032
Lonza™ P1 Primary Cell 4D-Nucleofector™ X Kit S	Lonza	V4XP-1032
TrueCut™ Cas9 Protein v2	ThermoFischer	A36499
Alt-R® CRISPR-Cas9 tracrRNA	IDT	1072534
Mouse Total CD8+ T cell isolation kit	Stem Cell Technologies	19853
Human Naïve CD8+ T cell isolation kit	Stem Cell Technologies	17968
Mycoplasma PCR test	PromoCell	PK-CA91-1096
4–20% Criterion™ TGX™ Precast Midi Protein Gel	BioRad	5671094
Trans-Blot Turbo Midi 0.2 μm PVDF Transfer membrane	BioRad	1704157
Pierce™ ECL Western Blotting Substrate	BioRad	32209
eBioscience™ Foxp3 / Transcription Factor Staining Buffer Set	Invitrogen	00-5523-00
BD Cytofix/Cytoperm™ Fixation/Permeabilization Kit	BD Biosciences	554714
RNA extraction RNeasy Plus Mini Kit	QIAGEN	74134
High-Capacity cDNA Reverse Transcription Kit	Applied Biosystems	4368814
PowerUp™ SYBR™ Green Master Mix for qPCR	ThermoFisher Scientific	A25741
NEB Next Ultra II kit	New England Biolabs	E7645L
P2 mid output kit	Illumina	20046811
3' Feature Barcode Kit, 16 rxns	10x Genomics, Inc.	1000262
Chromium Next GEM Single Cell 3' Kit v3.1, 4 rxns	10x Genomics, Inc.	1000269

(*Continued on next page*)

Continued

REAGENT or RESOURCE	SOURCE	IDENTIFIER
Chromium Next GEM Chip G Single Cell Kit, 16 rxns	10x Genomics, Inc.	PN-1000127
NextSeq 2000 P3 100 Cycle	Illumina, Inc.	20040559
Mitochondria Isolation Kit	ThermoFisher Scientific	89874
Deposited data		
Human Mitohcondrial Transfer Bulk RNA-seq data files	This manuscript, deposited in EGA	EGA: EGAS00001007356 and EGAD00001011082
Mouse Mitohcondrial Transfer Bulk RNA-seq data files	This manuscript, deposited in GEO	GEO: GSE229487
Mouse Mitochondrial Transfer Single cell RNA-seq data files	This manuscript, deposited in	GEO: GSE254191
Experimental models: Cell lines		
DM5, immortalized mBMSC cell line	Pamela G. Robey, National Institutes of Health	He et al.[71]
Immortalized bone marrow-derived human MSC cells	Genecopoeia	SL428
Platinum-E cells	Cell Biolabs	RV-101
293GP cells	Ling Zhang, Experimental Transplantation and Immunology Branch (NCI), USA	N/A
NALM6	DSMZ	ACC 128
B16 melanoma hgp100	Ken-Ichi Handa, Surgery Branch of the National Cancer institute (NCI), USA	Hanada et al.[38]
PG13 CD19 CAR	James N. Kochenderfer, Surgery Branch of the National Cancer institute (NCI), USA	Kochenderfer et al.[73]
SK23-GFP	This study	N/A
Experimental models: Organisms/strains		
C57Bl/6 wild-type mice, (Female in vivo studies and Male/Female in vitro studies)	Charles River Laboratories	Strain Code 027
Balb/c, (Female)	Charles River Laboratories	Strain Code: 028
Pmel-1 Ly5.1 mice [B6.Cg-ThylalCy Tg(TcraTcrb)SResVJ; 86.SJL-Ptprca Pepcb/BoyJ] Jax-ID 005023 crossed with Jax-ID 002014. (Female in vivo studies and Male/Female in vitro studies)	National Institutes of Health/ Universitätsklinikum Regensburg core breeding facility	N/A
NCG mice [NOD-Prkdcem26Cd52Il2rgem 26Cd22/NjuCrl], (Female)	Charles River Laboratories	Strain code: 572NCG
NXG MICE [NOD-Prkdcscid-IL2rgTm1/Rj], (Female)	Janvier Labs	Strain code: NXG
Oligonucleotides		
Mouse_Mt-CO2-F (GAGCAGTCCCCTCCCTAGGA)	IDT	N/A
Mouse_Mt-CO2-R (GGTTTGATGTTACTGT TGCTTGATTT)	IDT	N/A
Mouse_App-F (CGGAAACGACGCTCTCATG)	IDT	N/A

(*Continued on next page*)

Continued

REAGENT or RESOURCE	SOURCE	IDENTIFIER
Mouse_App-R (CCAGGCTGAATTCCCCAT)	IDT	N/A
Human_MT-CO2-F (CGTCTGAACTATCC TGCCCG)	IDT	N/A
Human_MT-CO2-R (TGGTAAGGGAGGGATCGTTG)	IDT	N/A
Human_APP-F (TTTTTGTG TGCTCTCCCAGGTCT)	IDT	N/A
Human_APP-R (TGGTCACTG GTTGGTTGGC).	IDT	N/A
Human_Talin2_F (CAAGGAAGTCGCCAACAGCACT)	IDT	N/A
Human_Talin2_R (TTGAGGCGAACGCTGTCAGGTT)	IDT	N/A
Human_ACTB_F (CATGTACGTTGCTATCCAGGC)	IDT	N/A
Human_ACTB_R (CTCCTTAATGTCACGCACGAT)	IDT	N/A
SNP_A9348G-F(CGAAACCACA TAAATCAAGCCC)	IDT	N/A
SNP_A9348G-R(CTCTCTTCTGG GTTTATTCAGA)	IDT	N/A
Predesigned crRNA TLN2-(AA)	IDT	Hs.Cas9.TLN2.1.AA
Predesigned crRNA TLN2-(AB)	IDT	Hs.Cas9.TLN2.1.AB
Predesigned crRNA CD3-(AA)	IDT	Hs.Cas9.CD2.1.AA
Predesigned crRNA CD3-(AD)	IDT	Hs.Cas9.CD2.1.AD
Predesigned crRNA CD3-(AE)	IDT	Hs.Cas9.CD2.1.AE
pMito-dsRed Vector	Takara Bio Inc.	632421
TLN2 AA_F (ctttccctacacgac gctcttccgatctGGATCACAGC CGAACATTCAGAG)	Microsynth	Custom oligo
TLN2 AA_R (ggagttcagacgtgt gctcttccgatctGCAATCTCACC AACCTCAGTGTC)	Microsynth	Custom oligo
TLN2 AB_F (ctttccctacacg acgctcttccgatctGGGC CTGGAAGTCAGTGATG)	Microsynth	Custom oligo
TLN2 AB_R (ggagttcagacgt gtgctcttccgatctACTGG GATTGGCAGCATACC)	Microsynth	Custom oligo
TLN2 AC_F (ctttccctacacgac gctcttccgatctAGAGGGT GTACTGGGCCATG)	Microsynth	Custom oligo
TLN2 AC_R (ggagttcagacgtgt gctcttccgatctGGCTTGA AATCCACCAAACTCAC)	Microsynth	Custom oligo
TNL2 AC OT1_F (ctttccctacac gacgctcttccgatctCACAGTGT GCGTGTCCTTGC)	Microsynth	Custom oligo
TNL2 AC OT1_R (ggagttcagacg tgtgctcttccgatctGGAAGCC AGCAAACTCACAGG)	Microsynth	Custom oligo

(*Continued on next page*)

Continued

REAGENT or RESOURCE	SOURCE	IDENTIFIER
Software and Algorithms		
FlowJo software 10.8.2	Tree Star	https://www.flowjo.com/
Image J	NIH	https://imagej.nih.gov/ij/index.html
Zen lite Software	ZEISS	https://www.zeiss.com/microscopy/en/products/software/zeiss-zen-lite.html
Incucyte Software (v2020C)	Sartorius	https://www.sartorius.com/en/products/live-cell-imaging-analysis/live-cell-analysis-software
Leica LAS X	Leica	N/A
Prism software v9.4	GraphPad Software	https://www.graphpad.com/scientific-software/prism/
Bowtie2 version 2.4.4	GitHub, Inc.	N/A
Blender2	GitHub, Inc.	https://github.com/cornlab/blender/blob/master/blender2.py
hg38	GitHub, Inc.	https://github.com/staciawyman/blender/blob/master/hg38.blacklist.bed
CRISPResso2	GitHub, Inc.	https://github.com/pinellolab/CRISPResso2
Illumina Dragon (v-3.8.4, NextSeq 2000)	Illumina, Inc.	https://support.illumina.com/sequencing/sequencing_software/dragen-bio-it-platform.html
Cellranger 7.0.0	10x Genomics	https://www.10xgenomics.com/support/software/cell-ranger/latest/release-notes/cr-release-notes
R (version 4.1.1)	R Core Team	https://cran.r-project.org/
Seurat package (version 4.3.0)	N/A	https://github.com/satijalab/seurat/tree/41d19a8a55350bff444340d6ae7d7e03417d4173 Cran:tar.gz: https://cran.r-project.org/src/contrib/Archive/Seurat/Seurat_4.3.0.tar.gz
scDblFinder R-package2 (version 1.8.0)	N/A	https://doi.org/10.18129/B9.bioc.scDblFinder
SingleCellExperiment (version 1.16.0)	N/A	https://doi.org/10.18129/B9.bioc.SingleCellExperiment
singleR (version 1.8.1)	N/A	https://doi.org/10.18129/B9.bioc.SingleR
enrichplot (version 1.23.0.991)	N/A	https://doi.org/10.18129/B9.bioc.enrichplot
clusterProfiler R-package (version 4.2.0)	N/A	https://doi.org/10.18129/B9.bioc.clusterProfiler
gprofiler2 R-package (version 0.2.2)	N/A	https://cran.r-project.org/web/packages/gprofiler2/index.html
ggplot2 R-package (version 3.3.5)	N/A	https://cran.r-project.org/web/packages/ggplot2/index.html Cran:tar.gz: https://cran.r-project.org/src/contrib/Archive/ggplot2/ggplot2_3.3.6.tar.gz
ggdendro R-package(0.1.23)	N/A	https://cran.r-project.org/web/packages/ggdendro/index.html
limma(v3.50.0)	Bioconductor	https://doi.org/10.18129/B9.bioc.limma
Biorender	BioRender	https://biorender.com/
Other		
25mm with 0.4μm pore size polycarbonate membrane insert	Corning	3412
75mm with 0.4μm pore size polycarbonate membrane insert	Corning	7910
BioCoat Collagen I 100 mm TC-treated Culture Dishes	Corning	354450
CellStar 6-Well Cell Culture Multiwell Plates	Fischer Scientific	657160

(*Continued on next page*)

Continued

REAGENT or RESOURCE	SOURCE	IDENTIFIER
96 well plate Round Bottom Ultra-Low Attachment Microplate,	Corning	7007
8-Well μ-Slide	ibidi Gmbh	80826
12 mm diameter glass coverslips	VWR	89015-725
Mattek gridded dishes	MatTek Corp	P35G-1.5-14-C-GRD
gentleMACS C Tubes	Miltentyi	130096334
Ultracomp eBeads™ Plus	Invitrogen	01-3333-42
CountBright™ Plus Absolute Counting Beads	Invitrogen	C36950
Dynabeads™ Human T-Activator CD3/CD28 for T Cell Expansion and Activation	Invitrogen	11131D

EXPERIMENTAL MODEL AND SUBJECT DETAILS

Cell lines

Immortalized human BMSCs (GeneCopoeia) and DM5, a spontaneously immortalized mouse BMSC line[71] were transduced to express the fluorescent protein dsRed fused with cytochrome c oxidase subunit 8A (COX8A) (Mito-dsRed). dsRed2-Mito (632421, Takara Bio Inc) was cloned into a MSGV1 γ-retroviral vector and produced in Platinum-E cells (Cell Biolabs) or 293GP cells (ATCC) for transduction. Mouse $CD8^+$ T cells were isolated from either C57BL/6, pmel-1 Ly5.1, or BALB/c mice using a Total $CD8^+$ T cell isolation kit (Stem Cell Technologies). Human $CD8^+$ T cells were isolated from peripheral blood mononuclear cell buffy coats or leukocyte reduction system chambers of healthy donors (NIH, US and University Hospital Regensburg, Germany) using a Naïve $CD8^+$ T cell isolation kit (Stem Cell Technologies). NALM6 cell line was originally obtained from DSMZ (ACC 128) and transduced with Luciferase-GFP (GL) as previously described.[72] PG13 expressing CD19-CAR (FMC63-28-ζ) retrovirus was used for transduction of human $CD8^+$ T cells with CD19 CAR as previously described.[73] $B16_{KVP}$ melanoma expressing human gp100 was engineered as previously described.[38] NALM6-GL and both human and mouse $CD8^+$ T cells were cultured with RPMI complete medium; human BMSCs, PG13 CD19-CAR, $B16_{KVP}$, Platinum-E, SK23-GFP, and 293GP cells were cultured with DMEM complete medium; and DM5 cell line was cultured with MEM-α complete medium. MART-1 TILs were kindly provided by Prof. Lotem and cultured in RPMI supplemented with 10% heat inactivated human AB serum (Valley Biomedical Inc.), 1% Pen/strep (Gibco), 1% HEPES (Gibco) and 0.01% β-mercaptoethanol (Gibco). All cell lines were regularly tested and validated as being mycoplasma free via a PCR-based assay (PromoCell).

Experimental Animals

C57BL/6 and BALB/c mice ages 6–8 weeks were obtained from Charles River. Immunodeficient NCG and NXG mice ages 6–8 weeks were obtained from Charles River and Janvier Labs, respectively. Pmel-1-Ly5.1 were generated in house breeding at either at animal facilities at the US National Institutes of Health or University Hospital Regensburg. All mice were housed in a specific pathogen-free facility under standard conditions (12 hr light/dark, food and water ad libitum). All mouse experiments were performed in strict accordance with the relevant guidelines and regulations of the University of Regensburg and US National Cancer Institute. All protocols were approved by relevant Animal Care and Use Committee at the US National Institutes of Health and the German authorities.

METHOD DETAILS

Antibodies, flow cytometry, and cell sorting

For cell sorting, we used antibodies anti-human CD8 (SK1) and anti-mouse CD8 (53–6.7) from BD Biosciences together with LIVE/DEAD™ Fixable Far Red Dead Cell Stain (Invitrogen™) unless otherwise stated. For flow cytometry analyses we employed the following antibodies. Anti-Sca-1 (D7), anti-CX3CR1 (SA011F11), anti-CD69 (H1.2F3) anti-CD3 (145-2C11), anti-KLRG1 (2F1/KLRG1), anti-CD27 (LG.3A10), anti-CD44 (IM7), anti-CD8a (53-6.7), anti-CD366 (B8.2C12), anti-Granzyme B (GB11), anti-PD-1 (RMPI-30) and anti-LAG-3 (C9B7W) were from Biolegend; anti-CD62L (MEL-14), anti-IL7Rα (SB/199), anti-CD45.2 (104), anti-CD244.2 (2B4), anti-TIGIT (1G9) were from BD Pharmingen; anti-CD122 (TM-Beta) was from BD Biosciences; anti-CD45.1 (A20) was from eBiosciences; and anti-TCF1 (C6309) was from Cell Signaling Technology. TruStain FcX™ used for blocking non-specific binding of immunoglobulin was from Biolegend and LIVE/DEAD™ Fixable Blue Dead Cell Stain was from Thermo Fisher Scientific. Ultracomp eBeads™ Plus (Invitrogen™) were used for compensation. LSR II or BDFortessa and BD FACSymphony (BD Biosciences)

were used for flow cytometry acquisition and a FACSAria Fusion (BD Biosciences) or BD Influx (BD Biosciences) were employed for cell sorting. Samples were analyzed with FlowJo software 10.8.2 (BD Biosciences).

Scanning electron microscopy of nanotubes

Human or mouse BMSCs and $CD8^+$ T cells were co-cultured on 12 mm diameter glass coverslips (VWR) for 24 hrs according to the experimental outline. The sample was fixed by 2.5% glutaraldehyde (Sigma-Aldrich) in 0.1 M sodium cacodylate buffer (Electron Microscopy Sciences). Cells were then washed 3 × 15 min with 0.1 M sodium cacodylate buffer, post-fixed in 0.1% Osmium tetroxide (OsO_4) (Sigma-Aldrich) in water for 1 hr at room temperature (RT) and washed 2 × 10 min with water before dehydration. The dehydration step was performed as follows: 35% ethanol for 5 min, 50% ethanol for 5 min, 70% ethanol for 10 min, 90% ethanol for 10 min, and 2 × 100% ethanol for 10 min. Following fixation and dehydration, the coverslips were dried and placed on FESEM stubs for sputter coating by EMS 300T D Dual Head Sputter Coater with Au or Pt/Pd (5 nm). Images were acquired on a Zeiss Ultra55 microscope equipped with a Gemini column and SE2 detector. Images were processed in ImageJ software.

Fluorescence microscopy of BMSC-$CD8^+$ T cell cocultures

Human or mouse BMSCs Mito-dsRed cell lines were co-cultured with $CD8^+$ T cells from health donors or TILs (MART-1) on 12 mm diameter glass coverslips (VWR) or 8-well μ-Slide (ibidi Gmbh). After 24 hrs, cells were fixed with 4% paraformaldehyde (PFA) at room temperature for 2 hr. The fixed co-cultured cells were washed three times with 1× PBS for 20 min. For structural assessment of nanotubes, cells on coverslips were stained for 1 hr with 50 μg/ml of Phalloidin AF-488 (Thermo Fisher Scientific) at RT followed by nuclear staining with Hoechst 33342 (Thermo Fisher Scientific) for 15-20 min. The cells were washed with 1× PBS-T three more times. The coverslips were mounted on glass slides and images were taken on a Nikon Eclipse Ti camera (Nikon Instruments) with NIS Elements Imaging Software (3.10) or TissueFAXS Plus slide scanner (TissueGnostics USA) equipped with Hamamatsu Orca Flash 4.0 V2 cooled digital CMOS camera. Confocal fluorescence microscopy was done on Zeiss LSM 800, Airyscan Confocal Laser Scanner Microscope with Zen 2.3 software. Post-processing of the images was done either in ImageJ or Zen lite software. For functional assessment of transferred mitochondria, cells were pre-stained with MitoTracker Deep Red as per manufacturer's guidelines prior to co-culture in 8-well μ-Slide and stained with CD8-VioBlue (MiltenyiBiotec) post-fixation for 30 minutes at 4°C. BMSC and TIL co-cultures were imaged using Stellaris 8 (Leica Microsystems).

Murine co-culture system platform

For murine samples, transwells with 25 mm or 75 mm diameter with 0.4 μm pore size polycarbonate membrane insert (Corning) were used for *in vitro* co-culture of BMSCs and $CD8^+$ T cells. In brief, mouse $CD8^+$ T cells were isolated from either C57BL/6, pmel-1 Ly5.1, or BALB/c mice using either Total $CD8^+$ T cell isolation kit (Stem Cell Technologies) and activated in non-tissue culture-treated 24-well plates (Corning) using either anti-mouse CD3e (145.2C11)/CD28 (37.51) both from BD Pharmingen, or for pmel-1 cells only whole splenocytes were isolated and activated using 1μM human $gp100_{25\text{-}33}$ peptide (Genescript), in RPMI complete media supplemented with rhIL-2 (Proleukin) for 3 days. On the day of co-culture, the inserts of the transwells were seeded with either 1.5×10^5 (for 24mm) or 1.5×10^6 (for 75mm) Mito-dsRed labeled mouse DM5 BMSCs in complete MEM-α media. After allowing BMSCs to attach for at least 5 hrs, media in the insert was removed, and pre-activated mouse $CD8^+$ T cells were seeded at a ratio of 1:1 or 3:1 in RPMI complete media. After 24-36 hrs, cells were collected for further analysis.

Incubation of T cells with isolated mitochondria

Isolation of the mitochondria from Mito-dsRed DM5-BMSC (Exo-Mito) was performed using Mitochondria Isolation Kit (ThermoFisher) following manufacturer protocol. The isolated mitochondria was resuspended in Mitochondria culture buffer composition: 70 mM sucrose, 220 mM mannitol, 10 mM KH2P04, 5 mM MgCl2, 2 mM HEPES, 1 mM EGTA,0.2% (w/v) fatty acid-free BSA, and 5 mM BME pH 7.0. The isolated mitochondria was used (added to T cells) within 2 hrs of isolation. Mito suspension was incubated with the T cells for 30 hrs and transfer was assessed by flow cytometry.

Human co-culture system platform

For human samples, tissue culture-treated 6-well plate (Corning) coated with collagen solution (Sigma-Aldrich) or pre-coated BioCoat™ 10 mm Petri dishes (Corning) were used for in vitro co-culture of BMSCs and $CD8^+$ T cells. In brief, $CD8^+$ T cells were isolated from buffy coats from healthy donors using a Naive $CD8^+$ T cell isolation kit (Stem Cell Technologies) and activated using a 3:1 ratio (beads:cells) of CD3/28 Dynabeads beads (Invitrogen™) in RPMI complete media supplemented with 60 IU/ml of rIL-2 (Proleukin) for 2 days and 3 days further expansion. On the day of co-culture, the tissue culture plates were seeded with either 1.5×10^5 (for 6-well plate) or 1.5×10^6 (for 10mm petri dish) Mito-dsRed labeled human BMSCs in complete DMEM media. After allowing BMSCs to attach for at least 5 hrs, media was removed, and pre-activated human $CD8^+$ T cells were seeded at a ratio of 1:1 or 3:1 in RPMI complete media. After 24–36 hrs cells were collected for further analysis.

Confocal imaging of sorted cells

Sorted human and mouse $Mito^+$ and $Mito^-$ cells (1×10^5) were stained in 10 nM MitoTracker Deep Red (ThermoFisher Scientific) in PBS for 15 minutes at 37°C. After incubation, cells were washed with complete RPMI media to remove excess dye, and then

counterstained with either Alexa-488 conjugated anti-mouse CD8 (53.6.7, Biolegend) or Alexa-488 conjugated anti-human CD8 (SK1, Biolegend) in conjunction with Hoechst 33342 (Invitrogen™, 2 μg/ml dilution) for 20 mins at 4°C. Stained cells were then seeded into 8-well μ-Slide (ibidi Gmbh) coated with Cell-Tak™ (Corning) and visualized using either Stellaris 8 (Leica Microsystems) or SoRa (Nikon) confocal microscope.

Quantification of mtDNA content

mtDNA was quantified with real-time PCR. Total DNA was isolated from BMSCs using Quick Extract™ DNA Extraction Solution (Lucigen), according to the manufacturer's protocol. Real-time PCR was performed in triplicates on 96-well plates (Applied Biosystems). Each PCR reaction (final volume 25 μl) contained 25 ng DNA, 12.5 μl of PowerUp™ SYBR™ Green PCR Master Mix (Applied Biosystems) and 0.5 μM of each forward and reverse primer. MtDNA was quantified using primers specific for the mouse or human *MT-CO2* gene and normalized using primers specific for the murine or human reference gene *APP*. Primers were as follows; mouse mt-Co2-F(GAGCAGTCCCCTCCCTAGGA), mouse mt-Co2-R (GGTTTGATGTTACTGT TGCTTGATTT), mouse App-F (CGGAAA CGACGCTCTCA TG), mouse App-R (CCAGGCTGAATTCCCCAT), human MT-CO2-F (CGTCTGAACTATCC TGCCCG), human MT-CO2-R (TGGTAAGGGAGGGATCGTTG), human APP-F (TTTTTGTG TGCTCTCCCAGGTCT), and human APP-R (TGGTCACT GGTTGGTTGGC).

Generation of BMSC lines with partially dysfunctional donor mitochondria

To obtain BMSC with dysfunctional donor mitochondria, mito-dsRed labelled BMSCs were cultured in the presence of 50 ng/ml EtBr (human cells) or 200 ng/ml EtBr (mouse cells) for 14 days. EtBr was added to the respective culture medium together with 50 μg/ml uridine. Mitochondria function was checked using qPCR, MitoTracker DeepRed stain, and Seahorse MST assay. RHOT1 (Miro1) expression of EtBr treated and untreated BMSC line was assessed by immunoblot. In brief, cells were lysed with radioimmunoprecipitation assay (RIPA) lysis buffer and equal amounts of protein lysates were electrophoresed on a 10–15% polyacrylamide gel for 1 hr and transferred to nitrocellulose membrane through wet blotting for 2 hrs at 350 mA (Bio-Rad Laboratories). Membranes were blocked by 5% BSA in 1X TBS-T (1X TBS and 0.1% Tween 20) for 1 hr and incubated with primary antibodies with either RHOT1 (Sigma; 1:500), and GAPDH (SCBT; 1:2,000) at 4 °C for 12–14 h. After washing three times with 1X TBS-T, the membrane was incubated with the secondary HRP-goat-anti-mouse/rabbit antibody (1:3,000) (Bio-Rad Laboratories) for 1 hr at room temperature. The membranes were washed twice with 1X TBS-T and once with TBS before developed using chemiluminescent Femto Substrate (Thermo Scientific) and imaged using G:BOX bio-imaging system (Syngene) using Quantity One software for image analysis.

Correlative light-electron microscopy

Sorted cells were fixed with 4% PFA and immobilized on Mattek gridded dishes (P35G-1.5-14-C-GRD, MatTek CorpAshland) using Cell Tak™ (Corning) and stained with Hoechst (1 μg/ml, Molecular Probes) for 20 min in PBS. Samples were acquired using an Olympus FluoVIEW FV3000RS confocal microscope with a UPLSAPO 60XS (NA 1.3) Silicone objective. After acquisition of the fluorescence images and the grid reference coordinates, cells were fixed with 2.5% glutaraldehyde in 0.1 M cacodylate buffer pH 7.4 for 1 hr at room temperature. Samples were then postfixed in 1% osmium tetroxide, 1.5% potassium ferrocyanide in 0.1 M cacodylate buffer for 1 hr on ice and en-bloc stained in 0.5% uranyl acetate overnight at 4°C. Samples were dehydrated in increasing concentrations of ethanol and infiltrated in epoxy resin (Sigma-Aldrich). After curing at 60°C for 48 hrs embedded cells were removed from the glass coverslips by dipping in liquid nitrogen. Ultrathin sections were obtained using an ultramicrotome (UC7, Leica microsystem), collected on formvar carbon coated slot copper grids, stained with uranyl acetate and Sato's lead solutions and observed in a Transmission Electron Microscope Talos L120C (FEI, Thermo Fisher Scientific) operating at 120 keV. Images were acquired with a Ceta CCD camera (FEI, Thermo Fisher Scientific). TEM images were then aligned to fluorescence images using the ICY ec-CLEM plugin.

Restriction enzyme analysis of mtDNA

Total DNA was isolated from sorted Mito$^+$ and Mito$^-$ cells following co-culture of CD8$^+$ T cells from BALB/c mice with Mito-dsRed labeled mouse DM5 BMSCs using QuickExtract™DNA Extaction Solution (Lucigen). Total DNA was also isolated from Mito-dsRed labelled mouse DM5 BMSCs and BALB/c CD8$^+$ T cells as a control. A 385 bp fragment (9072- 9456) of mitochondrial *mt-Co3* gene containing the A9348G polymorphism site was amplified from the samples by PCR using a thermocycler (BioRad) with the following primers: mt-Co3-F, (CGAAACCACATAAATCAAGCCC) and mt-Co3-R (CTCTCTTCTGGGTTTATTCAGA). The PCR product was then digested with PflFI (New England Biolabs) that recognizes the *Asp*I restriction site for 15 mins at 37 °C and the fragments were visualized by electrophoresis in a 2% agarose gel containing 0.5 μg/ml EtBr.

Mitochondria Stress Test assay

A Seahorse XFe96 Analyzer (Agilent) was used to determine OCR for sorted Mito$^+$ and Mito$^-$ CD8$^+$ T cells. Sorted cells were washed in assay media [XF Base media (Agilent) with glucose (10 mM), sodium pyruvate (1 mM) and L-glutamine (2 mM) (Gibco), pH 7.4] at 37 °C before being plated onto Seahorse cell culture plates coated with Cell-Tak™ (Corning) at 2.5×10^5 cells per well. After cell adherence and equilibration, OCR (pmol/min) was measured at steady state and after sequential injection of oligomycin (1.5 μM), BAM15 (2.5 μM), rotenone (1 μM), and antimycin A (1 μM) (Sigma-Aldrich). Experiments with the Seahorse system utilized the

following assay conditions: 2 min mixture, 2 min wait, and 3 min measurement. SRC was calculated as oxygen consumption rate (OCR) at maximum rate (OCR_{Max}) − OCR in basal state (OCR_{Bas}).

Bulk RNA-sequencing

For human samples, total cellular RNA was isolated from Mito$^+$ and Mito$^-$ CD8$^+$ cells using the RNeasy Mini Kit (Qiagen). The concentration and quality of the purified RNA was analyzed using the RNA ScreenTape Kit (Agilent). Generation of dsDNA libraries for Illumina sequencing from total cellular RNA was carried out using the SMART-Seq Stranded Kit from Takara according to the manufacturer's instructions. The quality of dsDNA libraries was analyzed using the High Sensitivity D1000 ScreenTape Kit (Agilent) and concentrations were assessed with the Qubit dsDNA HS Kit (Thermo Fisher Scientific). Equimolar amounts of each human library were pooled and sequenced on a NextSeq 550 instrument controlled by the NextSeq Control Software (NCS) v2.2.0, using a 75 Cycles High Output Kit with a single index, and single-end (SE) run parameters. Image analysis and base calling were done by the Real Time Analysis Software (RTA, v2.4.11) at the NGS-Core Facility (LIT). For mouse samples, total cellular RNA was isolated from post-sorted Mito$^+$ and Mito$^-$ CD8+ cells using the RNeasy Plus Mini Kit (Qiagen) as per manufacturers recommended protocol. The quantity and quality of purified RNA was analyzed with the Ribogreen Assay (ThermoFisher Scientific) and HS RNA Fragment Analyzer chip (Agilent), respectively. Generation of libraries for Illumina sequencing was completed on these samples using KAPA HyperPrep kit (KAPA Biosystems). The quality and quantity of dsDNA libraries was analyzed using the DNA-5k Caliper (PerkinElmer) and Qubit dsDNA HS Kit (Thermo Fisher Scientific). Sequencing was carried out on the NovaSeq 6000 sequencer S4. RNA-seq data for the human and mouse samples are listed in Tables S1 and S2.

Bioinformatic analysis of bulk RNA-sequencing data

For data analysis of RNA sequencing data, the output data from the NextSeq550, ".bcl" files, were converted into ".fastq" files with the bcl2fastq software (v2.20.0.422). For the human and mouse RNA Seq data, QC analysis and read mapping was performed using the SnakePipes analysis pipeline (v2.5.1). The pipeline used, among others, the following software: samtools (v1.9), STAR (2.7.4a), featureCounts (v2.0.0). Genome: GRCh38_gencode_release29 (ftp://ftp.ebi.ac.uk/pub/databases/ gencode/Gencode_human/release_29/ and GRCh38.primary_assembly.genome.fa.gz). Mouse Genome GRCm38.primary_assembly (ftp://ftp.ebi.ac.uk/pub/databases/gencode/Gencode_mouse/release_M23/GRCm38.primary_assembly.genome.fa.gz). QC of the count matrix and DE-Gene calling was performed with DESeq2. Gene counts were prefiltered with edgeR:filterByExpr and the FDR was set to (Padj.hs<0.05) for the human data set. Volcano plots were produced with the enhancedVolcano and ggrepel package (Figure 3A). For analysis of co-regulated and orthologous genes, DESeq result tables were merged using orthologous annotation derived from ENSEMBL using the biomaRt package. Only orthologous genes were taken forward. Subsequently, positively and negatively co-regulated genes were selected. The resulting gene table was selected for genes showing a baseMean.hs expression of 100 counts and Padj.hs <0.05. For the heatmap (Figure 3B), data was subset for human data to comply with baseMean.hs >100 and Padj.hs <0.05 and mouse data to show a p-value below 0.15. Variance stabilizing transformed (vst-function) expression data (DESeq2) was Z-score transformed for the mouse and human dataset separately. For hierachical clustering (euclidean distance, method complete), both data sets were combined and plotted with pheatmap. Over-representation analysis of up/down regulated co-regulated genes was performed using EnrichR with genes complying with: human: baseMean.hs >100 and Padj.hs<0.05 (59 genes).

CRISPR-Cas9 *TLN2* knockout

To knockout *TLN2* or *CD2* control genes in both human CD8$^+$ T cells and Mito-dsRed BMSCs we used Lonza™ P3 Primary Cell 4D-Nucleofector™ X Kit S (Lonza™ V4XP-3032) and Lonza™ P1 Primary Cell 4D-Nucleofector™ X Kit S (Lonza™ V4XP-1032), respectively, with TrueCut™ Cas9 Protein v2 (ThermoFischer), Alt-R® CRISPR-Cas9 tracrRNA (IDT) and the predesigned crRNA TLN2-(AA & AB) and CD2-(AA, AD&AE) (IDT). In brief, tracrRNA (200 μM) and crRNA (200 μM) were mixed equimolar proportions (0.75 μl each with 1.5 μl IDTE Buffer, per guide reaction), incubated 5 mins at 95°C in a ProFlex PCR System (Applied Biosystems™) and allowed to cool to RT for 20 mins. Newly formed gRNA was then combined with Cas9 enzyme (3 μl of gRNA and 1.2 μl of TrueCut Cas9 for each guide, topped up to 12.6 μl with IDTE Buffer) and incubated at RT for 20 mins to create TLN2 and CD2 RNP complexes. CD8$^+$ T cells (1×10^6, pre-activated for 24 hrs) and Mito-dsRed (5×10^5, low confluence) were seeded in 20 μl of P3 and P1 electroporation buffer solution, respectively, as per manufacturer's instructions in a 96-well round-bottom plate. TLN2 and CD2 RNP complexes were combined with cell suspensions in buffer solution and immediately transferred to a 16-well Nucleocuvette strip and the electroporation protocol CA137 (CD8$^+$ T cells) or FF104 (MitodsRed BMSCs) was performed on a Nucleofector Unit. After electroporation, warm media was added to the wells of the Nucleocuvette strip and cells were allowed to recover for 10 mins at RT, before being transferred back into tissue culture plates for expansion. Four days later, human co-cultures were set up with either Mito-dsRed hBMSC or CD8$^+$ T cells with *TLN2* KO or *CD2* KO (CRISPR control) and dsRed transfer rates to CD8$^+$ T cells were analyzed using flow cytometry. Knockout specificity and efficiency were determined by DISCOVER-seq and Amplicon NGS, respectively.

DISCOVER-seq

Preparation of the edited samples was carried out as previously described.[36] In brief, cells were fixed 12 hrs post editing in 1% formaldehyde (Pierce) for 15 min at RT, quenched with glycine (Merck, 125 mM final concentration) for 3 mins on ice, washed twice with ice cold PBS, pelleted, snap frozen in liquid nitrogen, and stored in -80°C till processing. A small sample from each condition was kept

in culture beyond DISCOVER-seq collection, for NGS analysis at 3 days post editing. After editing confirmation, processing was carried out as previously described[36] using the Mre11 antibody (Novus Biological). Sequencing libraries were prepared for each sample using the NEBNext Ultra II kit (New England Biolabs) according to manufacturer's instructions. NGS libraries were QCed, pooled, and sequenced on a NextSeq2000 (Illumina) using the P2 mid output kit (Illumina). After demultiplexing, reads were mapped against hg38 using Bowtie2 version 2.4.4 using very sensitive local alignment. Blender2 (https://github.com/cornlab/blender/blob/master/blender2.py) was run with default parameters, using the mock edited sample as control and filtering against the relevant blacklist sites in hg38 (https://github.com/staciawyman/blender/blob/master/hg38.blacklist.bed) to detect On- and Off-targets. Initially identified sites were further filtered for the presence of a valid PAM (by default NGG or NAG for SpCas9 based editing), and sites that met this criterion were allocated a DISCOVER score, which is calculated by summing up the read ends in a 10-bp window around the predicted cut site (-3 bp from the identified PAM). This initial target list was further filtered with default parameters from blender. In short, all sites with less than 8 mismatches towards the input guide and with a DISCOVER score >3 where kept. Additionally, sites with 4 or 5 mismatches were kept with a lower DISCOVER score threshold (>2) and the ones with less than 4 mismatches with a minimum DISCOVER score of 2. Results were visualized using the draw_blender_fig.py script provided with blender.

Amplicon sequencing and genome editing analysis

Primers including adaptors for subsequent NGS library preparation were designed to amplify a 100-250 bp region spanning the target site of interest. Sequences of oligos can be found in key resources table. Genomic DNA from edited or control cells was extracted using DNeasy kit (Qiagen) as per manufacturer's instructions. Approximately 100 ng of genomic DNA was used in PCR1 to amplify target alleles using the Q5 high fidelity polymerase (New England Biolabs), and after magnetic bead purification, barcoded with Illumina adaptors i5 and i7 in a short (8 cycles) PCR2. Individual NGS libraries were then bead purified, QCed on the Tapestation (D1000), Qubit quantified, and equimolarly pooled. NGS was performed on an NextSeq2000 (Illumina) using the P1 low output kit (Illumina). Demultiplexed NGS sequencing files (fastq) were analyzed for editing with CRISPResso2 (https://github.com/pinellolab/CRISPResso2) using default parameters and ignoring substitutions.[74]

Inhibitor treatment study

For pharmacological inhibition studies, both mouse and human Mito-dsRed BMSCs or $CD8^+$ T cells were treated with 1-10 μM of farnesyltransferase/geranylgeranyltransferase 1 inhibitor (L-778,123) (Biomol) incubated separately in their respective basal media for 7 hrs before or during co-culture. Cell viability of the different drug treatments was determined using the Trypan Blue exclusion test and quantified manually using a hemacytometer. All experiments were performed on at least 3-6 biological replicates/donors per condition.

Murine syngeneic melanoma model

C57BL/6 female mice ages 6–8 weeks were injected subcutaneously with 3×10^5 $B16_{KVP}$ cells in 100 μl of PBS. On day 10 after tumor inoculation, host mice received 6 Gy (C57BL/6 mice) or 2 Gy (NCG mice) sub-lethal irradiation prior to transfer of 1×10^5-1.25×10^5 $Mito^+$ and $Mito^-$ pmel-1 $CD8^+$ T cells. An untreated group that received no adoptively transferred cells was also included as a control. To support viability and expansion of transferred $CD8^+$ T cells, mice received recombinant IL-2 intraperitoneally (2.4×10^5 IU/day of rhIL-2 for 3 doses for 3 days). Mice were monitored thrice weekly for survival and tumor size using a caliper. The survival endpoint was reached when the mean diameter of the tumor size is 1.5 cm. For kinetic studies, SCENITH, and scRNA-seq analysis tumors and spleens were collected on day 7 post adoptive transfer. Tumors were cut into two equal portions using a scalpel; one half of the tumors was embedded in Tissue-Tek O.C.T. compound (Sakura Finetek) and immediately frozen for immunohistochemistry, and the other portion of tumors were weighed, digested, and tumor-infiltrating lymphocytes were analyzed by multidimensional flow cytometry analysis.

Frozen immunohistochemistry

Frozen tissues were sliced to 5 μm thick sections in a cryostat and fixed with acetone for 10 min at -20°C, left to dry for 20 minutes and then washed three times with PBS. Sections were blocked with 2% rat serum for 45 mins prior to overnight incubation with anti-mouse Ly5.1 antibody (1:100 dilution) in a humidified chamber at 4°C. Following PBS wash, tissue sections were counterstained with Hoechst 33342 (Invitrogen™, 2 μg/ml) for 10 min at room temperature, washed with PBS again, and mounted with ibidi mounting medium (Ibidi GmbH) and a glass coverslip. Images of the whole tissue sections were acquired using the LAS X Navigator tile scanning function on a Stellaris 8 confocal microscope (Leica Microsystems). ImageJ (version 1.54) was used to overlay a pseudocolor heatmap of Ly5.1 fluorescence intensity on confocal images of Hoechst 33342 to show the relative localization of adoptively transferred $CD8^+$ T cells in the tumor structure.

Quantification and phenotype of adoptively transferred $CD8^+$ T cells

Spleens were mechanically disrupted, passed through 40 μm strainers and treated for 2 min at room temperature with 1x ACK lysis buffer (Elabscience). Tumor tissue was mechanically disrupted in C-tubes using the m_tumor program on a GentleMACS (Miltenyi Biotec) followed by digestion for 30 mins with DNase and Collagenase at 37°C. Tumor-infiltrating lymphocytes were enriched using Ficoll® Paque Plus (Cytiva) at 400×g centrifugation for 30 mins at 18–20°C. Splenocytes and tumor-infiltrating lymphocytes were

stained separately with flow cytometry antibodies. CountBright™ Plus Absolute Counting Beads (Invitrogen™) were added to each sample for absolute quantification of tumor-infiltrating lymphocytes. For intracellular staining, cells were fixed and permeabilized using the FoxP3 staining kit (eBioscience) following surface marker staining. Quantification of adoptively transferred $CD8^+$ T cells was determined using Ly5.1 antibody and normalized based on counting beads, dilution factor, and tumor weights, where applicable.

Short and long-term *in vivo* functionality assays

Isolated $Mito^+$ and $Mito^-$ $CD8^+$ T cells were stained with a Cell Trace Violet Proliferation kit (Invitrogen) as per the manufacturer's instruction prior to adoptive transfer. For short-term *in vivo* functionality assays, 10^5 $Ly5.1^+$ pmel-1 T cells were transferred into the $B16_{KVP}$ tumor-bearing C57BL/6 mice. Tumors and spleens were harvested and processed 7 d later using the same isolation protocol described in the murine syngeneic melanoma model section. For long-term persistence *in vivo* studies, 10^5 $Ly5.1^+CD8^+$ T cells were adoptively transferred into sublethally irradiated (6 Gy) non-tumor-bearing C57BL/6 mice. Spleens were isolated and processed at day 28 post-transfer. Cells isolated from both spleens and tumor samples were stained with either MitoTracker green (Invitrogen) or Annexin V (Invitrogen) as per manufacturers protocols and followed by staining with LIVE/DEAD™ UV (Thermo Fisher Scientific), anti-mouse CD8-APC (Biolegend) and anti-mouse CD45.1 (Ly5.1)-APC/Cy7 (Biolegend).

Single-cell RNA-sequencing

$Mito^+$ and $Mito^-$ $CD8^+$ T cells were harvested directly prior to infusion (day 0) and harvested from tumor and spleens 7 d after adoptive transfer using murine syngeneic melanoma model set up and the isolation protocol described in the quantification and phenotype of adoptively transferred CD8+ T cells. Pre-infusion cells were washed and labeled with TotalSeq™-B anti-mouse Hashtag 1-6 (Biolegend) for 20 mins at 4°C as per manufacturer's instructions. For tumors and spleens, isolated cells were labeled with TotalSeq™-B anti-mouse Hashtag 1-4 (Biolegend) as per manufacturer's instructions followed by staining with LIVE/DEAD™ Fixable Far Red (Thermo Fisher Scientific), anti-mouse CD8-PacificBlue (BD Pharmingen) and anti-mouse CD45.1 (Ly5.1)-FITC (eBiosciences) for 20 mins each at 4°C. $CD8^+$ $CD45.1^+$ cells for each condition were sorted on FACS Aria Fusion II into DNA/RNA-low binding tubes containing 1 ml complete HBSS + 5% FCS. Each pool of sorted samples (pre-infusion, or tumors and spleens) was loaded onto a 10X Chromium Next GEM Chip G using the Chromium Next GEM Single Cell 3' Reagent Kits v3.1 and 3' Feature Barcode Kit (Dual Index) (10X Genomics) according to the manufacturer's protocol. Amplified cDNA was used for both, 3' RNA-seq library generation using the Chromium Single Cell 3′ Reagent Kit v3.1 and cell surface protein library preparation using the Chromium 3' Feature Barcode Kit (10X Genomics). 3' scRNA and scCSP libraries were quantified by QubitTM Fluorometer (ThermoFisher) and quality checked using Tapestation (Agilent Technologies). The libraries were pooled in a ratio 1 (scCSP) : 4 (scRNA) and sequenced on an Illumina Nextseq 2000 device. All sequencing runs were performed using the following parameters: PE-28-10-10-90.

Bioinformatic analysis of single-cell RNA-sequencing data

Base-calling and demultiplexing of sequencing reads were carried out using the bcl2convert provided by Illumina Dragon (v-3.8.4 NextSeq 2000, Illumina Inc., San Diego, California, USA). Sequencing reads were mapped to the mouse genome (https://cf.10xgenomics.com/supp/cell-exp/refdata-gex-mm10-2020-A.tar.gz, based on Mus_musculus.GRCm38.dna.primary_assembly.fa. modified and gencode.vM23.primary_assembly.annotation.gtf.filtered) using 10X Genomics Cell Ranger 7.0.0 with standard options and expected cells set to 12,000. Cell Ranger created count files for gene expression libraries and Cell-surface-marker (HTO) libraries.

Processing and analysis of single-cell RNA-seq and HTO count data were mainly performed in R (version 4.1.1) with the Seurat package (version 4.3.0). Since cell hashing was applied, it was possible to pool different groups in a single RNA-seq library. To assign groups to single cells based on HTO counts, the HTODemux() function from the Seurat package was employed with default settings (positive-quantile parameter of 0.99) after centralized log normalization. Cell calling via Cell Ranger yielded a total of 18,092 cells across the four libraries and all conditions. Cells that could not be assigned a treatment group due to insufficient HTO labeling (negative cells) were excluded from the analysis, resulting in 14,720 remaining cells. Doublets were identified based on ambiguous HTO labeling reported by HTODemux() and using the scDblFinder R-package[2] (version 1.8.0, used together with SingleCellExperiment, version 1.16.0) and also excluded from the analysis. scDblFinder was run in random approach. Known doublets from cell hashing were supplied, but only used for score thresholding and not for training. To obtain clusters, the FindNeighbours() and FindClusters() functions of Seurat were used with default parameters on each scRNA-seq library separately after excluding negative cells, using the top 20 principal components and 2,000 variable features as input. The clustering resolution was 0.4 for tumor samples, 0.2 for spleen samples, and 0.2 for *in vitro* samples.

For tumor and spleen samples, in order to obtain a valid set of cells for analysis, cells have additionally been filtered to have a minimum library count of 3,000, minimum number of features 1,000, maximum percentage of mitochondrial genes of 10% for spleen and tumor samples. In this step, filtering removed 9.5% of the tumor cells and 11.3% of the spleen cells. Further filtering was performed based on *singleR* (version 1.8.1)[75] annotation, filtering contaminating cells annotated as macrophages and CD4 T cells. Across all libraries, a total of 3,378 cells for spleen and 1,328 cells for tumor were then used for subsequent analyses.

For *in vitro* samples, cells have additionally been filtered to have a minimum ribosomal percentage of 15, minimum library counts of 1,000, minimum number of features 200, maximum percentage of mitochondrial genes of 10. Across all libraries, a total of 3,317 cells for *in vitro* samples were then used for subsequent analyses.

For dimensionality reduction and clustering counts were normalized for library size by dividing by the sum of total counts per cell and multiplying with a scale factor of 1 x 10^6. The 2,000 top variable features were identified by applying Seurat's FindVariableFeatures() function with default parameters (variance stabilizing transformation as selection method). Data was then mean-centered, scaled to unit variance, and subjected to principal component analysis (PCA). Afterwards, Seurat's FindNeighbours() function was used with the first 20 dimensions to construct a nearest-neighbor graph. The FindClusters() function was then run with default parameters (standard Louvain algorithm) to perform graph-based clustering on the cells. Clustering was run at different resolutions to find the optimal clustering setup. For visualization, a UMAP (Uniform Manifold Approximation and Projection3) dimensionality reduction was additionally applied to the data, using Seurat's RunUMAP() function on the first 20 dimensions of the data. A resolution of 0.2 was chosen for the final clustering setup in the case of spleen and in-vitro samples and a resolution of 0.4 for tumor samples, as they provided the best compromise between granularity and meaningfulness of clusters, as well as agreement with the localization of cells in UMAP space.

Differential gene expression was performed with FindAllMarkers() function from Seurat with logFC threshold 0.25, minimum fraction of 0.25 in either of the two populations, and Wilcoxon test. For spleen and tumor samples, differential expression for all pairwise comparisons between clusters was performed with FindMarkers() function from Seurat for logFC threshold 0 and default parameters. Results were plotted as violin plots for certain genes of interest, after Benjamini-Hochberg *p*-value correction between clusters.

To annotate the cell types of tumor and spleen samples, the scRNA-seq datasets were mapped on mouse TIL atlas, which consists of 16,803 single-cell transcriptomes (B16 melanoma and MC38 colon adenocarcinoma tumors). This projection was performed using ProjecTILs,[39] a computational method to project scRNA-seq data into reference single-cell atlases, enabling their direct comparison in a stable, annotated system of coordinates. As the mouse TIL atlas does not take into account proliferating cells, we integrated the analysis by adding the proliferation signatures from Pauken's dataset.[40]

The metabolic pathway score was calculated using the escape R package as described previously in Borcherding et al.[76] The Ucell method was used to calculate the enrichment score of metabolic signature genes and these scores were added to our single-cell object. The results were then visualized on UMAP and Violin plots using dittoSeq and Seurat packages, respectively.

Only for *in vitro* samples, differential expression was performed with FindMarkers() function from Seurat between ''spleen in vitro positive'' group and ''spleen in vitro negative group'', for a log fold change threshold of 0 and Wilcoxon test. The differential gene expression results for *in vitro* samples were then used as input to pathway/gene set analysis, using the GSEA (gene set enrichment analysis) approach as implemented in the clusterProfiler R-package (version 4.2.0) with the GSEA() function. As input for GSEA, the negative $\log_{10}$ p-values signed with the direction of the log FC were used with pvalueCutoff 1, maxGSSize 560 and minGSSize 1. Chosen gene set collection was Zhang et al.[25] Results were plotted with a modified gseaplot2() function allowing other colored bars from enrichplot (version 1.23.0.991).

Following GSEA analysis on a chosen gene set collection[25] of the human bulk and mouse scRNA *in vitro* data, core enriched genes were isolated from the results of the GSEA() function of clusterProfiler R-package (version 4.2.0). For conversion of human to mouse annotation gconvert() of gprofiler2 R-package (version 0.2.2) was used. Variance stabilized transformed expression values from human bulk were retrieved using the vst() function of DESeq2 (v 1.34.0) after removing the donor batch effect with the removeBatchEffect() function of limma(v3.50.0). Log-expression values from mouse scRNA *in vitro* samples were calculated using the AverageExpression() function of Seurat (v 4.0.5). The expression values were subset for the shared core enriched genes from both data sets. Subsequently, the expression values for each data set were scaled per gene using the scale() function. The scaled data sets were combined, the Euclidean distance of the genes was calculated with dist(method=''euclidean'') and hierarchical clustering was performed with hclust(method=''complete'') of the stats R-package. The heatmap was build with ggplot2 R-package (version 3.3.5), geom_tile() function, and the ggdendro R-package(0.1.23).

To visualize expression of Effector and Memory markers on a dimensional reduction plot (UMAP), FeaturePlot function was used from Seurat package which colors single cells on UMAP according to the gene expression.

SCENITH

SCENITH protocol was adapted from Argüello et al.[42] $Mito^+$ and $Mito^-$ $CD8^+$ T cells were harvested from $B16_{KVP}$ melanoma and spleen 7 d after adoptive transfer. Cells were plated at a density of 10^6 cells/ml antibiotic-free RPMI complete media in four separate wells (for three inhibitor treatments and untreated group) in either 48-well or 96-well flat bottom plates depending on cell numbers and allowed to rest for 1 hour at 37°C with 5% CO^2. The inhibitors [2-Deoxy-D-Glucose – abbreviated **2DG** (Sigma Aldrich; D6134), oligomycin – Abbreviated **Olig**, (Sigma Aldrich; 75351) and harringtonine – abbreviated **Har** (Santa Cruz Biotechnology; sc-204771)] were added to the separate wells for each sample at final concentrations of 100 mM (2DG), 1 μM (Olig), and 2 μg/ml (Har). For the untreated group, an equal volume of DMSO was added to each well as a control (**CO**). Cells were then incubated for 15 min at 37°C, 5% CO2. Following incubation, puromycin dihydrochloride (Sigma-Aldrich; P7255) was added to each well to reach a final concentration of 10 μg/ml. Cells were incubated for additional 25 min at 37°C, 5% CO2 to allow puromycin incorporation. Following the SCENITH treatment, the cells were transferred to a U-bottom 96-well plate on ice. Cells were centrifuged, washed in PBS, and then stained with LIVE/DEAD™ UV (Thermo Fisher Scientific) and surface markers anti-mouse CD8-Pacific Blue (BD Pharmigen), and anti-mouse CD45.1-FITC (ThermoFischer) for 20 mins on ice. After washing, the cells were fixed and permeabilized using the BD Cytofix/Cytoperm™ Fixation/Permeabilization Kit (BD Biosciences) according to the manufacturer's instructions. After washing the fixed cells twice with BD Perm/Wash™ Buffer solution, intracellular staining of puromycin (Anti-Puromycin antibody clone 12D10;

1:200, Sigma Aldrich; MABE-343-AF647) was performed for 1hr at 4°C in BD Perm/Wash™ Buffer. After incubation, cells were washed with BD Perm/Wash™ Buffer followed by FACS buffer and analyzed by flow cytometry. Based on the mean fluorescent intensity (MFI) of puromycin protein synthesis, metabolic capacities were calculated as follows: (i) Total metabolic capacity = CO-Har, (ii) FAAO capacity =100-100*(CO-2DG)/(CO-Har), and (iii) Glycolyitc capacity=100-100*(CO-Olig)/(CO-Har).

Quantification of *TLN2* expression

To determine *TLN2* expression over time, a human co-culture was set up using either activated or non-activated $CD8^+$ T cells with BMSCs. Following 24hrs of incubation, BMSC and $CD8^+$ T cells were collected, stained with anti-human CD8-BV510 (BD Biosciences) together with LIVE/DEAD™ Fixable Far Red Dead Cell Stain (Invitrogen™) and sorted based on cell type using BD FACS Aria Fusion II into collection with tubes with Buffer RLT (QIAGEN). RNA was extracted using RNeasy Plus Mini Kit (QIAGEN) and converted to cDNA using a High-Capacity cDNA Reverse Transcription Kit (Applied Biosystems) as per manufacturer instructions. Quantitative PCR was performed on sample cDNA using SYBR™ Green Master Mix with human primers for either *TLN2* or *ACTB* on a QuantStudio™ 3 Real-Time PCR system. See key resources table for oligonucleotide primer sequences.

Human *in vitro* cytotoxicity assay

For human *in vitro* cytotoxicity assays, $Mito^+$, $Mito^-$, $Mito^+$ EtBr or $Mito^-$ EtBr $CD19CAR^+$ $CD8^+$ T cells were co-incubated with target NALM6-GL leukemia cells at a 1:5 effector to target ratio (15,000:75,000) in 100 μl of AIM V or RPMI complete media in a 96 well round bottom plate (Corning). For tumor-infiltrating lymphocyte studies, MART-1 TILs were thawed and cultured in complete media supplemented with 3000 U/ml IL-2 for 2 days. One day prior to 36 hr co-culture with human primary cells or immortalized MitodsRed-BMSCs TILs were rested in complete media without IL-2. $Mito^+$ and $Mito^-$ MART-1-specific $CD8^+$ T cells were co-incubated with $MART\text{-}1^+$ SK23-GFP melanoma cells at a 1:5 effector to target ratio (4,000:20,000) in 200 μl of complete media in a 96-well flat bottom plate (Corning) for 48-72 hrs. GFP fluorescence intensity of the tumor cells was measured every 2 hrs using an Incucyte Live-Cell Analysis Instrument (Essen Bioscience). Green calibrated unit (GCU) per mm^2/image (NALM6-GL targets) or Target Green Object Area (TGOA) (SK23-GFP targets) were obtained using the Incucyte image software analyzer.

Repetitive *in vitro* cytotoxicity assay

$Mito^+$ and $Mito^-$ $CD19CAR^+$ $CD8^+$ T cells were co-incubated with NALM6-GL leukemia cells at a 1:1 effector to target ratio (20,000:20,000) in 200 μl of complete media in a 96 well plate (Corning) for 48-72 hrs. GFP fluorescence intensity of the tumor cells was measured every 2 hrs with an Incucyte Live-Cell Analysis Instrument (Essen Bioscience). After 48-72 hrs, cells were collected, washed and negatively enriched using a total $CD8^+$ T cells isolation kit (Stem Cell Technologies) and replated onto a new 96-well plate with 20,000 fresh NALM6-GL leukemia cells per well and measured on Incucyte for another 48-72 hrs. This process was repeated for a total of 6 rounds.

Humanized B-cell malignancy model

NALM6-GL (8×10^5) were injected intravenously into NXG host mice, followed 3 days later by the administration of 1.25×10^5 $CD19\text{-}CAR^+$ $CD8^+$ T cells that either acquired donor mitochondria ($Mito^+$), did not acquire donor mitochondria ($Mito^-$), or were cultured alone (CD8 mono). Recombinant human IL-15 (NCI) was injected intraperitoneally every other day (1 μg per mouse). Tumor burden was measured using the IVIS Lumina III in Vivo Imaging System (PerkinElmer). After 7 days, blood was collected from mice to confirm the adoptive transfer of $CD8^+$ T cells and to assess relative levels of circulating NALM6-GL cells in the blood.

QUANTIFICATION AND STATISTICAL ANALYSIS

Statistical analyses were conducted using Prism software v9.4 (GraphPad Software, La Jolla, California, USA). Spare respiratory capacity from Seahorse metabolic assay and inhibitor studies were analyzed using one-way ANOVA with Dunnett's multiple-comparison test. Transfer rates for *TLN2* KO CRISPR editing are shown as mean ± s.e.m. relative to *CD2* KO CRISPR control and analyzed using unpaired two-tailed Student's t-test. Flow cytometry data were analyzed using unpaired two-tailed Student's t-test. Tumor growth curves and Incucyte cytotoxicity assay were analyzed using Wilcoxon test on the curve slopes. A log-rank (MantelCox) test was used for comparison of survival curves for pmel-1 melanoma and NALM6 B-cell malignancy *in vivo* models. The p-value was denoted by * for $p < 0.05$, ** for $p < 0.01$, *** for $p < 0.001$, and **** for $p < 0.0001$.

CellPress
OPEN ACCESS

Supplemental figures

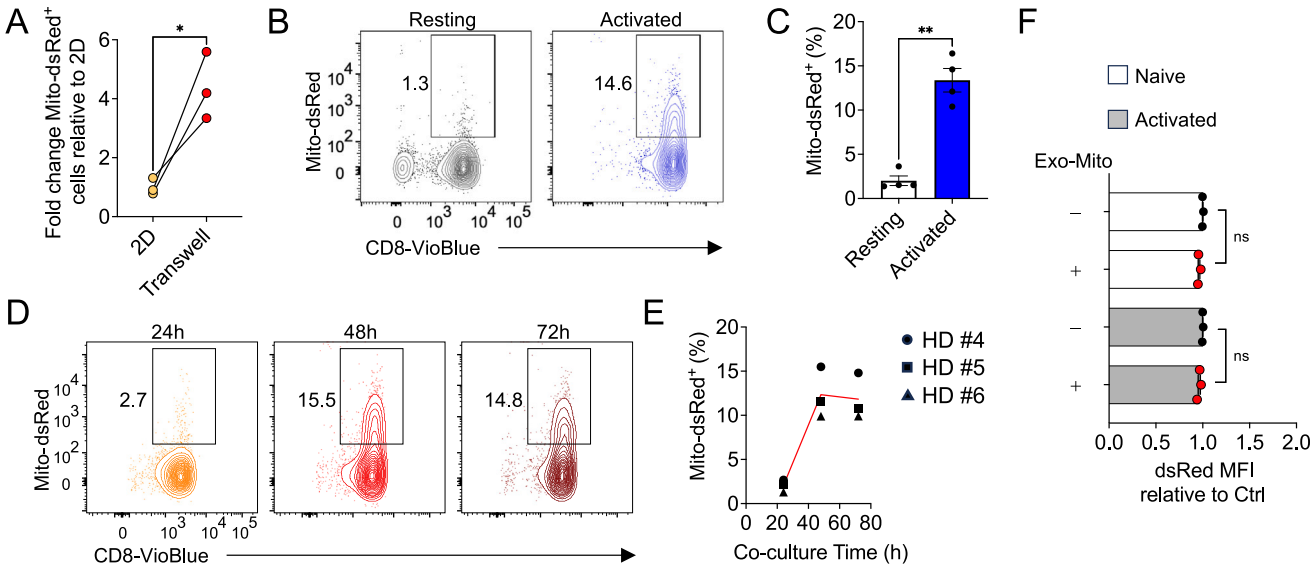

Figure S1. Parameters influencing mitochondrial transfer, related to Figure 2

(A) Fold-change difference in Mito-dsRed$^+$ mouse CD8$^+$ T cells after co-culture with BMSCs in transwell systems compared with 2D culture plates.

(B and C) Flow cytometry plot (B) and frequency (C) of Mito-dsRed$^+$ human CD8$^+$ T cells after BMSCs co-culture with CD8$^+$ T cells that were pre-activated with CD3/CD28 beads or in resting state (unstimulated). Data shown in (C) are mean ± SEM (n = 4 biological replicates).

(D and E) Flow cytometry plot (D) and frequency (E) of Mito-dsRed$^+$ human CD8$^+$ T cells at the indicated time points after BMSCs co-culture.

(F) Bar graph showing dsRed levels (mean fluorescent intensity [MFI]) relative to control T cells. Naive and activated T cells were cultured in the presence and absence of dsRed$^+$ mitochondria, isolated from Mito-dsRed BMSCs (referred to as Exo-Mito). T cells were analyzed by flow cytometer and data normalized with the MFI of T cells that were not incubated with BMSC mitochondria. Data shown are mean ± SEM (n = 3 biological replicates). *p < 0.05, **p < 0.01 (paired two-tailed Student's t test). ns, not significant.

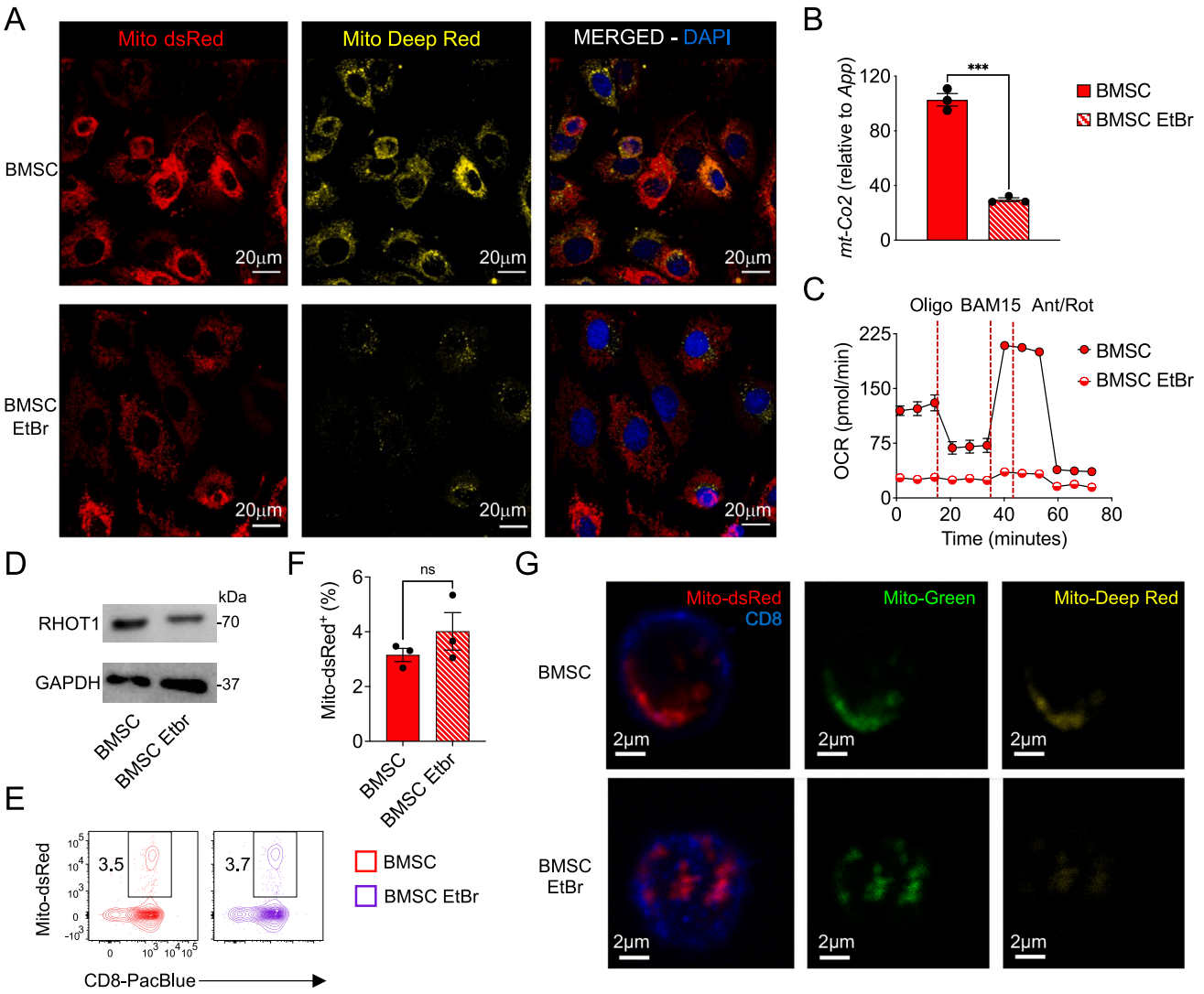

Figure S2. EtBr-treated BMSCs have dysfunctional mitochondria, related to Figure 2

(A) Confocal microscopy images of mouse Mito-dsRed BMSCs that were left untreated or pre-treated with 200 ng/mL ethidium bromide (EtBr). MitoTracker Deep Red, a mitochondrial potential-dependent dye, was used to stain functional mitochondria. Scale bar is 20 μm.

(B) Quantitative real-time PCR of mt-CO2 mRNA in EtBr-treated or untreated Mito-dsRed BMSCs. Bars (mean ± SEM of technical triplicates) are relative to *App*.

(C) Oxygen consumption rates (OCRs) of EtBr-treated or untreated Mito-dsRed BMSCs. Data were obtained under basal culture conditions and in response to the indicated molecules. Data shown are mean ± SEM (n = 4 technical replicates).

(D) RHOT1 in EtBr-treated or untreated Mito-dsRed BMSCs assessed by immunoblot. GAPDH was used as loading control.

(E and F) Flow cytometry plot (E) and frequency (F) of Mito-dsRed$^+$ CD8$^+$ T cells after co-culture with EtBr-treated or untreated Mito-dsRed BMSCs. Data shown in (F) are mean ± SEM (n = 3 biological replicates).

(G) Confocal microscopy images of sorted Mito-dsRed$^+$ CD8$^+$ T cells after co-culture with EtBr-treated or untreated Mito-dsRed BMSCs. ns, not significant; ***$p < 0.001$ (unpaired two-tailed Student's t test). Scale bar is 2 μm.

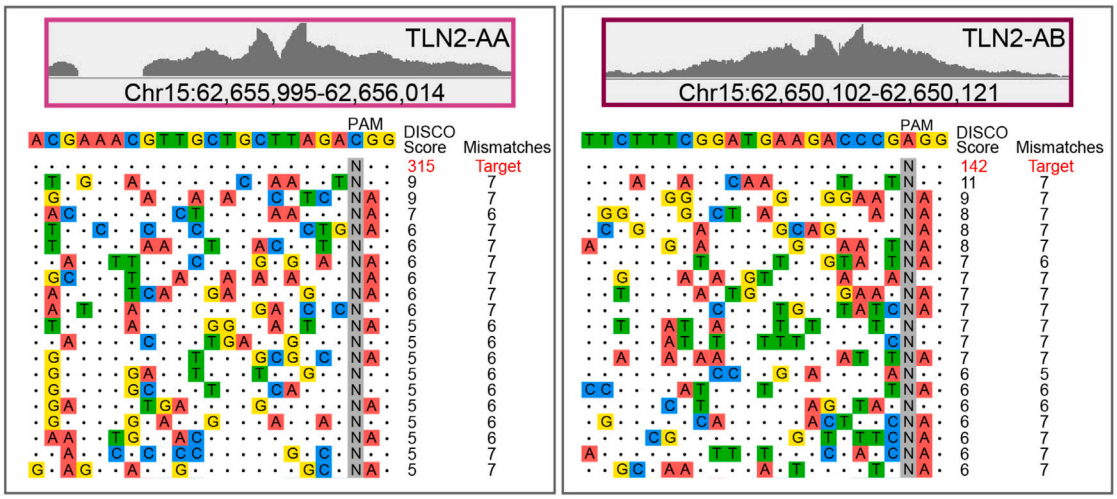

Figure S3. Specific Talin-2 (*TLN2*) targeting by TLN2 CRISPR-RNAs (crRNAs), related to Figure 3

DISCOVER-seq (discovery of *in situ* Cas off-targets and verification by sequencing) output for the TLN2-AA and TLN2-AB crRNAs in T cells. The top 20 sites sorted for DISCO score. Besides the on-target site, all other sites exhibit a high number of mismatches, with the majority also harboring the non-canonical protospacer adjacent motif (PAM) NAG.

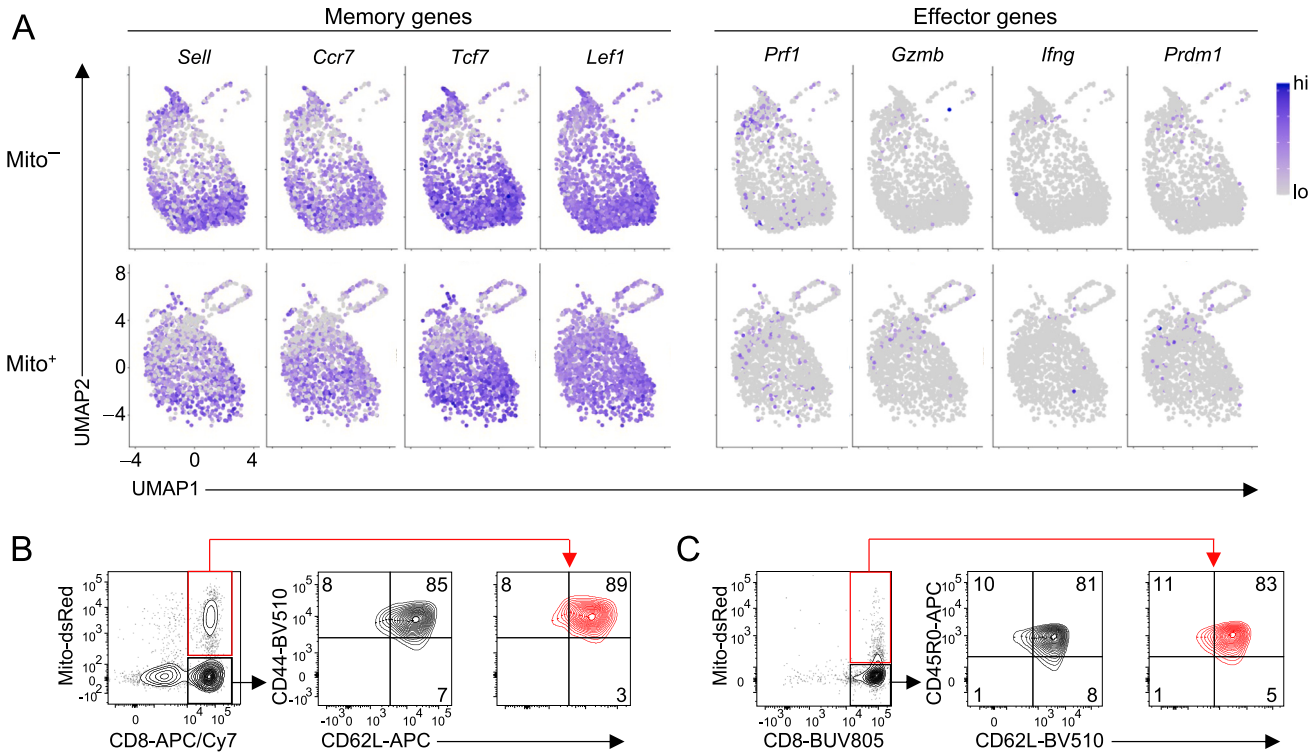

Figure S4. Mito$^+$ and Mito$^-$ T cells exhibit a similar differentiation state in pre-infusion products, related to Figures 4 and 7

(A) Feature plots showing mRNA expression of the indicated memory and effector genes in Mito$^+$ and Mito$^-$ cells assessed by scRNA-seq. Data are pooled from 3 independent donors.

(B) Representative flow cytometry analysis of mouse CD8$^+$ T cells after a 48 h co-culture with mouse Mito-dsRed BMSCs. Right panels show the expression of CD44 and CD62L on Mito$^+$ (red) and Mito$^-$ (black).

(C) Representative flow cytometry analysis of human CD8$^+$ T cells after a 48 h co-culture with human Mito-dsRed BMSCs. Right panels show the expression of CD45R0 and CD62L on Mito$^+$ (red) and Mito$^-$ (black). Numbers indicate the frequency of cells in the quadrant.

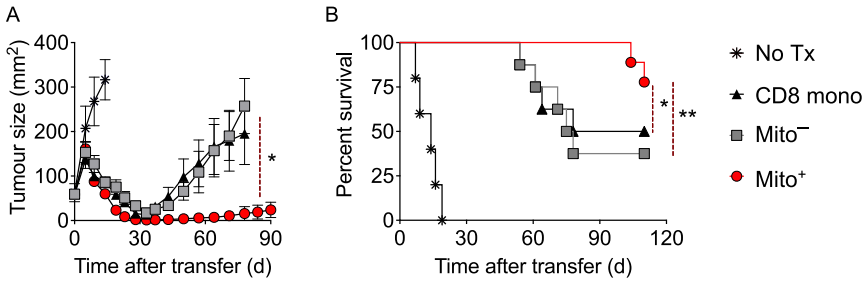

Figure S5. BMSC mitochondrial transfer enhances CD8$^+$ T cell antitumor immunity in immunodeficient mice, related to Figure 4

Tumor size (A, mean ± SEM) and survival curve (B) of sublethally irradiated NCG mice bearing $B16_{KVP}$ tumors after treatment with 2.5 × 10^5 Mito$^+$ and Mito$^-$ pmel-1 Ly5.1$^+$CD8$^+$ T cells with recombinant human IL-2 (n = 8 or 9 mice/group). No Tx, no treatment (n = 5 mice). *p < 0.05 (Wilcoxon test, A; log-rank [Mantel-Cox] test, B) and **p < 0.01 (log-rank [Mantel-Cox] test).

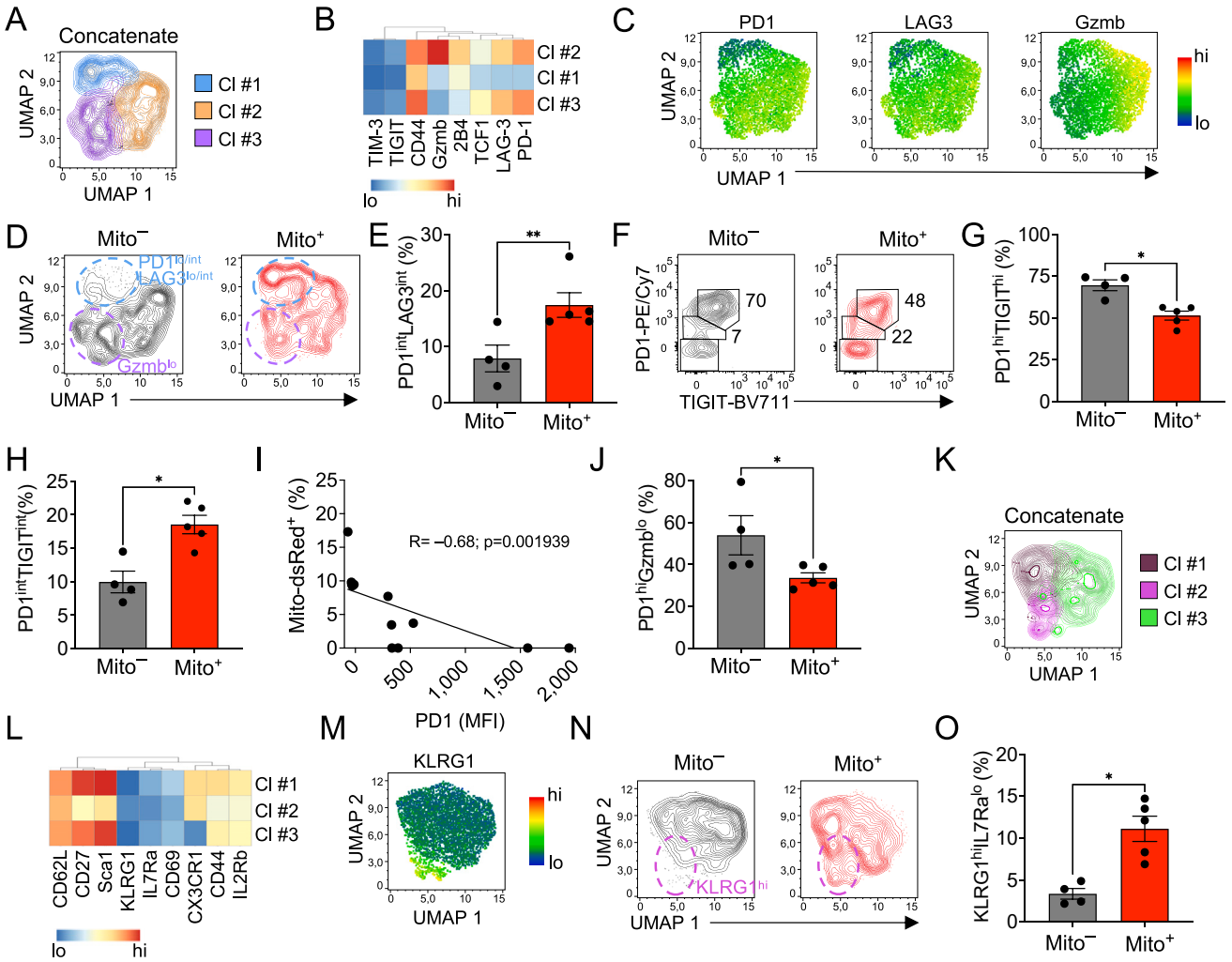

Figure S6. BMSC mitochondrial transfer enhances CD8⁺ T cell effector differentiation within tumors while preventing T cell exhaustion, related to Figure 5

1.25 × 10^5 Mito⁺ and Mito⁻ pmel-1 Ly5.1⁺CD8⁺ T cells were adoptively transferred into sublethally irradiated Ly5.2⁺ mice bearing B16 tumors in conjunction with recombinant human IL-2.

(A) UMAP plots of concatenated Mito⁺ and Mito⁻ pmel-1 Ly5.1⁺CD8⁺ T cells isolated from tumors 7 days after treatment showing the distribution of 3 clusters (Cl) identified by FlowSOM.

(B) Heatmap showing the relative expression levels of the indicated molecules in the 3 FlowSOM clusters.

(C) UMAP plots of concatenated Mito⁺ and Mito⁻ pmel-1 Ly5.1⁺CD8⁺ T cells showing the expression levels of PD-1 (left), LAG3 (center), and Gzmb (right).

(D) UMAP plots of Mito⁺ and Mito⁻ pmel-1 Ly5.1⁺CD8⁺ T cells showing differences in cluster distributions.

(E) Frequencies of Mito⁺ and Mito⁻ pmel-1 Ly5.1⁺CD8⁺ T cells expressing intermediate levels of PD-1 and LAG3 7 days after treatment. Data shown are mean ± SEM (n = 4–5 biological replicates).

(F–H) Flow cytometry plot (F) and frequency (G and H) of intratumoral Mito⁺ and Mito⁻ pmel-1 Ly5.1⁺CD8⁺ T cells expressing high (G) and intermediate (H) levels of PD-1 and TIGIT 7 days after tumor treatment. Data shown in (G) and (H) are mean ± SEM (n = 4–5 biological replicates).

(I) Correlation between the percentage of Mito-dsRed⁺ cells and the levels of PD-1 in intratumoral Mito⁺ pmel-1 Ly5.1⁺CD8⁺ T cells. *$p < 0.05$ (unpaired two-tailed Student's t test).

(J) Frequencies of Mito⁺ and Mito⁻ pmel-1 Ly5.1⁺CD8⁺ T cells expressing the indicated combinations of PD-1 and Gzmb 7 days after treatment. Data shown are mean ± SEM (n = 4–5 biological replicates).

(K) UMAP plots of concatenated Mito⁺ and Mito⁻ pmel-1 Ly5.1⁺CD8⁺ T cells isolated from B16 tumors 7 days after treatment showing the distribution of 3 clusters (Cl) identified by FlowSOM.

(L) Heatmap showing the relative expression levels of the indicated molecules in the 3 FlowSOM clusters.

(M) UMAP plots of concatenated Mito⁺ and Mito⁻ pmel-1 Ly5.1⁺CD8⁺ T cells showing the expression levels of KLRG1.

(N) UMAP plots of Mito⁺ and Mito⁻ pmel-1 Ly5.1⁺CD8⁺ T cells showing differences in cluster distributions.

(O) Frequency of Mito⁺ and Mito⁻ pmel-1 Ly5.1⁺CD8⁺ T cells expressing the indicated combinations of KLRG1 and IL-7Ra 7 days after treatment. Data shown are mean ± SEM (n = 4–5 biological replicates). *$p < 0.05$; **$p < 0.01$ (unpaired two-tailed Student's t test).

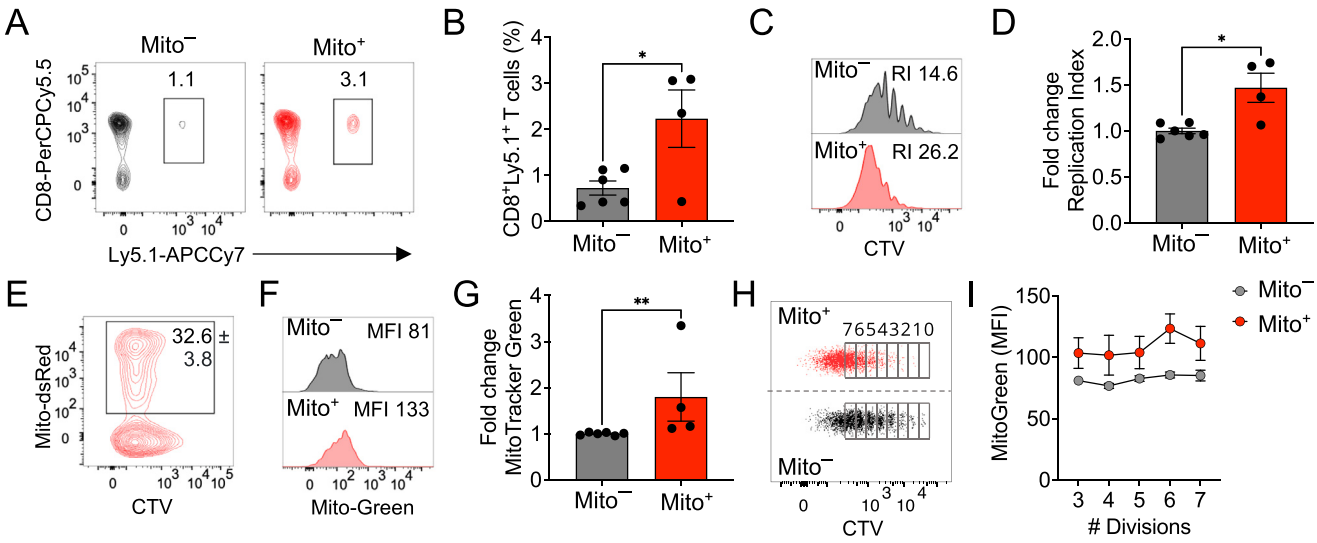

Figure S7. Mitochondrial transfer augments CD8⁺ T cell mitochondrial mass long-term boosting cell persistence, related to Figure 6

(A and B) Flow cytometry plot (A) and frequency (B) of pmel-1 Mito$^+$ and Mito$^-$ Ly5.1$^+$CD8$^+$ T cells in the spleen 28 days after transfer into sublethally irradiated Ly5.2$^+$ mice in conjunction with recombinant human IL-2. Data shown in (B) are mean ± SEM (n = 4–6 biological replicates).

(C and D) Flow cytometry plot (C) and bar graph (D) showing proliferation differences between pmel-1 Mito$^+$ and Mito$^-$ T cells 28 days after transfer as in (A) and (B). RI, replication index. Data shown in (D) are mean ± SEM (n = 4–6 biological replicates).

(E) Flow cytometry plot of Mito$^+$ pmel-1 Ly5.1$^+$CD8$^+$ T cells in the spleen 28 days after transfer showing CTV signals versus Mito-dsRed.

(F and G) Flow cytometry plot (F) and fold change differences (G) of MitoTracker Green levels in pmel-1 Mito$^+$ and Mito$^-$ Ly5.1$^+$CD8$^+$ T cells in the spleen 28 days after transfer as in (A) and (B). Data shown in (G) are mean ± SEM (n = 4–6 biological replicates).

(H and I) MitoTracker Green MFI (I) in pmel-1 Mito$^+$ and Mito$^-$ cells for each of the indicated divisions as per the gating strategy shown in (H). Data shown in (I) are mean ± SEM (n = 3 biological replicates).